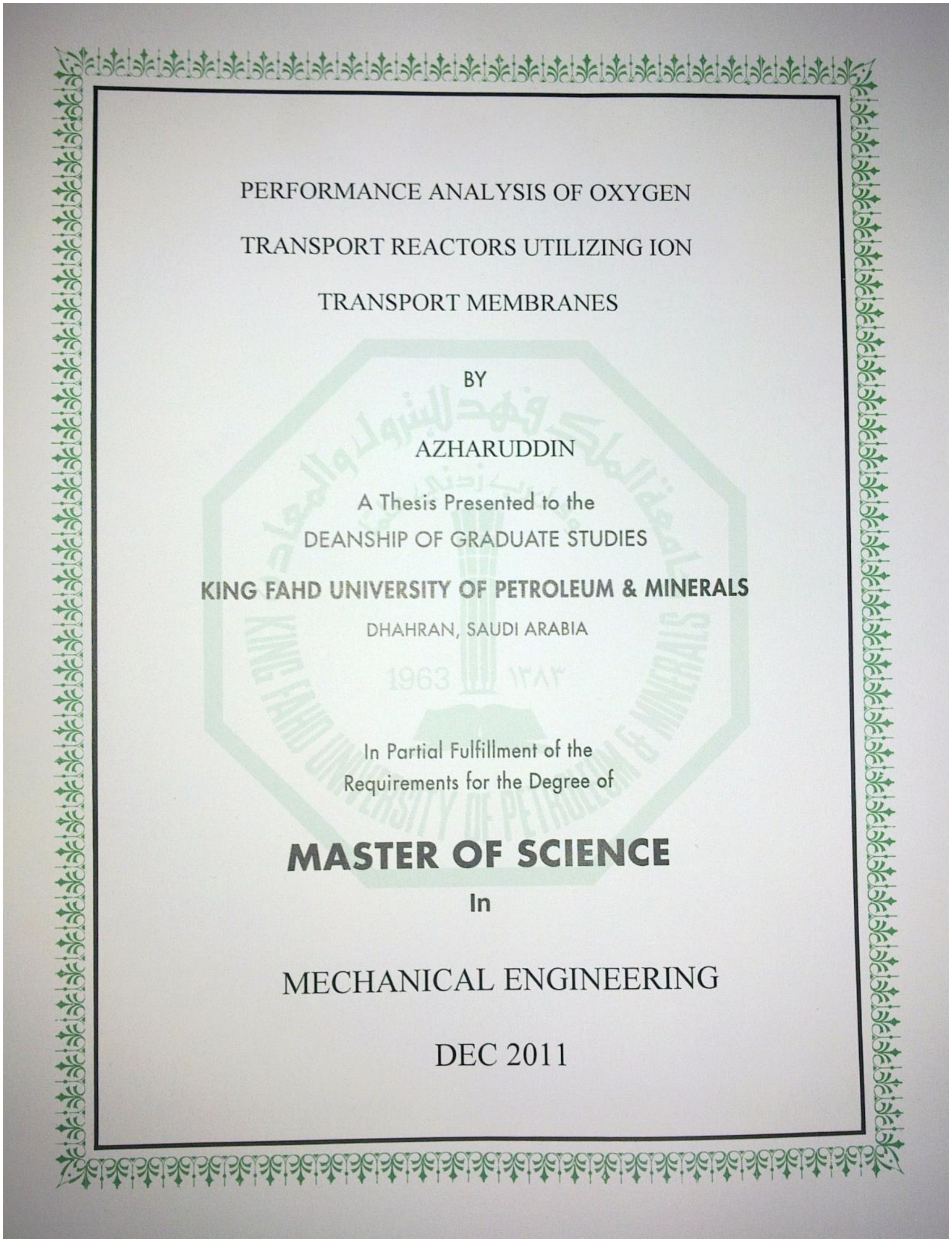

PERFORMANCE ANALYSIS OF OXYGEN TRANSPORT REACTORS UTILIZING ION TRANSPORT MEMBRANES

BY

AZHARUDDIN

A Thesis Presented to the
DEANSHIP OF GRADUATE STUDIES

KING FAHD UNIVERSITY OF PETROLEUM & MINERALS
DHAHRAN, SAUDI ARABIA

In Partial Fulfillment of the
Requirements for the Degree of

MASTER OF SCIENCE

In

MECHANICAL ENGINEERING

DEC 2011

KING FAHD UNIVERSITY OF PETROLEUM & MINERALS

DHAHRAN 31261, SAUDI ARABIA

DEANSHIP OF GRADUATE STUDIES

This thesis, written by Azharuddin under the direction of his thesis advisor and approved by his thesis committee, has been presented to and accepted by the Dean of Graduate Studies, in partial fulfillment of the requirements for the degree of **MASTER OF SCIENCE in MECHANICAL ENGINEERING**.

Thesis Committee

Hassan Badr

Dr. Hassan M. Badr (Advisor)

Med Habib

Dr. M A Habib (Member)

R.B. Mansour

Dr. Rached Ben Mansour (Member)

Dr. Amro M. Al- Qutub
Department Chairman

Dr. Salam A. Zummo
Dean of Graduate Studies

29/2/12

Date

بسم الله الرحمن الرحيم

ACKNOWLEDGEMENT

"In the name of Allah, The Most Gracious and The Most Merciful"

All praise belongs to Almighty Allah (s.w.t.) for bestowing me with courage and perseverance to carry out this work sincerely. I thank Almighty Allah for giving me chance to do my M.S. successfully at King Fahd University of Petroleum and Minerals, Dhahran. I am happy to have had a chance to glorify His name in the sincerest way through this small accomplishment and ask Him to accept my efforts.

Acknowledgement is due to King Fahd University of Petroleum and Minerals for providing me financial support and good academic environment during the course of my M.S. Special thanks is also due to the Center of Clean Water and Clean Energy at M.I.T and KFUPM.

My deep gratitude and appreciation goes to my thesis advisor, my mentor Dr. Hassan M Badr for his constant endeavor, guidance and motivation during the course of my study. His valuable and priceless suggestions made this work interesting and challenging for me. I also wish to express my deep appreciation to Dr. M A Habib for his help, guidance, and constant encouragement during my M.S. I am greatly indebted to Dr. Rached Ben Mansour for the valuable time he spent throughout my thesis work and also for always being supportive and helping me during difficult times.

I would also like to acknowledge all the Mechanical Engineering faculty members with whom I took courses during my M.S. especially Dr. Shuja and Dr. Yilbas who helped me a lot, guided me and encouraged me during my coursework and related research.

TABLE OF CONTENTS

ACKNOWLEDGEMENT iv

LIST OF TABLES ix

LIST OF FIGURES x

THESIS ABSTRACT (ENGLISH) xviii

THESIS ABSTRACT (ARABIC) xx

CHAPTER 1 1

INTRODUCTION 1

- 1.1 Research Background 1
- 1.2 Problem Statement 5
- 1.3 Objectives 5
- 1.4 Thesis Outline 6

CHAPTER 2 8

LITERATURE REVIEW 8

- 2.1 Carbon Capture and Sequestration technologies 8
  - 2.1.1 Pre-combustion capture: 11
  - 2.1.2 Post combustion capture: 12

2.1.3 Oxyfuel Combustion: 13

2.1.4 Economic viability: 15

2.2 Oxyfuel combustion in power cycles 16

2.2.1 Combustion in power cycle 18

2.2.2 Flue Gas Composition: 19

2.2.3 Oxyfired power plants incorporating oxygen transport membranes 20

2.3 Membranes for gas separation in Carbon capture and sequestration 30

2.3.1 Mixed Ionic and Electronic Conducting (MIEC) Membranes for O_2/N_2 separation: 31

2.3.2 Oxygen Transport Theory: 31

2.3.3 Bulk transport theory: 34

2.3.4 Surface exchange- limited reaction: 38

2.3.5 Generalized transport equation: 40

2.4 Numerical work in the area of membranes 50

CHAPTER 3 55

MODEL DEVELOPMENT 55

3.1 Membrane Permeation model 55

3.1.1 Methodology: 57

3.1.2 Governing Equations: 58

3.1.3 User Defined Function (UDF): 60

3.2 Combustion Mechanism 64

3.2.1 Reaction Mechanism for methane combustion: 65

3.3 Numerical Scheme and Boundary conditions 68

CHAPTER 4 71

NUMERICAL STUDY 71

4.1 Grid Independence 71

4.2 Validation 74

CHAPTER 5 83

RESULTS AND DISCUSSION 83

5.1 Cold Combustion (Mixing) 83

5.2 Combustion in ITM Reactor 96

5.2.1 Temperature characteristics: 102

5.2.2 Combustion characteristics: 106

5.2.3 Effect of fuel mass flow rate on O_2 permeation flux (J_{O2}): 121

5.2.4 Effect of fuel mass flow rate on combustion temperature: 122

5.2.5 Effects of fuel mass flow rate on permeate O_2 partial pressure:................ 123

5.2.6 Effect of mass flow rate on O_2/CH_4 ratio: 124

5.2.7 Temperature contours for different compositions: 126

5.3 Energy Balance verification 132

5.4 Effect of local temperature variation along the membrane surface and radiation heat transfer on the combustion process... 135

CHAPTER 6 141

CONCLUSION AND RECOMMENDATIONS FOR FUTURE WORK..................... 141

6.1 Cold Combustion (O_2 separation-only) 141

6.2 Combustion in Oxygen Transport Reactor (OTR) 142

6.3 Future work:.. 143

Nomenclature.. 144

References... 149

Vita.. 162

LIST OF TABLES

Table 1 Materials and operating conditions of previous experimental work done on tubular membrane for oxygen permeation……………………………………………….50

Table 2 Coefficients of polynomial functions belonging to temperature-dependent thermal properties of species, taken from the material property database given by Fluent Inc.…………………………………………………………………………….. 69

Table 3 Properties of reactant and product species…………………………………....70

Table 4 List of model parameter values……………………………………………... 97

Table 5 List of operating conditions for the reactive mode. Feed gas is air and sweep gas is CH_4/CO_2 mixture………………………………………………………………. 100

LIST OF FIGURES

Figure 1 World Energy consumption based on usage based on the types of fuel (Mtoe) [8] 9

Figure 2 World CO_2 emissions from different types of fuels (Mt of CO_2) [8].................. 9

Figure 3 CO_2 capture system [9].. 11

Figure 4 Pre-combustion process [9] 12

Figure 5 Oxyfuel Process [9] 14

Figure 6 various technology showing efficiencies [16]. 17

Figure 7 Oxyfuel process with water condensation [25] 20

Figure 8 Oxyfuel process without water condensation [28] 20

Figure 9 AZEP Oxyfired cycle incorporating OTM [30] 23

Figure 10 4-end integration system [32].. 24

Figure 11 3-end system integration [32]... 25

Figure 12 Oxygen Conduction in OTM in four-end design (left) and three-end design (right) 26

Figure 13 The ZEITMOP cycle in which OTR is remote from Combustion chamber [33] 27

Figure 14 The ZEITMOP cycle with OTR and combustion chamber combined [35] 30

Figure 15 Different sections of ITM involved in oxygen transport during oxygen permeation 32

Figure 16 Variation of regime from bulk-diffusion to surface-exchange reaction limited with decreasing membrane thickness [38] 33

Figure 17 Surface exchange and bulk diffusion mechanism 40

Figure 18 Mechanism of Oxygen transport through dense Ion transport membrane by considering Surface exchange mechanism 56

Figure 19 Solution strategy for oxygen transport though the membrane. 63

Figure 20 Axi-symmetric geometrical view for Wang et al [58] 67

Figure 21 Domain for oxyfuel Ion transport membrane reactor 67

Figure 22 Mass Fraction of O_2 with three different grids without combustion 72

Figure 23 Mass Fraction of O_2 for three different grids with combustion 73

Figure 24 Temperature variation along the axis for three different grids 73

Figure 25 Variation of O_2 permeation flux with oxygen partial pressure at inlet of shell side 75

Figure 26 Variation of O_2 permeation flux and O_2 outlet partial pressure with O_2 partial pressure in the outer region 76

Figure 27 Variation of the O_2 permeation flux over the reactor length for a) different operating temperatures, and b) different inlet partial pressures (P_1) 78

Figure 28 Variation of O_2 mass fraction within the reactor for different values of P_1 at the operating temperature of 800^0C 79

Figure 29 Oxygen permeation flux against $(P_1/P_0)^{0.5}-(P_2/P_0)^{0.5}$ at different temperatures 80

Figure 30 Schematic of computational domain along with a description of some of the boundary conditions used in the model by Norton and Vlachos [89] 81

Figure 31 Centre line temperature profile for premixed combustion of air/methane mixture 82

Figure 32 Oxygen to methane mass fraction ratio for different inlet conditions of sweep ratio (CO_2/ CH_4) for co-current configuration 87

Figure 33 Oxygen to methane mass fraction ratio for different inlet conditions of sweep ratio (CO_2/ CH_4) for counter-current regime 88

Figure 34 Mass fraction of species for different sweep ratios (CO_2/ CH_4) at inlet for co-current regime 89

Figure 35 Mass fraction of species for different sweep ratios (CO_2/ CH_4) at inlet for counter-current regime 90

Figure 36 Ratio of O_2/CH_4 for different sweep ratios (CO_2/CH_4) 91

Figure 37 Variation of O_2/CH_4 along the reactor axis for different sweep ratios (CO_2/CH_4); 92

Figure 38 Variation of the oxygen permeation flux along the membrane surface for different sweep ratios (CO_2/CH_4) 93

Figure 39 Variation of total oxygen permeation rate with percentage of CH4 in the sweep mixture 95

Figure 40. The cross section of the monolith reactor [92].. 97

Figure 41 Temperature, reaction rate and composition profiles 98

Figure 42 Oxygen permeation Flux for the reactive and separation only case................. 99

Figure 43 Temperature profiles for the different sweep gas mixture for three different mass flow rates. 101

Figure 44 Kinetic rate of reaction profiles for different sweep gas mixture for three different mass flow rates. 104

Figure 45 O_2/CH_4 profiles for the different sweep gas composition 105

Figure 46 CH_4 Mass fraction profiles for different sweep gas composition.................. 108

Figure 47 Percentage CH_4 conversion for different mass flow rates.............................. 109

Figure 48 Percentage of O_2 & CH_4 conversion and O_2 permeation rate for mass flow rate of 1.625×10^{-07} Kg/s 109

Figure 49 O_2/CH_4 vs Percentage of CH_4 at inlet for different mass flow rates 110

Figure 50 O_2 Mass Fraction Profiles for different sweep gas composition 113

Figure 51 O_2 Permeation flux for different sweep gas composition 114

Figure 52 Radial temperature profiles at different sections for mass low rate of........... 115

Figure 53 O_2 mass fraction radial profiles for mass flow rate of 1.625×10^{-7} Kg/s......... 117

Figure 54 Radial temperature and composition profiles for mass flow rate of 1.625×10^{-7} Kg/s for m_R of 0.5/0.5 118

Figure 55 Temperature and composition profiles for three different mass flow rates at m_R =0.5/0.5 120

Figure 56 Effect of mass flow rate of fuel on the oxygen permeation flux 121

Figure 57 Temperature profiles for different fuel mass flow rates 122

Figure 58 O_2 partial pressure profiles for different fuel mass flow rates 123

Figure 59 O_2/CH_4 for different mass flow rates 124

Figure 60 Comparison between oxygen permeation rate from the ITM with and without combustion for mass flow rate of 1.625×10^{-07} Kg/s 125

Figure 61 Temperature contour for mass flow rate of 1.625×10^{-07} Kg/s and different CH_4/CO_2 mixtures mass ratio m_R 128

Figure 62 Temperature contour for mass flow rate of 4.625×10^{-07} Kg/s and different CH_4/CO_2 mixtures mass ratio m_R 129

Figure 63 Temperature contour for mass flow rate of 8.625×10^{-07} Kg/s and different CH_4/CO_2 mixtures mass ratio m_R 130

Figure 64 Temperature contour for three different mass flow rate of 8.625×10^{-07} Kg/s for CH4/CO2 of 1.0/0. 131

Figure 65 Block Diagram of ITM reactor 132

Figure 66 Oxygen Permeation flux through the BSCF membrane tube as a function of temperature [58]. 136

Figure 67 O_2 permeation flux for different temperature for increasing partial pressure at shell side... 137

Figure 68 Temperature along the axis of the reactor for mass flow rate of 1.625×10^{-7} Kg/s for a) m_R=0.1/0.9 b) m_R=0.5/0.5 c) m_R=1.0/0.. 138

Figure 69 Temperature contours for mass flow rate of 1.625×10^{-7} Kg/s and m_R = 1.0/0 with equation 36 and equation 37 139

LIST OF ABBREVIATIONS

CCS	Carbon Capture and Sequestration
CFD	Computational Fluid Dynamic
EOR	Enhanced Oil Recovery
ECBM	Enhanced Coal Bed Methane Recovery
ITM	Ion Transport Membrane
OTR	Oxygen Transport Reactor
OTM	Oxygen Transport Membrane
MCM	Mixed Conducting Membrane
IPCC	Intergovernmental Panel on Climate Change
IGCC	Integrated Gasification Combined Cycle
NGCC	Natural Gas Combined Cycle
FGD	Flue Gas Desulphurization
MEA	Mono-Ethanol Amine
PC	Pulverized Coal

ASU	Air Separation Unit
ATR	Auto-Thermal Reforming
HFMR	Hollow Fiber Membrane Reactor
CES	Clean Energy Systems
BSCF	$Ba_{0.5}Sr_{0.5}Co_{0.8}Fe_{0.2}O_{3-\delta}$
ZEITMOP	Zero Emission Ion Transport Membrane Oxygen Power
UDF	User-Defined Function
SIMPLE	Semi-Implicit Method for Pressure-Linked Equations
AMG	Aggressive Advanced Multigrid
BCGSTAB	Bi-Conjugate Gradient Stabilized Method

THESIS ABSTRACT (ENGLISH)

NAME: AHARUDDIN

TITLE: PERFOMANCE ANALYSIS OF OXYGEN TRANPORT REACTOR UTILIZING ION TRANSORT MEMBRANES

MAJOR: MECHANICAL ENGINEERING

DATE: DEC 2011

This study aims at investigating the performance of a cylindrical ion transport reactor designed for oxy-fuel combustion. The cylindrical reactor walls are made of dense, nonporous, mixed-conducting ceramic membranes that only allow oxygen permeation from the outside air into the combustion chamber. The sweep gas (CO_2 and CH_4) enters the reactor from one side, mixes with the oxygen permeate and the combustion products are discharged from the other side. The process of oxygen permeation through the reactor walls is influenced by the flow condition and composition of air at the feed side (inlet air side) and the gas mixture at the permeate side (sweep gas side). The modeling of the flow process is based on the numerical solution of the conservation equations of mass, momentum, energy and species in the axi-symmetric flow domain. The membrane is modeled as a selective layer in which the oxygen permeation depends on the prevailing temperatures as well as the oxygen partial pressure at both sides of the membrane. The CFD calculations were carried out using FLUENT 12.1 while the mass transfer of oxygen through the membrane is modeled by a set of user defined functions. The model *results were validated against previous experimental data and the comparison showed a good agreement. Further, the study is carried out for the optimal composition mixture of sweep gas for cold-combustion (mixing) within the reactor. Lastly the integration of membrane model with ITM reactor as combustion chamber is done by using single step methane combustion chemistry. The results showed the significant increase of* O_2 *permeation in case of combustion in comparison with cold combustion.*

MASTER OF SCIENCE DEGREE

KING FAHD UNIVERSITY OF PETROLEUM & MINERALS

Dhahran, Saudi Arabia

THESIS ABSTRACT (ARABIC)

الاسم: اظهرالدين

العنوان: تحليل اداء مفاعلات نقل الأكسجين باستخدام الاغشيه الناقله الايونيه
التخصص: الهندسة الميكانيكية .

التاريخ: ديسمبر 2011 .

تهدف هذه الدراسة إلى التحقيق في أداء مفاعل نقل ايوني أسطواني مصمم لاحتراق الوقود مع الأكسجين .تم اعتبار جدران المفاعل الاسطواني المصنوع من ماده غير مسامية من السيراميك ناقلة للأيونات والإلكترونات وتسمح فقط للأكسجين للتغلغل من الهواء الخارجي لغرفة الاحتراق . يدخل غاز الاكتساح (خليط من ثاني أكسيد الكربون وغاز الميثان) إلى المفاعل من جانب واحد، يختلط مع الأوكسجين ويتم تفريغه من نواتج الاحتراق من الجانب الآخر. تتأثر عملية تغلغل الأكسجين من خلال جدران المفاعل بحالة تدفق وتكوين الهواء في جانب التغذية. (مدخل الهواء الجانبي)، وخليط الغاز في الجانب الآخر من الغشاء (جانب غاز الاكتساح) .ويستند وضع نماذج عملية التدفق على الحل العددي لمعادلات حفظ الكتلة والطاقة والحركة ومكونات الغاز . وتم تصميم ونمذجة الغشاء كطبقة انتقائية يعتمد فيها تغلغل الأكسجين على درجات حرارة الغشاء بالإضافة إلى الضغط الجزئي للأكسجين في جانبي الغشاء. وأجريت عمليات توازن الموائع الحسابية CFD باستخدام برنامج FLUENT 12.1في حين يتّبع انتقال كتلة الأكسجين من خلال الغشاء نموذجا خاصا تم تطويره في هذا البحث. تم التحقق من صحة نتائج النموذج بالمقارن مع بيانات تجريبية سابقة وأظهرت المقارنة اتفاقا جيدا مع النتائج .علاوة على ذلك، أجريت الدراسة لتكوين الخليط الأمثل لغاز الاكتساح من أجل الاحتراق البارد (الخلط) داخل المفاعل. وأخيرا تم دمج نموذج الغشاء مع مفاعل غشاء النقل الأيوني (ITM) كغرفة احتراق عن طريق استخدام احتراق غاز الميثان كيميائيا مباشرة إلى نواتج الحريق بخطوه واحده. واظهرت النتائج ان هناك زيادة كبيرة في تغلغل الأكسجين في حالة الاحتراق مقارنة مع الاحتراق البارد (الخلط).

درجة الماجستير في العلوم

جامعة الملك فهد للبترول و المعادن

الظهران المملكة العربية السعودية

CHAPTER 1

INTRODUCTION

1.1 Research Background

Most of the energy used worldwide is derived from fossil fuels. Combustion of fossil fuels leads to emissions of CO_2 into the atmosphere, which is known to contribute to the undesired global warming. It is generally accepted that the increase in the temperature of the earth is linked to the increase in greenhouse gases, mostly CO_2, in the atmosphere. Saudi Arabia has ratified the Kyoto protocol [1], which sets strict limits on emissions of CO_2 and imposes penalties.

CO_2 is a major greenhouse gas released whenever fuels containing hydrocarbon, such as methane, are burned. Most of the world’s energy needs are currently met by combustion of hydrocarbon fuels. Renewable energies are carbon neutral and present a favourable solution to the problem of greenhouse gas emissions. Unfortunately renewable energy technologies are currently not mature enough in comparison to fossil fuel based technologies. Much work is required before such energy sources will produce a major portion of our energy. Another method of power production is nuclear technology that does not contribute to the global warming problem. However acceptance of nuclear power by the public is quite low, particularly in Saudi Arabia.

Fossil fuels are heavily used in power industry as it is relatively cheap and abundant. The Hubbert oil peak is the maximum production of oil. In theory it coincides with the midpoint of the available oil in a region. Various current estimates place the world peak between 2009 and 2035 [2], implying that there is at least as much oil still available in the world as has been consumed since the industrial revolution. The discovery of methane hydrates in vast quantities indicates that fossil fuel will continue to be used for decades to come. Unfortunately combustion of these fuels produces pollutants and CO_2, the main contributor to global warming. One of the main challenge facing engineers now is how to reduce or prevent the negative impact of CO_2 on the climate caused from power plants, while allowing the continued use of fossil fuels for power production.

Carbon capture and sequestration (CCS) means capturing CO_2 and trapping it away from the atmosphere. There are many methods of sequestering CO_2 either by utilization in industrial processes or by storage underground or in deep seas. Enhanced Oil Recovery (EOR) is another option which involves injecting CO_2 into partially depleted oil wells to increase oil production. This is currently common practice in many oil companies. Over 40 Million cubic feet of CO_2 can be injected daily into oil well in Ghawar, Saudi Arabia by 2012 which was reported by Minister of Petroleum, Saudi Arabia [3].

CO_2 is also utilized in Enhanced Coal Bed Methane Recovery (ECBM) for harvesting methane from unmineable coal by injecting CO_2 into the coal bed. The neutralization of alkali pollutants can be done by using CO_2 in polluted areas. Yet another method is to absorb CO_2 into coal beds that are inaccessible and cannot be mined. Some minerals will react with CO_2 to form a solid product. There are two methods of doing this; the first is mining the reactant mineral and the second is reacting it with CO_2 to produce a product which can be used in road pavement, or injecting CO_2 into subterranean caverns containing the reactant mineral, and allowing it to slowly react over time. Other methods of CO_2 storage include injection into some geological formations, particularly porous rock. Calculation of storage capacity can be done of various types of geological formation. Akinfiev et al [4] presented theoretical calculations for formation of methane by a reaction of CO_2 with Fayalite, an abundant mineral, and discussed the possibility of a closed carbon cycle. In effect, Fayalite becomes a fuel, with methane being the energy carrier, and no emissions to the atmosphere. Many studies are being undertaken on sequestration, and many numerical simulations have been developed and tested [5, 6].

Until now many methods have been proposed for capturing CO_2 produced by combustion of fossil fuels for production of electricity. The fuel may be burned in air, and the exhaust products separated to capture CO_2. This usually involves either cryogenic or chemical processes, or use of membranes to separate gases. These methods are costly and consume a large amount of energy, thus resulting in reducing the power plant efficiency. Alternatively, carbon may be removed from hydrocarbon fuel before combustion, for example by conversion of methane to syngas, a mixture of carbon monoxide (CO) and hydrogen (H_2), followed by separation of H_2 from the mixture. It is possible to produce pure H_2 by this method, so that the H_2-using technology is emission free. However it is difficult to separate CO from H_2 as both are gases and the remaining CO will contain some unseparated H_2. This mixture is also an energy rich fuel source, and CO_2 will be produced by burning this CO-rich syngas. Another method is to use O_2 only instead of air for combustion which gives CO_2 and H_2O as flue gases and by condensation process H_2O can be easily separated and CO_2 can be sequestrated as discussed in this section. Separation of O_2 from air takes large amount of energy by conventional air separation technology. The other alternative to separate O_2 from air is use to Ion Transport Membranes (ITM) by which power loss in very low compared to cryogenic methods. In the present work, the use of ITM in order to separate O_2 and its integration as combustion chamber is studied which can retrofit the conventional gas turbine combustion chamber to ITM reactor. This concept utilizes a high temperature mixed ionic and electronic conducting ceramic membrane to separate O_2 from air and in some cases concurrently oxidizes the fuel within the same reactor which can reduces the size and can enhance the oxygen separation. However, many implication and operational constraints imposed by using ITMs within a power cycle still need to be addressed, and the thermodynamic penalty must be accessed before the benefits of ITM technology can be realized. In order to study whether or not these systems can fit into present power cycles numerical simulation is a good approach. Numerical solution of this kind of reactor can help to understand the feasibility of using this technology in power cycles.

1.2 Problem Statement

The problem considered in this work is that of an oxygen transport reactor of cylindrical shape in which a mixture of CH_4 and CO_2 (sweep gas) are injected from one side and the oxygen permeates through the ITM walls of the combustor. The combustion products are discharged through the other end of the combustor. The study will focus on the following:

1. Investigating the effect of the oxygen partial pressure in the air side on the oxygen permeation rate through the ITM and validation of the computational model against the experimental data available in the literature.
2. Studying the effect of con-current and counter-current flows of sweep gas on oxygen permeation for cold combustion
3. Investigating the effect of the sweep gas composition on the oxygen permeation rate through the ITM and the size and geometry of the resulting combustion zone.
4. Investigating the effect of combustion in the oxygen transport reactor and the effect of oxygen permeation rate through the ITM.

1.3 Objectives

The objectives of the thesis are listed below:

1. To develop a model for permeation of oxygen through Ion Transport Membrane (ITM) by creating source and sink terms at the membrane boundary cells in the continuity and species transport equation.
2. Validation of the model developed using experimental data from the literature.
3. To study the influence of partial pressure and gas temperature on oxygen permeation through the ITM.
4. To study the effect of con-current and counter-current flows of sweep gas on oxygen permeation.
5. To simulate the combustor of an oxygen transport reactor on a cold-combustion basis and to study the influence of the CO_2/CH_4 ratio on oxygen permeation rate from rich to lean mixtures.
6. To simulate the oxygen transport reactor for combustion with one step reaction with methane and to study the influence of CO_2/CH_4 ratio on O_2 permeation and to determine the amount of methane required for the present combustor.

1.4 Thesis Outline

This thesis contains six chapters.

Chapter 1 introduces the subject of Carbon capture and Sequestration and importance of Oxy-fuel combustion to mitigate greenhouse gases specially CO_2. The utilization of CO_2

in various industrial processes is also presented. The problem statement and objectives of the present thesis are discussed.

Chapter 2 is mainly a literature review and is divided in four sections. First section is about carbon capture methods and the second section focuses on oxyfuel combustion in power cycles. The third section is about the membrane separation technologies used for these CO_2 capture operations and viability of these systems in power cycles. The last section highlights the numerical schemes that were applied by previous researcher for separation technologies.

In Chapter 3, a membrane permeation model has been developed in order to study separation of O_2 from air by using different compositions of inert sweep gas. It also explains the combustion methodology that has been adopted (single step chemistry) to create the reducing environment when fuel is used as sweep gas.

In Chapter 4 the numerical method used for solving the flow, species transport and combustion processes is discussed. The results of grid independence test and validation of the C.F.D code are presented.

Chapter 5 is divided into two sections. The first section focuses on discussion of reslts in the case of cold combustion and the second section focuses on discussing the results in the case of combustion.

In Chapter 6, the conclusions of this study are presented. The recommendations of possible future research in this area also presented.

CHAPTER 2

LITERATURE REVIEW

The literature review presented in this chapter is divided into four sections. The first section presents the research done in carbon capture and sequestration technologies and the attempt of changing from air-fuel combustion to oxyfuel combustion in power generation systems and the economic viability of these systems. In the second section, the research work accomplished to use the oxyfuel process in power cycles. In the third section, the research carried to develop alternatives to replace the air separation unit by membrane reactors which save a good amount of power. The last section of this chapter presents the numerical work carried out to model separation of species from a mixture of gases.

2.1 Carbon Capture and Sequestration technologies

The statement given by IPCC [7]: 'Emissions of CO_2 due to fossil fuel burning are virtually certain to be the dominant influence of the trends in atmospheric CO_2 concentration during the 21st century'. CO_2 is considered to be the greenhouse gas that makes the largest contribution from human activities. With the on-going debate on global warming and climate changes there is a clear incentive to investigate strategies to reduce the emissions of CO_2 to the atmosphere. One way to achieve this is to remove CO_2 from exhaust gases from the power plants and store it away from the atmosphere, i.e. CO_2-capture and sequestration.

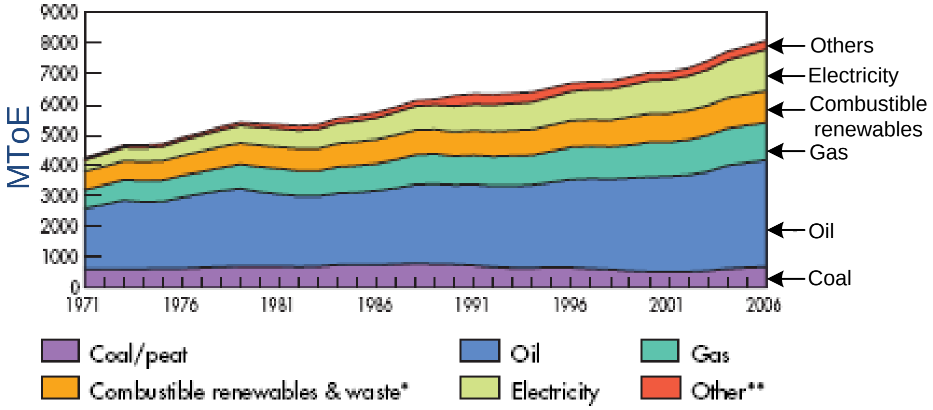

Figure 1 World Energy consumption based on usage based on the types of fuel (Mtoe) [8]

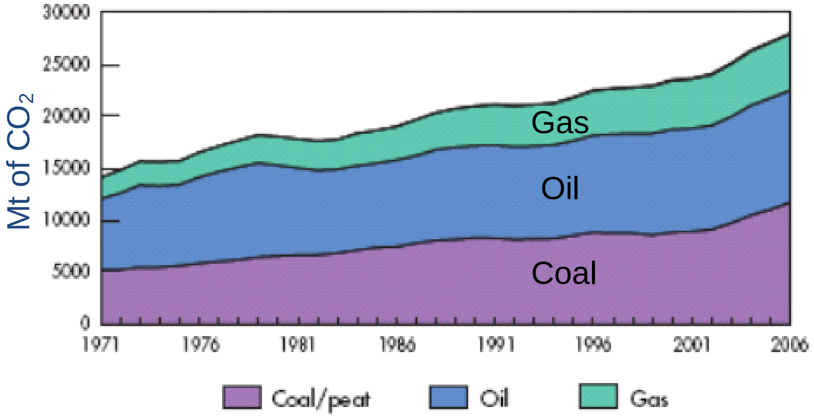

Figure 2 World CO_2 emissions from different types of fuels (Mt of CO_2) [8]

Figure 1 show how the world energy is produced in the last few decades [8]. As most of the energy is produced from fossil fuels, this also causes an increase in CO_2 emissions which can be seen clearly in Figure.2. According to IPCC [9], the average yearly growth in CO_2 emissions during the period 1995-2001 was 1.4%, a number that was higher than the five year period before that.

In this thesis, CO_2-capture and storage will be referred to as CCS. When considering combustion of fossil fuels, it is required to separate CO_2 from flue gases and store it somewhere away from the atmosphere. While capture of CO_2 is possible for all types of combustion, it is only considered to be viable for large power (or industrial) plants. Capture of CO_2 from, for instance, an automobile engine would be very expensive, and it would also be a major problem to gather all the captured CO_2 and store it. Figure 3 shows four different concepts to achieve CO_2 capture. One is an industrial plant where CO_2 is separated from the flue gases in the process. The other examples are power plants, for which there are three different approaches for carbon capture; post-combustion, pre-combustion and oxy-fuel. These approaches will be discussed in more detail below. The common process in all of these approaches is the handling of the captured CO_2. For transportation of $CO_{2,}$ it should be compressed and possibly liquefied to reduce its volume. Several options are available as storage sites, but only deep ocean and large geological formations are considered to be large enough to handle the required quantities. Depleted oil and gas fields have been suggested as a promising storage place as discussed in the introduction. Oil wells are already drilled, and equipped for injection to the underground, thus become appropriate sites for CO_2 sequestration. Another advantage of CO_2 injection in oil wells is its usage in enhancing oil recovery.

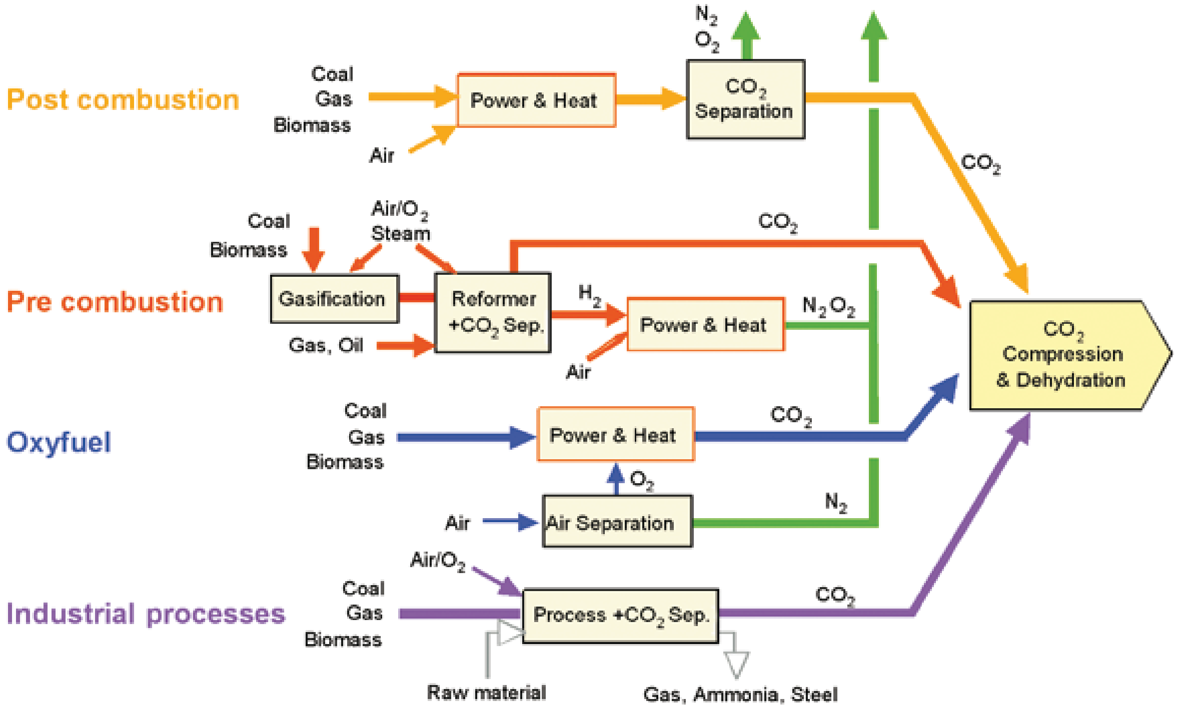

Figure 3 CO_2 capture system [9]

2.1.1 Pre-combustion capture:

Decarbonisation of fuel gas is done in pre-combustion systems. In chemical and refining industries, this process has been used for hydrogen production for more than five decades [10]. In this type of systems, the primary fuel is processed in a reactor in the presence of steam and air (or oxygen) to produce a mixture consisting mainly of carbon monoxide and hydrogen (synthesis gas). The reaction between the carbon monoxide with steam in a second reactor (a "shift reactor") produces additional hydrogen and CO_2. The resulting mixture of hydrogen and CO_2 can then be separated into a CO_2 gas stream, and a stream of hydrogen. If CO_2 is stored, the remaining hydrogen is a carbon-free energy carrier that can be combusted to generate power and/or heat with no CO_2. Although the initial fuel conversion steps are more elaborate and costly than that of post-combustion systems which is discussed in later sub-section, the high concentrations of CO_2 produced by the shift reactor (typically 15 to 60% by volume on a dry basis) and the high pressures often encountered in these applications are more favourable for CO_2 separation. Pre-combustion can be used in natural gas or coal based plants that employ integrated gasification combined cycle (IGCC) technology as can be seen in Figure 4.

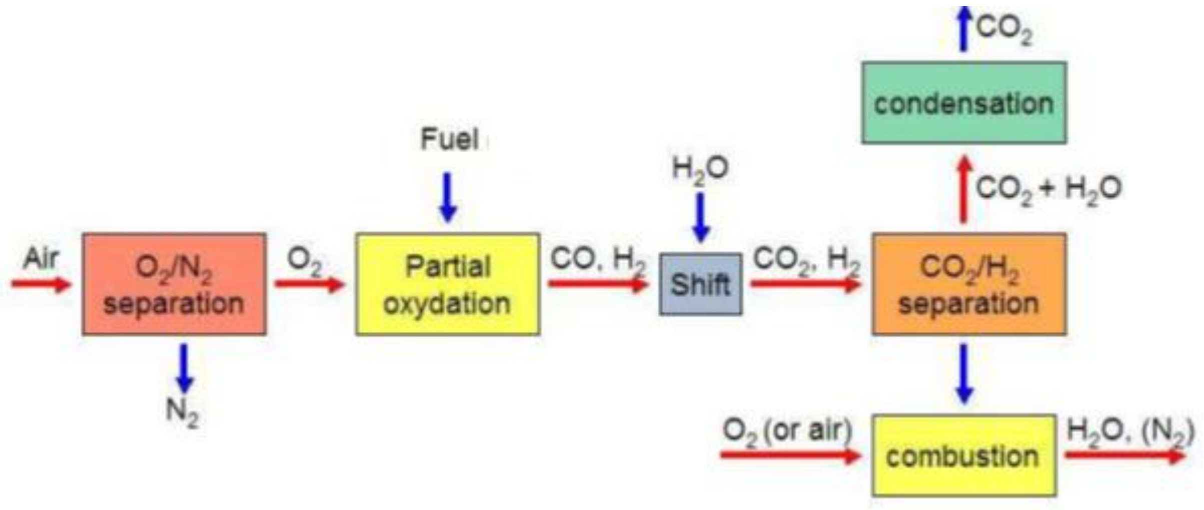

Figure 4 Pre-combustion process [9]

2.1.2 Post combustion capture:

It involves separation of CO_2 from the flue gases produced by the combustion of the primary fuel in air. These carbon capture systems normally use a liquid solvent mostly amines- to capture the fraction of CO_2 present in the flue gas stream by a chemical reaction. The flue gas must contain very low levels of oxides of nitrogen and sulphur (NO_X and SO_2) to form stable, non-regenerable salts in reaction with the amine. This means that post-combustion CO_2 capture on coal fired power plants requires upstream de-NOx and flue gas desulphurization (FGD) facilities. The solvent is then regenerated.

For a modern pulverized coal (PC) power plant or a natural gas combined cycle (NGCC) power plant, current post-combustion capture systems would typically employ an organic solvent such as monoethanolamine (MEA) [9, 10, 11, 12].

The requirement of heat for the current generation of solvents is high and has a major impact on the overall efficiency of the power plant since steam which would otherwise generate power in the LP turbine of the plant is now used to regenerate the solvent instead. Integration of the heat cycle of plants fitted with post-combustion capture is essential to minimise the impact of the capture process on the overall plant efficiency [13].

2.1.3 Oxyfuel Combustion:

Oxyfuel combustion systems use oxygen instead of air for combustion of the primary fuel to produce a flue gas that is mainly consisting of water vapour and CO_2. Normally, the flue gas has high CO_2 concentrations and by cooling and compressing the gas stream, water vapour can be removed easily. It may have potential as a part of a system for capturing and storing CO_2 as the nitrogen concentration in the flue gas is much lower than that in case of using air for combustion. So, the CO_2 can be stored with less downstream processing. Oxyfuel combustion systems are, in principle, able to capture nearly all of the CO_2 produced. However, the need for additional gas treatment systems to remove pollutants such as sulphur and nitrogen oxides lowers the level of CO_2 captured to slightly more than 90%. The most widely considered technology for oxygen production is cryogenic air separation. The auxiliary power consumption of a cryogenic air separation unit is high and has a major impact on the overall efficiency of the power plant. Further treatment of the flue gas may be needed to remove air pollutants and non-condensed gases (such as nitrogen) from the flue gas. As a method of CO_2 capture in boilers, Oxyfuel combustion systems are in the demonstration phase. Oxyfuel systems are also being studied in gas turbine systems, but conceptual designs for such applications are still in the research phase [9] and the related flow diagram can be seen in Figure 5. Integration of the thermodynamic cycle of plants fitted with Oxyfuel capture is essential to minimise the impact of the capture process on the overall plant efficiency.

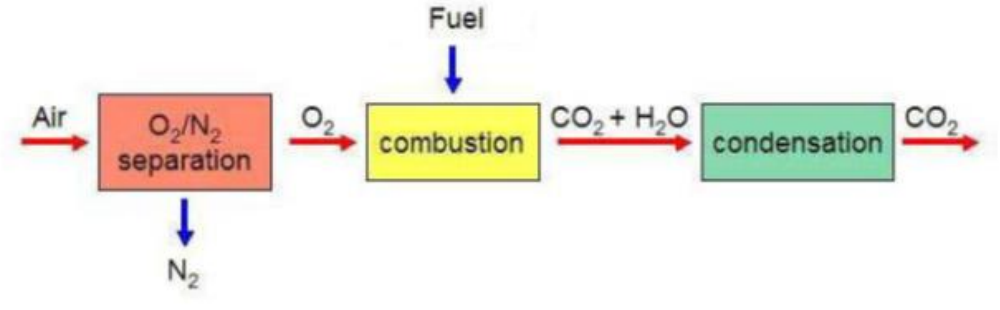

Figure 5 Oxyfuel Process [9]

Among all capture methods, CO_2 scrubbing techniques are the most mature. MEA-based scrubbing has been utilised for more than 60 years for natural gas purification and food-grade CO_2 production. In particular, Rectisol and Selexol processes have been commercially used since the 1990s for CO_2 capture in the refining, chemical and fertilizer industries and are today extensively used in gasification plants to purify synthesis gas for downstream chemical applications. Current units, using these techniques, are able to remove thousands of tonnes of CO_2 per day [14]. However, they have not yet been demonstrated on the large scale necessary for 90% CO_2 capture from a typical 500MW coal fired power plant where 10000–15000 tons of CO_2 would be removed per day.

Other capture technologies such as anti-sublimation, enzymes and algae for post-combustion and chemical looping and high pressure oxy-reactor are still at an early stage of development, with commercial deployment generally considered to be unlikely before 2025.

2.1.4 Economic viability:

The study of economic viability of these technologies is an important issue that has to be considered. Since the coal fired power plants generate high rate of flue gases but with low CO_2 concentration. There is huge capital investment needed to install the post combustion systems for massive volumes of flue gases in the present conventional power generation systems. Since most of the processes for CO_2 capture is energy intensive, pre-combustion or oxyfuel processes are viable processes which lies within low investment.

The Air Separation units (ASU) which uses cryogenic process to separate of oxygen and nitrogen may alone consume about 13% of the power plant output [15]. On the other hand gas separation membranes have relatively low energy consumption and their integration into membrane reactors is very promising. Therefore, they are excellent for gas separation in retrofitting coal-fired power plants and the oxyfuel combustion power plant.

2.2 Oxyfuel combustion in power cycles

In his paper, Kvamsdal et al [16] reported a comparison of power plant overall efficiency utilizing different CO_2 capture techniques with that of conventional power plant with no CO_2 capture as shown in Figure 6. The figure indicates a maximum efficiency of 57% for conventional power plant with no CO_2 capture. It can be seen that technology progresses towards 100% CO_2 capture with higher efficiency. Out of many cycles shown, Advanced Zero Emission Process (AZEP) cycle showed maximum carbon capture with very low efficiency penalty. It 85% CO_2 capture the efficiency penalty was 4% compare with no CO_2 capture and with 100% CO_2 capture it was 7% . From the technical side, the oxyfuel process can be applied to the existing coal-fired power plants and we can build new one with only oxyfuel combustion chambers [17]. The new technology of membrane separation and combustion is not yet fully matured to commercialize to manufacture a large scale power production unit.

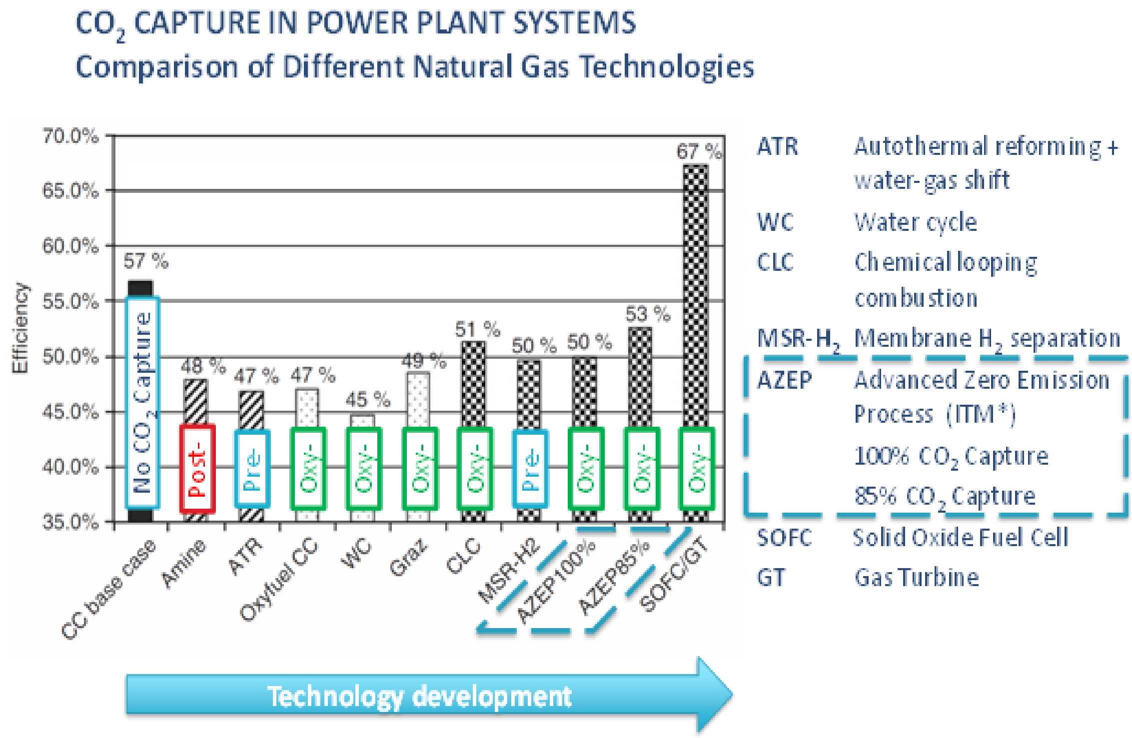

Figure 6 various technology showing efficiencies [16].

However, the efforts put by the researchers [18, 19, 20, 21, 22] show great potential to implement this membrane integration with oxy-rich fuel combustion. Several aspects of oxyfuel processes for use in coal-fired power plant are currently under investigation, e.g. boiler design, combustion reactions and chemistry of combustion, sealing issues for Oxygen Transport Reactor (OTR) in order to to make this technology more viable. Vattenfall a Sweden based company has commissioned the world's first coal-fired plant with CO_2 capture technology in September 2008 with a thermal capacity of 30 MW [23]. The idea of this oxyfuel combustion can be extended to natural gas combustion with membrane integration in a combustion chamber. More work has to be done for clarification of combustion issues such as reaction kinetics, ignition (in case of coal-fired), flame stability, sealing of membrane and the activation energy required for operating these OTR.

2.2.1 Combustion in power cycle

The combustion oxidizer generally used for oxyfuel processes should have a purity of more than 95% and the rest being nitrogen [24, 25]. In coal-fired combustion there must be excess oxygen supplied to the boiler which is necessary to obtain a stoichiometric and homogenous combustion. In the flue gas, there will be CO_2 along with H_2O vapours with small concentration of NOx, SOx, etc. The boiler flue gas is sent to a clean-up process to remove acid gases and particulates. Then it is again treated for NOx removal in deNOx treatment unit, this NOx generation due to the air-leakage in boiler which accounts to 8%-15% [24]. SOx treatment is also necessary for the removal of sulphur inside the boiler [26, 27]. After complete dehumidification of the flue gas, it is estimated that the purity of remaining CO_2 ranging 85% to 95% [18, 28, 11] and is ready for compression and storage.

If the combustion is done with natural gas (mainly methane) in an oxygen transport reactor then the process of DeNOx and DeSOx treatment can be avoided since with membranes supply very high purity of oxygen and the leakage is also negligible compared to boiler furnace. Since the oxygen flames give higher temperatures that should be controlled, around 2/3 of the flue gas need to be recycled [17]. The missing element of N_2 is replaced by recycled CO_2 which will carry away the heat and will increase the concentration of CO_2 [27]. Moreover, the recycled CO_2 is used to sweep out the permeate side of the membrane thus lowering the oxygen partial pressure and allowing the required gradient of O_2 partial pressure across the membrane.

2.2.2 Flue Gas Composition:

The work done by Kakaras et al [25] for lignite fired power plant with oxyfuel boiler shows a composition of 66% of CO_2 by weight and 19% of H_2O and N_2 and Ar of 8% and O_2 is 1% at boiler exit. The emission analysis done by Fabienee et al [26] for a small lab scale plant with a capacity of 1.5 MW showed flue gas composition of 80% CO_2, 17 % N_2, and 3% of O_2. The study done by Singh et al [11] indicated that for the 400 MW pulverised coal-fired power plant, the dry flue gas composition was 91% CO_2, and 75% CO_2 on wet basis. These studies showed that the ideal O_2 to CO_2 ratio in the feed is 30/70 with around 50% recycled flue gas which will lead to CO_2 purity of more than 97% [21, 22, 27].

In general oxyfuel combustion process in which oxygen is separated and feed to the combustion chamber, is considering two mechanisms for the flue gas recirculation. The first mechanism is called “wet recycling”, the flue gas is recycled directly after clean-up processes removes particulates and acid gases. The swept gas will be mainly composed of water and CO_2. The second mechanism is “dry recycling” in which water is removed from the flue gas by condensation. This condensation doesn’t remove all water but after condensation the flue gas passes through molecular sieves to eliminate the water completely [28]. The schematics of the two mechanisms are shown in Figure 7 and 8.

In case of Oxygen transport reactor in which O_2 permeation and combustion takes place at the same time, the recycled CO_2 will play a major role in controlling the temperature of the reactor and increasing the CO_2 concentration at the exit of the combustor.

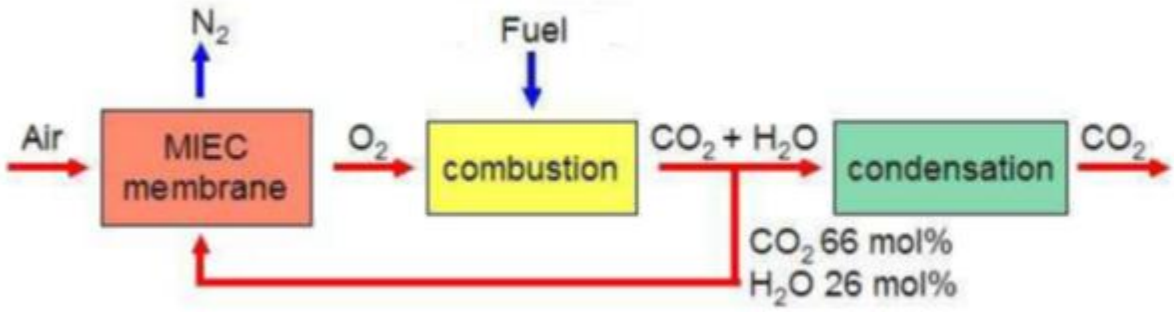

Figure 7 Oxyfuel process with water condensation [25]

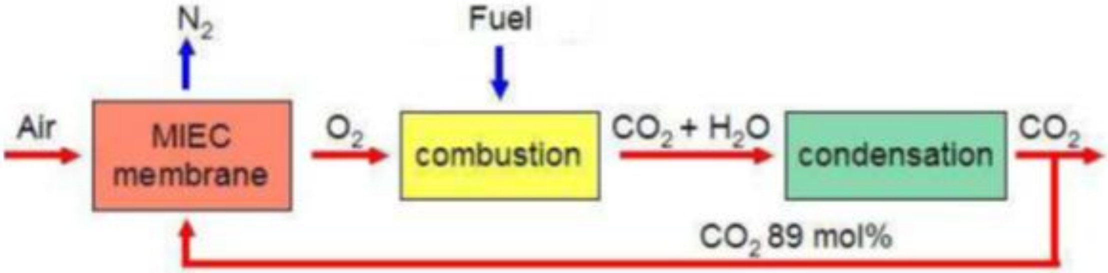

Figure 8 Oxyfuel process without water condensation [28]

2.2.3 Oxyfired power plants incorporating oxygen transport membranes (OTM):

A number of configurations are designed and some are installed while others are under laboratory testing. In 2005, the world's first oxyfired power plant was installed in Kamberlina, California, USA by Clean Energy Systems (CES) [29].

As stated earlier, the cryogenic air separation is accompanied by huge loss of efficiency of oxyfired cycles. The air separation with cryogenics requires air compressing and then cooling to very low temperature of about -183^{o}C which liquefies oxygen for separation from nitrogen. The liquefied oxygen is then heated and used in oxyfired cycles; the whole process accounts of 13% loss of efficiency [15]. However, OTMs offers oxygen production without high adverse effect on efficiency. Oxygen transport Membranes have been incorporated in power cycles and a well-developed example is Advanced Zero Emission Power (AZEP) cycle [30] as shown in Figure 9. In this cycle, air after being compressed, it is split into two parts. The first of is used to heat steam and air, while the other part is mixed with oxygen in OTM unit which is sometimes called as Mixed Conducting Membrane reactor (MCM) in the figure 9 and returns to the combustion chamber as oxidant. The membrane conducts oxygen to the fuel side and heats the air side. The membrane doesn’t have to withstand flames since combustion occurs away from the membrane wall, but hot combustion products enters the OTM reactor at temperature close to adiabatic combustion temperature. The oxygen depleted turbine (main turbine) drives both air compressor and the electrical generator. The combustion products are used to heat the working fluid in the Rankine cycle and are then cooled to condense H_2O after boiler leaving only CO_2. The thermal efficiency of AZEP cycle was is compared with conventional combined cycle power plant and it was found to be about 8.3% lower [31].

This efficiency loss is mainly due to the reduced inlet turbine temperature which was about 1200 ^{o}C and it causes significant amount of power loss both in steam and gas turbine. The efficiency of the cycle was claimed to increase, by increasing the inlet turbine temperature which can be done by additional fuel firing in the heated air steam before the gas turbine, from 50% to 54% [31] but with a penalty of CO_2 capture which was about 8.5%. The other cycle which was developed with OTM is Oxycoal-AC cycle in Germany. By the name suggests pulverised coal is used as fuel. The combustion products provide heat to air stream and bottoming Rankine cycle. In this cycle, air turbine drives the compressor and the power is generated in bottoming cycle only. The efficiency of the cycle was reported 41.6% with 4-end concept and 39.7% with 3-end concept [32]. The 4-end concept and 3-end concept is described in the next paragraph and shown in Figure 10 and 11.

Stadler et al [33] carried out research on oxyfuel coal combustion by efficient integration of Oxygen Transport Membranes for possible implementations of OTM into an Oxyfuel process through three-end and four-end integration of membranes. He focused on the overall cycle efficiency for different level of integration which includes low, medium, high integration, high integration with fogging and Co-firing. The four-end concept refers to the application of sweep stream on the low pressure side in order to remove the permeating component and thereby increasing the driving potential whereas in the three-end concept vacuum is applied at the permeate side and can be seen figure 12.

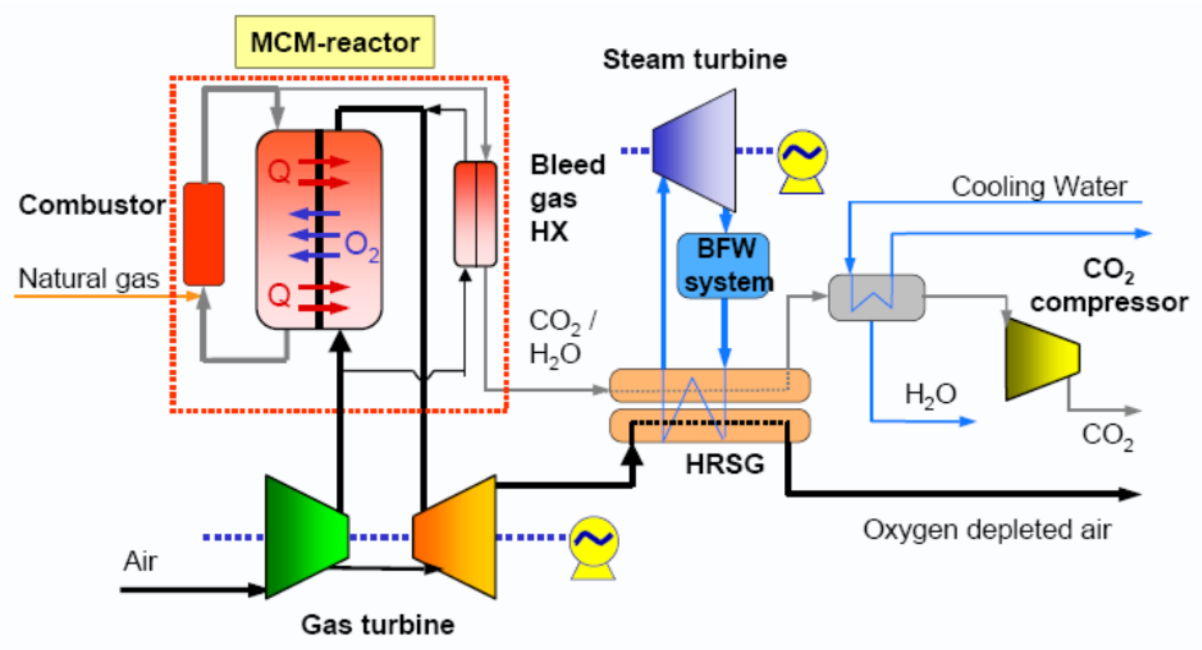

Figure 9 AZEP Oxyfired cycle incorporating OTM [30]

The OTM materials used in the analysis was BSCF. The operating temperature of the membrane was about 825^{o}C and the mean oxygen partial pressure ratio was in between 3 and 26. The oxygen flux across the membrane is determined by the following Wagner-equation

$$J_{O_2} = \frac{C_{wagner} T_{membrane}}{d} \exp\left(\frac{-K_{wagner}}{T_{membrane}}\right) \ln\left(\frac{p_{o_{2,feed}}}{p_{o_{2,permeate}}}\right)$$

where C_{wagner} and K_{wagner} are membrane material properties and constants which can be determined experimentally.

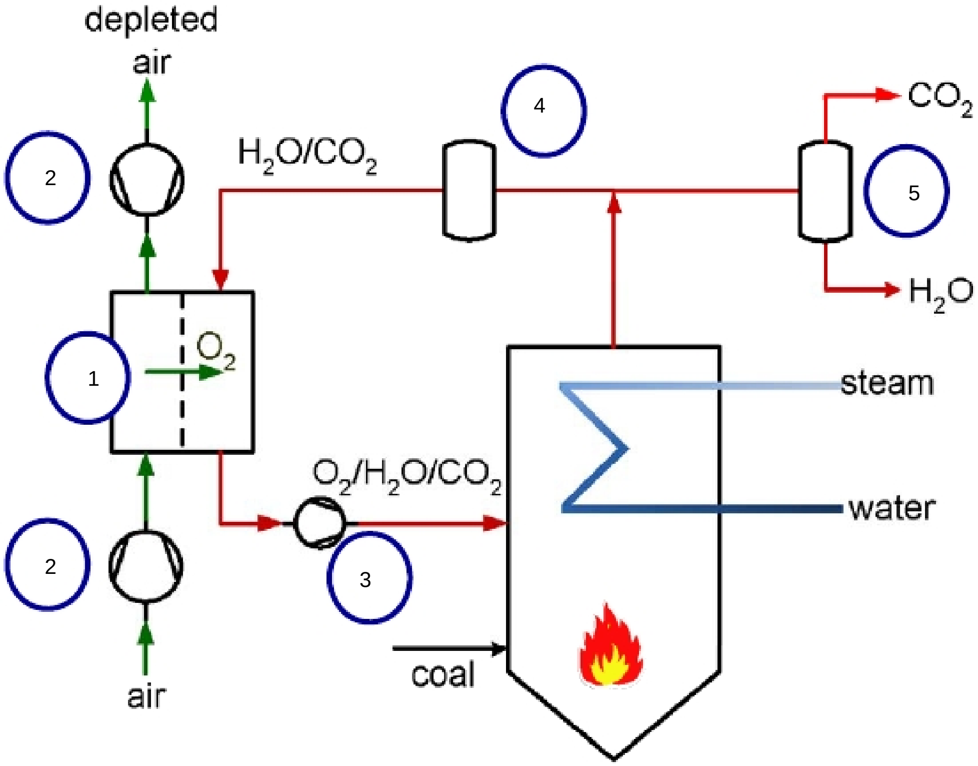

Figure 10 4-end integration system [32]

1. Membrane 2. Coupled turbo components 3. Recirculation fan 4. Hot flue gas cleaning 5. CO_2 conditioning

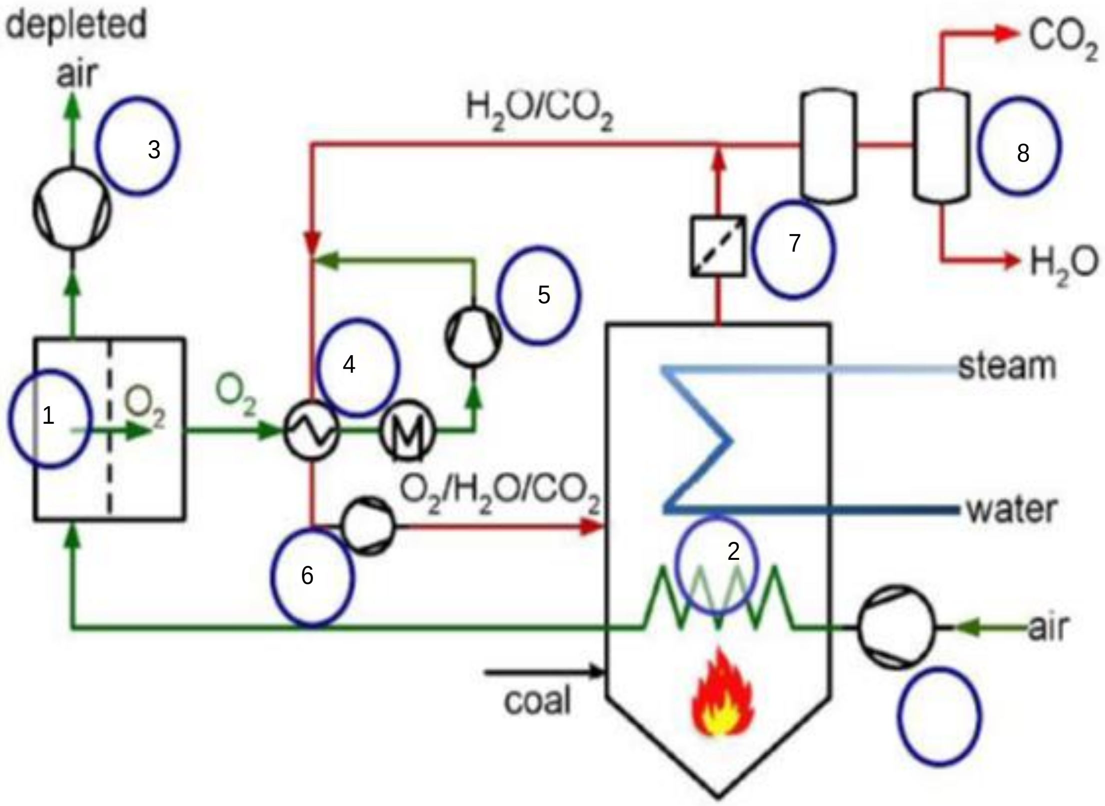

Figure 11 3-end system integration [32]

1. Membrane 2. Air preheater 3. Coupled turbo components 4. O_2 cooler 5. Vacuum pump 6. Recirculation fan 7. Flue gas cleaning 8. CO_2 conditioning.

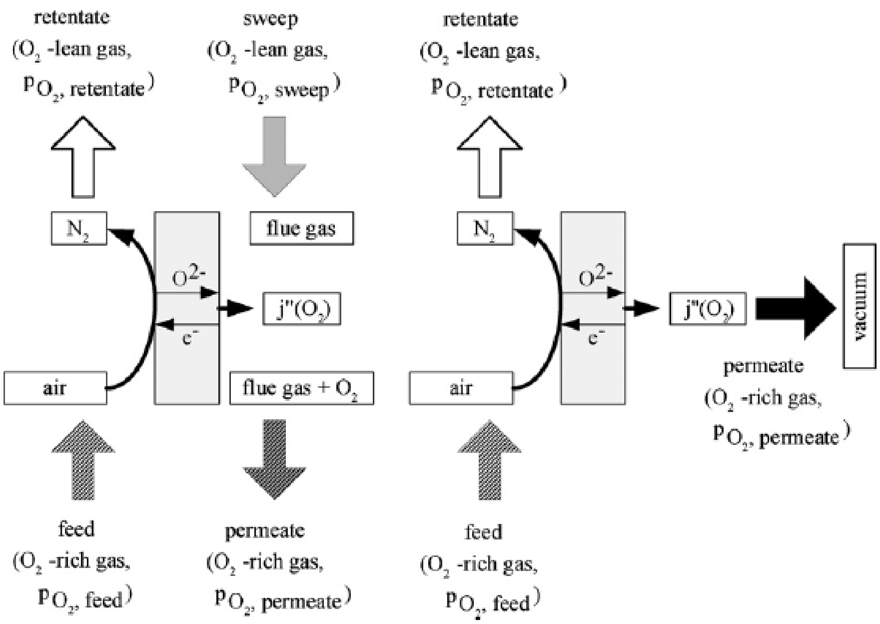

Figure 12 Oxygen Conduction in OTM in four-end design (left) and three-end design (right)

It’s was expected that the efficiency can be improved through optimisation of membrane operation parameters such as oxygen separation degree, the partial pressure ratio and the total pressure ratio. It was found from the analysis that the oxygen concentration varies linearly with the separation degree and with 90% separation degree, 16.5 vol% concentration of oxygen and with the partial pressure ratio of 26 the adiabatic flame temperature achieved was about 1500^{o}C. The analysis gives quite evidence of the four-end design got more capability of producing high efficiency than three-end design shown in figure 12. The critical remarks found are the membrane material stability at high elevated temperatures and permeability of the membranes which affects the overall efficiency of the plant.

The concept developed by E Yantovski [34] for oxyfired power plant with zero emission resulted in a new cycle called ZEITMOP (Zero Emission Ion Transport Membrane Oxygen Power) cycle. This cycle is shown in Figure 13 and was developed to work on all type of fossil fuels. The cycle has three turbines, one for combustion products, second for depleted oxygen and third for CO_2 recirculation through the system.

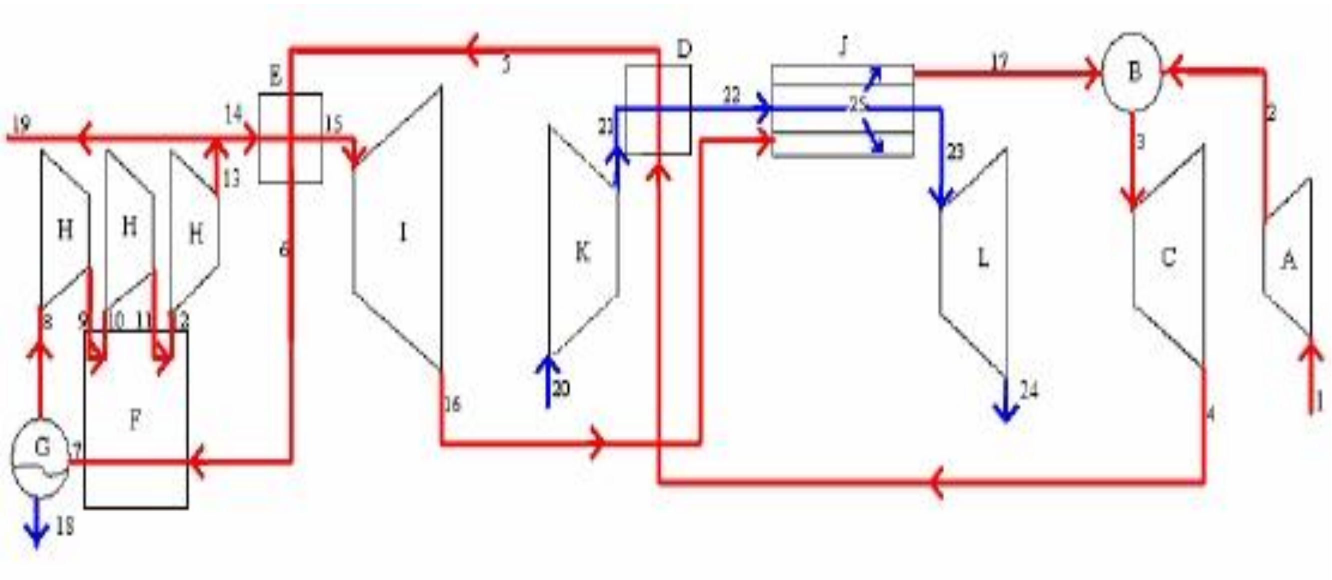

Figure 13 The ZEITMOP cycle in which OTR is remote from Combustion chamber [33]

Methane (1) is compressed in compressor A (2) and burned in combustion chamber B in a mixture of O_2 and CO_2 (17). The exhaust products (3) are expanded in turbine C (4) and are then cooled in two heat exchangers D and E (5,6) before being further cooled in cooling tower F (7), causing the water in the combustion products to condense. Th liquid water is separated in water separator G and removed (18) leaving almost pure CO_2 (8). The CO_2 is compressed in a three stage compressor H with intercooling in the cooling tower F to 210 bar (9-13) and the portion born of combustion is captured (19). The rest of the CO_2 (14) is heated in heat exchanger E (15) and expanded in turbine I (16) before entering the OTM unit J where it is mixed with O_2 (25), then returns to combustion chamber B (17). Air (20) is compressed in compressor K (21) and heated in heat exchanger D (22) before entering OTM unit J in which the O_2 required for combustion (25) is separated. The hot depleted oxygen air is expanded in a turbine L (23) before it is being discharged to atmosphere. The water and CO_2 produced from combustion was in liquid phase hence they are considered as effluents, not emissions. The water can be removed totally in separator G and CO_2 is captured and sequestrated.

The approximate pressure and temperature obtained in the range 15 to 40 bar and 800 to 900^{o}C for oxygen separation through dense, nonporous, mixed-conducting ceramic membranes. The paper shows how the efficiency varies with different cycle selection and implementation of ITMs. To show the feasibility of ITMs, the numerical analysis of ZEITMOP power cycle with separate combustion and ITM reactor was done [33]. The economic issue such as cost of manufacturing membranes and oxygen flux at 900 ^{o}C were discussed. For the combustion temperature range of 1000-1400 ^{o}C, thermal efficiency obtained between is in the range of 46%-52% with CO_2 circulation.

Foy [35] carried out a computational analysis for the combined OTR and combustion chamber in ZEITMOP cycle as shown in Figure 14. The ZEITMOP-Combined cycle was simulated at a combustion pressure of 15 bar and combustion temperatures of 1000°C (which would be the likely maximum combustion temperature if perovskite membranes were used) and 1400°C. It is similar to the previous cycle but the average working temperature in which OTR was changed with separate module and combined module of OTR. The combined ZEITMOP cycles showed a realistic behaviour and more work is needed to optimise the cycle efficiency and parameters that involve the design of OTR to work at high temperature with controlled combustion. Tzimas et al [36] investigated the impact of CO_2 capture in fossil fuel power plants on the emissions of nitrogen oxides (NO_x) and sulphur oxides (SO_x). This was done by estimating the emissions of these chemical compounds from natural gas combined cycle and pulverized coal plants, equipped with post-combustion carbon capture technology for the removal of CO_2 from flue gases, and comparing them with the emissions of similar plants without CO_2 capture.

It was indicated that the NO_x emissions from the power generation sector are likely to increase when carbon capture technologies are implemented on a large scale, due to the reduced efficiency of such power plants.

For optimizing the thermal efficiency of the cycle, many formats can be selected for CO_2 capture and improving the working performance of OTR. This has very wide potential in making hybrid power plants with OTR for carbon capture and integrating with the renewable energy sources like solar. Foy's [35] work was focused on the study of combustion chamber with OTR and the result can be used to optimise the total cycle efficiency. From the above discussion it was found that there is potential in changing the technology from air-fuel to oxy-fuel is worth and that needs more research to address the problems in implementing the change.

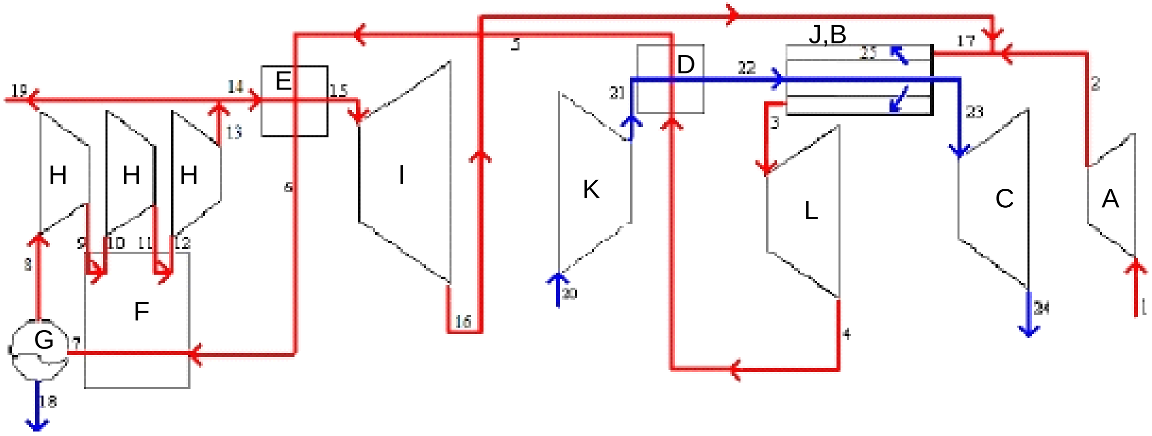

Figure 14 The ZEITMOP cycle with OTR and combustion chamber combined [35]

2.3 Membranes for gas separation in Carbon capture and sequestration

Generally there are three types of membranes currently available for gas separation applications and are considered for CO_2 capture:

- Organic porous polymer membranes.
- Inorganic porous membranes, amorphous or crystalline
- Inorganic dense membranes, metallic or ceramic

Organic polymeric membranes are excellent candidate for CO_2 separation from N_2 for the post-combustion process. These membranes can even separate the H_2/CO_2 in pre-combustion process but they have low thermal stability and not suitable for high temperature and pressure applications [37]. On the other hand dense inorganic membranes are suitable for H_2/CO_2 and O_2/N_2 separation.

2.3.1 Mixed Ionic and Electronic Conducting (MIEC) Membranes for O_2/N_2 separation:

MIEC membranes have been tested for oxygen separation from air and regarded as clean, cost effective technology. These membranes are dense in nature with no detectable pores which means that the oxygen molecules cannot pass through these membranes. These membranes have the capability of separating oxygen from air because of the oxygen vacancies in the crystal lattice which is created by doping of the material. Oxygen ions are transported from one side of the membrane to the other by a mechanism called hopping. This mechanism is activated only if the oxygen anions have enough thermal energy to overcome the energy barrier to hop from one side of the crystal lattice to the other which means that the membrane are operable at high temperatures. The typical range for the membranes to activate the mechanism of oxygen transport is 700^{o}C to 1000 ^{o}C [38]. There will be a counter-balancing electron transport to maintain electro-neutrality in the material and there is no need of any potential voltage for the oxygen transport.

2.3.2 Oxygen Transport Theory:

In ITM membranes, the oxygen transport occurs because of the partial pressure difference across the membranes. The oxygen molecules dissociated into O^{2-} anions at the high oxygen partial pressure side (feed side) and travel through lattice and released at low oxygen partial pressure side where these anions recombine again to form oxygen molecules. The oxygen flux is depended on the membrane electronic and ionic conductivity. Flux is maximum when the electronic and ionic transference number is 0.5 for fixed total conductivity. The oxygen permeation rate is controlled by two main factors, one is the rate of interfacial oxygen exchange on both sides of the membrane and other is the rate of solid state diffusion within the membrane material. The oxygen transport through the membrane involved three progressive steps: the surface-exchange reaction on interface I, the simultaneous bulk-diffusion of charged species and electron/electron holes in the bulk phase and the surface-exchange reaction on the interface II [15]. After a certain thickness of the membrane the diffusion is the rate determining mechanism and when the thickness is reduced, oxygen transport across the interfaces I and II becomes the limiting factor and the variation of thickness and the mechanism affecting it is shown in Figure 16.

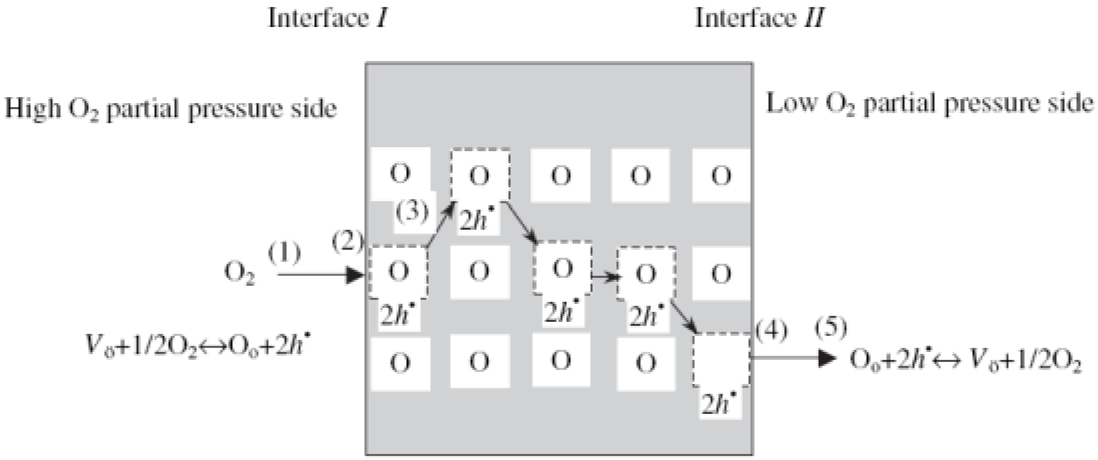

Figure 15 Different sections of ITM involved in oxygen transport during oxygen permeation

As long as the bulk diffusion mechanism is dominant, oxygen flux permeation can be increased by decreasing the thickness of the membrane. When the thickness reaches a characteristic membrane thickness L_c, the oxygen permeation is controlled by both surface exchange kinetics and bulk diffusion. For membrane thickness less than $2L_c$, the permeation flux becomes independent of membrane thickness and it can be seen figure 16. The characteristic thickness of the membrane is defined as the ratio of self-diffusivity of oxygen to surface exchange coefficient [39].

$$L_c = \left(D_s / k_{io} \right) \quad (1)$$

The transport of oxygen is influenced by many factors related to microstructure such as grain boundary diffusion and order-disorder phenomena, roughness and porosity of the membrane surface.

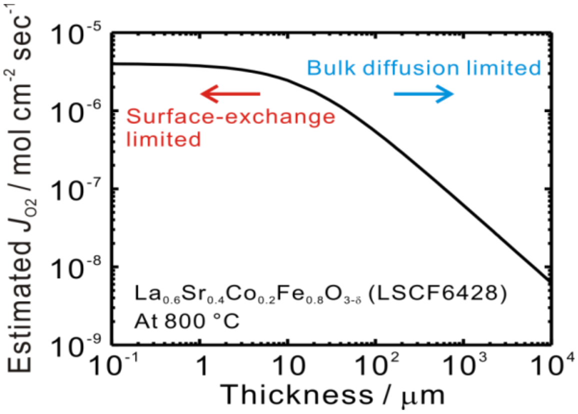

Figure 16 Variation of regime from bulk-diffusion to surface-exchange reaction limited with decreasing membrane thickness [38]

2.3.3 Bulk transport theory:

The diffusion process in the thick membrane is commonly the slowest step. The Wagner theory can be used to describe the oxygen flux J_{O_2} [40].

$$J_{O_2} = \frac{1}{16F^2L} \int_{\mu_{O_2}(II)}^{\mu_{O_2}(I)} t_i t_e \sigma_t d\mu_{O_2} \tag{2}$$

$$t_i = \frac{\sigma_i}{\sigma_e + \sigma_i} = \frac{\sigma_i}{\sigma_t} \tag{3}$$

where t_i , t_e is the ionic and electronic transference numbers respectively which are defined as ratio of electronic (σ_e) or ionic conductivity (σ_i) over sum of them.

Equation (2) has been derived by assuming that local equilibrium exists between the two charged species such as oxygen ion and electron and a hypothetical neutral species such as molecular oxygen in the bulk oxide. For consideration, at least three species can contribute to the bulk-diffusion which are (a) oxygen vacancies, (b) electrons or (c) electron holes. Each of them might be the slowest moving species and therefore limiting the oxygen flux.

2.3.3. (a) Oxygen vacancies diffusion:

In mixed ionic and electronic conducting membranes, the electronic conductivity dominates, that is $\sigma_e >> \sigma_i$, the integral of equation (2) involves only σ_i as a function of oxygen partial pressure. Assuming ideal thermodynamic system, the chemical potential can be written as

$$d\mu_{O_2} = RTd\ln P_{O_2} \tag{4}$$

Nernst-Einstein correlation [41] for the ionic conductivity is expressed as,

$$\sigma_i = \frac{4F^2 V_O^{\bullet\bullet} D_v}{RTV_m} \tag{5}$$

$$D_v = D_v^0 \exp\left(-\frac{E_a}{RT}\right) \tag{6}$$

For average value of σ_i and for small oxygen partial pressure gradient the oxygen permeation flux equation can be integrated as,

$$J_{O_2} = \frac{RT}{16F^2L}\bar{\sigma}_i \ln\frac{P_{O_2}^{'}}{P_{O_2}^{''}} \tag{7}$$

The above equation is valid for very rare cases such as the case of tubular membrane [42] working under 700°C-900 °C for partial pressure of oxygen at feed side is in between 0.09-1.0 atm.

In general, if the oxygen ionic conductivity can be correlated [43] to oxygen partial pressure in a simplified manner, then the oxygen flux can be given by,

$$\sigma_i = \sigma_i^o P_{O_2}^{-n} \tag{8}$$

$$J_{O_2} = \frac{RT}{4F^2L}\sigma_i^o\left(P_{O_2}^{'-n} - P_{O_2}^{''-n}\right) \tag{9}$$

Kim et al [44, 45] have derived generalise form of equation describing oxygen permeation through tubular perovskite membrane assuming that density of vacancies at the interfaces does not change. Equation (10) shown below is for Bulk-diffusion limited region in tubular perovskite membranes.

$$J_{O_2} = \frac{\pi w C_i D_a}{2S \ln(r_1 / r_2)} \ln\left(\frac{P_{O_2}^{'0.5}}{P_{O_2}^{''0.5}} \right) \tag{10}$$

where $D_a = \frac{\sigma_e D_i}{\sigma_e + \sigma_i}$. (11)

2.3.3. (b) Electron diffusion:

The electronic defects could be properly assumed and can be given in the equation (12). Furthermore, by using the law of mass action; equation (13) can be derived. The electronic concentration is proportional to $P_{O_2}^{-1/4}$, if the concentration of all other species (oxygen vacancies and interstitials) is much higher. Therefore, the electron concentration can be taken as constant, when $t_i \approx 1$(ionic conductivity is dominant). Therefore equation (2) can be modified resulting in equation (14). In this equation, electronic conductivity is a function of electron concentration as shown by equation (15). From the above mentioned assumptions the oxygen permeation flux is depended to -1/4th order of oxygen partial pressure and is given by equation (16). The mentioned equations are best fitted with the results of Han et al [46], and Nigara el al [47].

$$O_O^x \leftrightarrow \frac{1}{2}O_2 + V_O^{\bullet\bullet} + 2e \tag{12}$$

$$n = \frac{K_{V_O^{\bullet\bullet}}^{1/2}[O_O^x]^{1/2}}{P_{O_2}^{1/4}[V_O^{\bullet\bullet}]^{1/2}} \tag{13}$$

$$J_{O_2} = \frac{RT}{16F^2L}\int_{P_{O_2}^{''}}^{P_{O_2}^{'}} \sigma_e d\ln P_{O_2} \tag{14}$$

$$\sigma_e \approx n \approx KP_{O_2}^{-1/4} \tag{15}$$

$$J_{O_2} = \frac{RT}{4F^2L}\sigma_e^o\left(P_{O_2}^{'-1/4} - P_{O_2}^{''-1/4}\right) \tag{16}$$

2.3.3. (c) Electron hole diffusion:

The electron holes equation can be represented as follows,

$$O_2 + 2V_O^{\bullet\bullet} \leftrightarrow 2O_O^x + 4h^{\bullet}$$

(17)

Further, by using law of mass action; equation (18) can be obtained. By the same assumptions used in electron diffusion, oxygen flux equation (19) can be derived which also shows the dependence of 1/4th order of partial pressure of oxygen and this has been reported by Han et al[46], Capoen et al [48] and Dou et al [49].

$$h = \frac{K_{O_O^x}^{1/2}P_{O_2}^{1/4}[V_O^{\bullet\bullet}]^{1/2}}{[O_O^x]^{1/2}} \tag{18}$$

$$J_{O_2} = \frac{RT}{4F^2L}\sigma_h^o\left(P_{O_2}^{'1/4} - P_{O_2}^{''1/4}\right) \qquad (19)$$

2.3.4 Surface exchange- limited reaction:

This mechanism is dominant when the oxygen transport resistance in the bulk-diffusion phase becomes very small due to increase in the ionic or electronic conductivity or due to reduction in the thickness of the membrane. In this case, the Wagner equation is not applicable. Other relations were developed to explain the behaviour of oxygen transport within this regime. Dou et al [49] proposed a possible mechanism the surface reaction into bulk-diffusion as following:

$$O_{2(g')} \leftrightarrow 2O_{(w')} \qquad (20)$$

$$O_{(w')} + V_{O(w')}^{\bullet\bullet} \leftrightarrow O_{(w')}^{x} + 2h_{(w')} \qquad (21)$$

$$O_{(w')}^{x} \leftrightarrow O_{O(w'')}^{x}$$

(22) $h_{(w')} \leftrightarrow h_{(w'')}$

(23) $O_{(w'')}^{x} + 2h_{(w'')} \leftrightarrow O_{(w'')}^{x} + V_{O(w'')}^{\bullet\bullet}$

(24) $2O_{(w'')}^{x} \leftrightarrow O_{2(g'')}$

(25) Surface exchange reactions are expected to be sequential and may consist of adsorption from the gas phase, charge transfer reaction between the adsorbed species and bulk including the reversed reactions as shown in Figure 17.

If the slowest moving species considered is O^x at the interface I, and using the law of mass action, the following relation for charged and absorbed oxygen species from equation (20) and (21) applies. A proportional constant *K* represents the equilibrium constant. *K* is specific for each type of reaction as indicated in its subscript which refers to the primary product of the reaction.

$$K_{O_{(w')}} = \frac{O^2_{(w')}}{P_{O_2(g')}}$$

$$K_{O^x_{(w'')}} = \frac{[O^x_{(w')}]P^2_{(w')}}{[O_{(w')}][V^{\bullet\bullet}_{O(w')}]}$$

Therefore,

$$[O^x_{(w')}] = \frac{K^{1/2}_{O_{(w')}} K_{O^x_{(w'')}} P^{1/2}_{O_2} [V^{\bullet\bullet}_{O(w')}]}{P^2_{(w')}}$$

If the oxygen flux is proportional to the concentration of species O^x, then the oxygen flux can be represented as equation (26).

$$J_{O_2} = \alpha\left(P'^{1/2}_{O_2} - P''^{1/2}_{O_2}\right) \tag{26}$$

where $\alpha = \beta_1 / L$; β_1 is the bulk-diffusion step constant determined experimentally and *L* is the membrane thickness.

Kim et al [44] derived an equation which accounts for the surface exchange kinetics for tubular perovskite membranes which was used to fit the oxygen permeation data for $SrCo_{0.8}Fe_{0.2}O_{3-\delta}$ and $Sm_{0.5}Sr_{0.5}CoO_{3-\delta}$.

$$J_{O_2} = \frac{2\pi r_1 r_2 w C_i k_{io}}{S(r_1 + r_2)} \left(\sqrt{\frac{P'_{O_2}}{P^0_{O_2}}} - \sqrt{\frac{P''_{O_2}}{P^0_{O_2}}} \right) \tag{27}$$

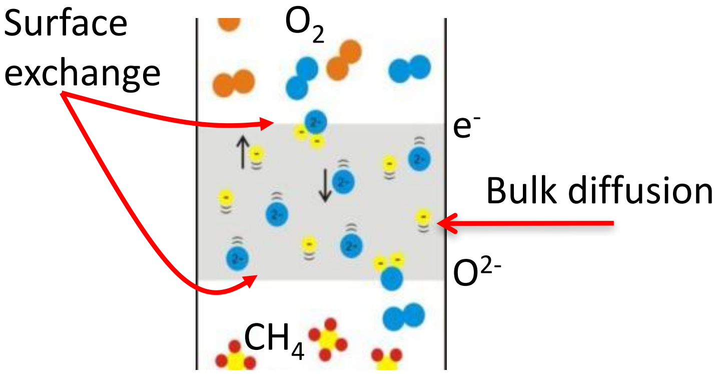

Figure 17 Surface exchange and bulk diffusion mechanism

2.3.5 Generalized transport equation:

Incorporating all mechanisms into a single explicit equation was demonstrated by many researchers [49-56] with the following assumptions.

i. The oxygen permeation rate across the membrane is governed by the flux of oxygen vacancies since the electronic conductivity in perovskite is much greater than its ionic conductivity.

ii. A steady-state electric field gradient is negligible due to fast movement of electron holes (electronic holes is assumed to dominate the electronic conductivity).

iii. Ideal gas behaviour is applied to the gas phase.

iv. The radial diffusion is neglected while the diffusion coefficient of oxygen vacancies D_v is assumed to be constant.

v. Surface-exchange reaction in the feed side is governed by equation (17) while the reverse of equation (17) applies to the permeate side, both with the rate constants k_f and k_r that are equal for both sides.

vi. Concentration of electron holes is considered constant at both sides of the membrane while the law of mass action is applied for other components.

$$J_{O_2} = \frac{(k_r / k_f)(1/P_{O_2}^{''0.5} - 1/P_{O_2}^{'0.5})}{(1/k_f P_{O_2}^{''0.5}) + (2L/D_v) + (1/k_r P_{O_2}^{'0.5})} \tag{28}$$

The above equation (28) is derived for specific disk-shaped membranes and has been shown to fit the oxygen flux for LSCFO in the temperature range 750^{o}C-950^{o}C and for 0.21-1.0atm oxygen partial pressure at the feed side. In the equation, each term in the denominator represents resistance in the feed, bulk membrane and permeates side respectively.

Xu et al [52] carried out similar analysis for disc membrane LCSF6428 and a correlation is developed for steady state oxygen permeation flux.

$$J_{O_2} = \frac{D_v k_r \left[(P_{O_2}^{'})^{0.5} - (P_{O_2}^{''})^{0.5} \right]}{2L(P_{O_2}^{''})^{0.5}(P_{O_2}^{'})^{0.5} + ((P_{O_2}^{'})^{0.5} + (P_{O_2}^{''})^{0.5})D_v} \tag{28}$$

Where D_v, k_f, k_r are functions of temperature and specific properties of the membrane and can be obtained by fitting experimental oxygen flux data as a function of temperature and oxygen partial pressure gradients.

The above equation can be rewritten in form as, $J_{O_2} = \dfrac{\Delta P_{O_2}}{R_t}$

Where $\Delta P_{O_2} = (k_r / k_f)(1/P_{O_2}^{''0.5} - 1/P_{O_2}^{'0.5})$ is oxygen pressure driving force across the membrane and $R_t = R_{ex}^{'} + R_{diff} + R_{ex}^{''}$ is the total resistance to permeation, where

$$R_{ex}^{'} = (1/k_r(P_{O_2}^{'})^{0.5})$$

$$R_{diff} = (2L/D_v)$$

$$R_{ex}^{''} = (1/k_f(P_{O_2}^{''})^{0.5})$$

If any one step is limiting then its resistance dominates the total partial pressure difference, so the permeation flux based on the single step can be given as follows

Bulk diffusion $\Rightarrow J_{diff} = \dfrac{\Delta P_{O_2}}{R_{diff}} = \dfrac{k_r D_v (1/P_{O_2}^{''0.5} - 1/P_{O_2}^{'0.5})}{2Lk_f}$

Surface exchange: oxygen-rich side $\Rightarrow J_{ex}^{'} = \dfrac{\Delta P_{O_2}}{R_{ex}^{'}} = k_r(P_{O_2}^{'0.5} / P_{O_2}^{''0.5} - 1)$

Surface exchange: oxygen-lean side $\Rightarrow J_{ex}^{''} = \dfrac{\Delta P_{O_2}}{R_{ex}^{''}} = k_r(1 - P_{O_2}^{''0.5} / P_{O_2}^{'0.5})$

The value of D_v , k_f , k_r can be obtained by the following expressions.

$$D_v = D_v^0 \exp\left(\frac{-E_D}{RT}\right)$$

$$k_r = k_r^0 \exp\left(\frac{-E_f}{RT}\right)$$

$$k_r = K_r^0 \exp\left(\frac{-E_r}{RT}\right)$$

Where E_r, E_D, E_f is the activation energies (kJ/mol) and k_r^0, D_v^0, k_f^0 are pre-exponential coefficients for reverse, bulk and forward reaction rate constants.

Tan and Li [50] derived the O$_2$ permeation flux equation(30) for tubular membrane accounting for bulk diffusion of oxygen vacancies in the membrane and the surface oxygen exchange kinetics on either side of the membrane by considering no mass transfer resistance between gas and the membrane surface.

$$J_{O_2} = \frac{k_r\left[(P'_{O_2})^{0.5} - (P''_{O_2})^{0.5}\right]}{(R_m / R_{in})(P''_{O_2})^{0.5} + (2t_e(P''_{O_2})^{0.5}(P'_{O_2})^{0.5} / D_v) + (R_m / R_o)(P'_{O_2})^{0.5}} \tag{30}$$

where, J_{O_2} is the oxygen permeation molar flow flux, mol/cm^2-s, $\Rightarrow R_m = \frac{R_o - R_{in}}{\ln\left(R_o / R_{in}\right)}$, R_m is the average radius of the tubular membrane, in which R_o and R_{in} is the outer and the inner radii of the tubular membrane in cm, t_e is the effective thickness of the membrane wall and for symmetric membrane it is given as $t_e = R_o - R_{in}$.

It can be seen that the total permeation resistance is composed of three parts:

i. The exchange reaction at the inner membrane surface (permeate side). $\Rightarrow R_1 = (P_{O_2}^{''})^{0.5} / k_r R_m / R_{in}$

ii. The bulk diffusion $\Rightarrow R_2 = 2t_e k_f / k_r (P_{O_2}^{''})^{0.5} (P_{O_2}^{'})^{0.5} / D_v$

iii. The exchange reaction at the outer membrane surface (feed side). $\Rightarrow R_3 = (P_{O_2}^{'})^{0.5} / k_r R_m / R_o$

The $P_{O_2}^{'}$ and $P_{O_2}^{''}$ are the partial pressure of oxygen at the feed side and the permeate side respectively. R_1, R_2, R_3 are the resistances to oxygen permeation as described above and these resistances has the units (atm$^{0.5}$cm^{2}sec/mol). D_v is the diffusion coefficient of oxygen vacancies in the membrane (cm^2/s); k_f (cm atm$^{-0.5}$s^{-1}) and k_r (mol cm^{-2}s^{-1}) are the forward and the reverse reaction rate constants for the surface exchange reaction shown in equation (31):

$$\frac{1}{2} O_2 + V_O^{\bullet\bullet} \xleftrightarrow{k_f / k_r} O_o^x + 2h^{\bullet} \tag{31}$$

The charged defects are defined using Kröger-Vink notation [15] where O_o^x represents lattice oxygen, $V_O^{\bullet\bullet}$ the oxygen vacancy and $h^{\bullet}$ the electron hole. Both, diffusion coefficient of the oxygen vacancy and the surface exchange reaction constants are function of temperature but independent of the oxygen partial pressures [57].

Tan et al [57] predicted these constants for LSCF6428 in analysis for oxyfuel combustion using membranes and are given in equations (32-34). In these equations, T is the local temperature in K.

$$D_v = 1.58\times10^{-2}\exp\left(\frac{-8852.5}{T}\right) \tag{32}$$

$$k_f = 5.90\times10^{6}\exp\left(\frac{-27291}{T}\right) \tag{33}$$

$$k_r = 2.07\times10^{4}\exp\left(\frac{-29023}{T}\right) \tag{34}$$

Wang et al [58] conducted oxygen permeation study in a tubular $Ba_{0.5}Sr_{0.5}Co_{0.8}Fe_{0.2}O_{3-\delta}$ oxygen permeable membrane. Oxygen permeation flux was measured at different partial pressure on both side of the membrane for different membrane temperatures in the range of 700 and 900 ^oC. The experimental setup consist of a tubular membrane of dia 4.96 mm, shell of dia 29 mm and length 17.68 mm. Air (O_2 and N_2) is used as feed at shell side with mass flow rate of 300 ml/min and He is used as sweep gas in tube side with mass flow rate of 60 ml/min for varying oxygen partial pressure in shell side from 0.09 atm to 1 atm and for temperature range between 700-900 ^oC. The results show that the oxygen permeation flux increases with increase of partial pressure of oxygen at shell side for a constant temperature. The increase of temperature also greatly affects the permeation flux along with the partial pressure of O_2 at the feed side. The analysis was done considering two mechanism of transport of oxygen, one is surface exchange current model and other is bulk diffusion given by equations (26) and (10) respectively.

Guillodo et al [59] conducted experimental analysis for oxygen permeation through dense $Bi_2V_{0.9}Cu_{0.1}O_{5.35}$ ceramic membranes. The oxygen permeation was decomposed in three steps: bulk diffusion, surface exchange between oxygen and oxygen vacancies at feed side and surface exchange between oxygen and oxygen vacancies at permeate side. The oxygen flux is modeled using Wagner theory [40] assuming that both surfaces of the membrane are in equilibrium with the imposed gas atmospheres. The oxygen permeation flux was correlated as equation (19).The experiments are done on three cells and out of which two cells are coated with porous gold layer. The amount of oxygen permeation flux was calculated by varying the pressure at the feed side between $10^2$and 10^5 Pa. The results show that permeation flux is proportional to the $\left(P_1^n - P_2^n\right)$ where the best fit value of n obtained to be 0.5. The maximum value of oxygen flux was 9.1×10^{-7} mol cm^{-1}min^{-1} for 923 K and 10^5 Pa.

Taheri et al [60] made a comparison for the permeation of oxygen flux through three membranes SCF, LSCF (6482) and LSCF (8264). For a given membrane, the oxygen flux was found to be a function of temperature and partial pressures. The permeation of oxygen was assumed to be dominant by bulk diffusion as given by equation (7).The temperature was assumed 1153 K and the membrane thickness was 0.84 mm. The partial pressure of oxygen at the feed side was varied between 0.1-1.0 bar and the air mass flow rate was 150 mL/min and the sweep gas (He) flow rate was 25 ml/min. The flux increased as LSCF (8264) <LSCF (6482) <SCF (82). The increase of flux was found to be proportional to the ratio of natural log of partial pressure of oxygen at feed to permeate sides and reaches a maximum value of 1.0×10^{-7} mol/cm^2.s for LSCF(8462), 1.7×10^{-7} mol/cm^2.s for LSCF(6482) and 9.2×10^{-7} mol/cm^2.s for SCF(82).

Xuan et al [61] carried out numerical modeling by integrating the chemical kinetics for autothermal reforming (ATR) of biogas. The performance and characteristics of biogas for hydrogen production was investigated for a two-dimensional model based on the integration of chemical kinetics with the computational fluid dynamics. The analysis was done for three physical models; one was the conventional ATR reformer and other two with hydrogen membrane reformer and oxygen membrane reformer. The results obtained from the numerical investigation were compared with the experimental data of autothermal reforming of methane and the results were in good agreement.

An experimental investigation of oxygen permeation through perovskite membrane under vacuum and elevated pressures was carried out by Zhu et al [62]. The analysis was done by taking BSCFO material and the dimensions were OD 2.38 mm and ID of 1.4 mm and length of 400 mm. The feed mass flow rate was varied from 100-200 ml/min and the pressure at the feed side ranged from of 1atm to 7 atm and the permeate side is kept at vacuum pressure of 100 Pa. The experiments are done at elevated temperatures of 825-925°C. The maximum permeation reported was 9.5 cm^3/cm^2-min at 925°C and 7 atm pressure at feed site for 200 ml/min mass flow rate of air at feed.

Tan et al [57] studied oxy-fuel combustion using a catalytic ceramic membrane reactor. In this experimental work, Tan et al used perovskite $La_{06}Sr_{0.4}Co_{0.2}Fe_{0.8}O_{3-\alpha}$ (LSCF6428) hollow fiber oxygen-permeable membranes, prepared by phase inversion/sintering technique, for combustion in a hollow fiber membrane reactor (HFMR). It was assumed that the furnace gives a symmetrical temperature profile. A second HFMR was prepared using platinum coated LSCF6428 hollow fiber membranes. The methane was fed into inner side, through the catalyst bed while the air supply was introduced concurrently into the shell side (outer diameter) of the hollow fibers. The total time was ten minutes. All experiments were performed at 1 atm on both the shell and inner sides. In modeling of the membrane reactor assumptions in the model equations are made such as, radial concentration gradients and the temperature changes due to reaction can be neglected. The modeling equations are a group of ordinary differential equations and are solved numerically using MATLAB. The results showed that as the methane feed flow rate increases, more oxygen is converted and the oxygen conversion eventually approaches 100%. Furthermore no products other than carbon dioxide were observed during the experiments. It was concluded that the granular LSCF6428 catalyst shows a high catalytic activity to methane combustion. At high methane feed flow rate, the experimental data were in better agreement with the simulated results using the faster reaction kinetics. The oxygen concentration in the product stream was found to increase as the temperature was increased indicating that the oxygen permeation rate is higher than the oxygen consumption rate due to the reactions. The conversion for both methane and oxygen was found to increase as the reaction rate increases. Both effect of increasing the temperature or decreasing the methane feed flow rate tend to increase methane conversion. It was shown that the model can adequately predict the trend of the experimental results both for the methane conversion and the oxygen permeation rate It was found that methane combustion in the HFMR is dependent on the rate of oxygen permeation through the membranes. The results showed that the oxygen permeation rate is increased due to platinum coating and, as a result, the methane conversion is increased. The coating decreased the outer surface exchange resistance to oxygen permeation leading to the improvement of oxygen permeation rate and hence methane conversion.

The performance of ITM reactors were studied in different configurations such gas single-tube, hollow-fibber membrane module, capillaries and monolithic multi-channels. Of all the configurations, the hollow-fiber module has highest surface area and is suggested for use in oxyfuel combustion applications [63]. Table 1 shows some of the researchers who carried out experiments on tubular membrane for oxygen permeation.

Table 1 Materials and operating conditions of previous experimental work done on tubular membrane for oxygen permeation

Membrane	Shape	Thickness (mm)	Temperature (°C)	P_1(atm)	P_2(atm)	J_{O2}	Ref.
$Ba_{0.5}Sr_{0.5}Co_{0.8}Fe_{0.2}O_{3-\delta}$	Tube	1.5	700-900	0.09-1	0.0093-0.1147	7.068×10^{-7}--2.31×10^{-6} (mol/m^2-s)	[58]
$Ba_{0.5}Sr_{0.5}Co_{0.8}Fe_{0.2}O_{3-\delta}$	Tube	0.22	850-950	0.21	0.01	1.406×10^{-6}--3.266×10^{-6} (mol/m^2-s)	[64]
$CaTi_{0.8}Fe_{0.2}O_{3-\delta}$	Tube	1	800-1000	0.21	0.0789	7.976×10^{-9}--2.18510^{-8} (mol/m^2-s)	[65]
$Bi_{1.5}Y_{0.3}Sm_{0.75}O_3$	Tube	1.2	850-875	0.21	0.05-0.15	4.4×10^{-7}--6.36×10^{-7} (mol/m^2-s)	[66]
$Bi_{1.5}Y_{0.3}Sm_{0.75}O_3$	Tube	1.225	870-930	0.005-0.5	0.014-0.071	2.364×10^{-8}--7.750×10^{-8} (mol/m^2-s)	[67]
$(ZrO_2)_{0.85}(CaO)_{0.15}$	Tube	1.67-2.75	1230	0.001-1	1×10^{-6}--1×10^{-4}	2.82×10^{-10}--8.42×10^{-10} (mol/m^2-s)	[68]
$La_{0.6}Sr_{0.4}Co_{0.2}Fe_{0.8}O_{3-\alpha}$	Tube	0.44	700-950	0.21	0.001	1.57×10^{-3} --5.49×10^{-3} (mol/m^2-s)	[62]
$La_{0.6}Sr_{0.4}Co_{0.2}Fe_{0.8}O_{3-\alpha}$	Tube	1	850-900	0.219	0.21	4×10^{-7}--1.050×10^{-7} (mol/m^2-s)	[69]
$Ba_{0.5}Sr_{0.5}Co_{0.8}Fe_{0.2}O_{3-\delta}$	Tube	0.2	700-1000	1	Not reported	1.10×10^{-2}--6.0×10^{-2} (mol/m^2-s)	[70]
$[(ZrO_2)_{0.9}(CeO_2)_{0.1}]_{0.9}(CaO)_{0.1}$	Tube	2	1127-1527	0.21	0.003-0.006	3.222×10^{-11}-1.938×10^{-9} (mol/m^2-s)	[47]
$[(ZrO_2)_{0.8}(CeO_2)_{0.2}]_{0.9}(CaO)_{0.1}$	Tube	2	1127-1527	0.21	0.003-0.006	1.361×10^{-10}--9.439×10^{-9} (mol/m^2-s)	[47]
$[(ZrO_2)_{0.7}(CeO_2)_{0.3}]_{0.9}(CaO)_{0.1}$	Tube	2	1127-1527	0.21	0.003-0.006	2.777×10^{-10}--1.562×10^{-8} (mol/m^2-s)	[47]
$[(ZrO_2)_{0.6}(CeO_2)_{0.4}]_{0.9}(CaO)_{0.1}$	Tube	2	1127-1527	0.21	0.003-0.006	6.308×10^{-10}--2.405×10^{-8} (mol/m^2-s)	[47]
$SrCo_{0.5}FeO_x$	Tube	0.25-1.0	850	0.21	Not reported	0.3-3.35 (cm^3/cm^2-min)	[71]
$La_{0.2}Sr_{0.8}Fe_{0.8}Co_{0.1}Cr_{0.2}O_{3-\delta}$	Tube	1,1.1	1000	0.21	0.00003	0.6-6.0 cm^3/cm^2-min)	[72]
$(LaCa)(CoFe)O_{3-\delta}$	Tube	0.4,0.8	800-950	0.21	0.005-0.009	0.1-10 (cm^3/cm^2-min)	[73]
$Ba_{0.5}Sr_{0.5}Co_{0.8}Fe_{0.2}O_{3-\delta}$	Tube	0.83	825-925	01-Jul	0.001	2.5-8.5 (cm^3/cm^2-min)	[74]
$La_{0.6}Sr_{0.4}Co_{0.2}Fe_{0.8}O_3$	Tube	0.6	800-900	0.21	0.142 -- 0.083	0.303-0.780 (ml/cm^2-min)	[75]

2.4 Numerical work in the area of membranes

Numerical simulations of membrane using finite-volume approach are very few. Mirella et al [76] carried out numerical and experimental investigation of mass transfer performance of Pd-Ag Membrane Modules for Hydrogen separation. In the analysis, impact of concentration polarisation and non-ideal flow on design of membrane separation units was evaluated by using Computational Fluid Dynamic. In the analysis, the source and sink terms are introduced on either side of the membrane boundary cell in order to account for the permeation of hydrogen in the numerical study developed by Coroneo et al [77]. The study covered different module configuration for H_2 and N_2

mixture and compared with the experimental results which were found to be in good agreement. The analysis extended to the use of baffles which permits the production of compartments inside the module, avoiding mixing and increase permeation driving force. The results show the separation performances of the module increases with the number of baffles. In all modules, studied the module with baffle resulted in maximum permeates of H_2.

Shigeo Goto [78] studied the effect of hydrogen permeation rate through composite palladium membrane for tubular configuration. A palladium film was coated on composite membrane tube. The analysis was done for increasing temperatures for two different modes. In the first mode, CP mode, H_2 was passed through the tube and pressure was reduced in shell side. Therefore, H_2 permeates first ceramic tube and then through the palladium film. In the second mode, PC mode, H_2 was passed from shell side and pressure inside the membrane tube was reduced and H_2 permeates first through palladium film then composite tube. The numerical models were based on the combined resistances of both palladium film and composite support. From the results it showed that with increase of temperature, permeation rate increases under CP mode.

A CFD modelling of inorganic membrane modules for gas mixture separation was carried out by M Coroneo et al [77]. First, they derived the permeation coefficient, based on the transport mechanisms for the gas molecules across the membrane. The basics of molecular diffusion, Knudsen diffusion and viscous (Poiseulle) flow, and used in the source term formulation in the continuity and species transport equations. Of all the mechanisms, the molecular diffusion was dominant on H_2 permeation at high pressures. The mole fraction and permeation rate of hydrogen increases with increase of working pressure and a good agreement with the experimental results was found.

Staudacher et al [79] conducted simulative analysis of mass transfer effects in gas and vapour permeation modules. The study relates the effect of concentration polarisation and flow distribution with spacers between two membrane surfaces. Calculations of permeation as a function of temperature, pressure and composition were done using finite-volume method. The use of baffles in the model which separates membrane into a number of compartments helped in velocity control of feed. The flow through the membrane was implemented as a sink in the basic transport equation for each finite cell. A user-defined function (UDF) was implemented for the transport from the membrane using a function for flux proportional to partial pressures. Similar to the work Staudacher et al [79], it was found from the results that the driving force obtained was due to concentration polarisation and the use of spacers which affects the performance of membrane.

The above literature shows a great potential of ITMs in optimizing the power generation systems and giving a breakthrough towards clean energy production. Using these ITMs many probable power cycles [29-35] were proposed and some of them [29-32] were implemented without integration as combustor. Currently, research has been focusing towards the ways of integrating the ITMs with combustion chamber [33-36]. The study of fluid dynamics and membrane behaviour with the combustion has not been studied yet in designing the combustion chamber integrated with ITMs.

Many researchers [37-61] have examined the performance of these membranes experimentally for oxygen separation. The experiments were done in both disk type and tubular membranes to study the permeation performance based on the geometrical and membrane characteristics. For Oxygen transport reactor, the feasible design at the initial stage is the concentric tubes with air in the outer side and sweep gas (inert) in the core side in order to sweep out the permeated oxygen. The effect of flow rates of sweep gas and air has been studied [58] and it shows increase of permeation with increase of sweep gas flow rates. It is tedious to do experiments each time to study the characteristics of such membrane. One of the alternatives is to use computational fluid dynamics to study the behaviour of these membranes.

If the permeate side is reacting, then the permeation performance will change due to reduced oxygen partial pressure. So, it is important to know the performance of these membranes when there is a reacting zone in order to integrate with power plant. Modeling the phenomenon of species transport from one side to the other numerically was studied [76-78] for Hydrogen separation through Pd-Ag membranes without reacting zone at permeates side. Zhang [73] and Smith [74] modeled the behaviour of ITMs for one dimensional model assuming that change of oxygen mole fraction on the surface of membrane and in the bulk is negligible. This assumption is not fully valid for natural gas combustion application since the mole fraction of oxygen will reduce from membrane surface to bulk as it will be consumed by the methane.

From the above discussion, it is evident that all of the numerical studies done are one dimensional and mostly for separation only. If we have the combustion at permeate side then it is important to know the combustion and permeation characteristics. So in order to study the behaviour of species in the whole domain the problem must be solved assuming axisymmetric velocity and thermal fluids.

CHAPTER 3

MODEL DEVELOPMENT

This chapter consists of three sections. The first section gives detailed information about formulating the permeation of oxygen through the Ion Transport Membrane. The second section explains the combustion chemistry and reaction mechanism. The last section of this chapter defines the numerical scheme and boundary conditions.

3.1 Membrane Permeation model

Dense perovskite membranes of type $Ba_{0.5}Sr_{0.5}Co_{0.8}Fe_{0.2}O_{3-\delta}$ is selected since the oxygen flux obtained is highest with it as reported in table 1 and it is good conductors of both types with electron carriers and oxygen ion and high permeation are reported through these membranes [58]. Mechanism of oxygen transport through these membranes is classified into two types: exchange reactions on the membrane surfaces and the ionic diffusion through bulk diffusion [80] and it is discussed earlier in chapter 2. These two mechanisms are interrelated by a characteristic thickness of membrane L_c which is related to the ratio of self-diffusivity of oxygen to surface exchange coefficient $\left(D_s/k_{io}\right)$ [45]. If the thickness of the membrane is greater than the characteristic thickness, then bulk transport dominate, if the thickness of the membrane is less than characteristic thickness then oxygen transport is equally limited by both surface exchange kinetics and the bulk diffusion.

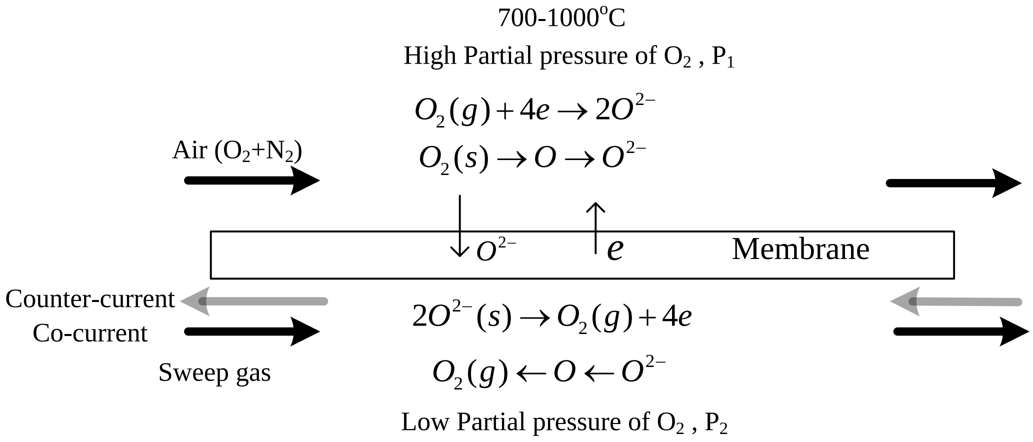

Figure 18 Mechanism of Oxygen transport through dense Ion transport membrane by considering Surface exchange mechanism

The mechanism of oxygen transport through the dense perovskite $Ba_{0.5}Sr_{0.5}Co_{0.8}Fe_{0.2}O_{3-\delta}$ membrane is shown in Fig. 18. At feed side oxygen molecules are absorbed on the membrane surface and converted in oxygen ions. These oxygen ions then migrate to permeate side through the bulk via the oxygen vacancies and then it gets recombine with the holes to form oxygen molecules. The oxygen permeation through these dense, mixed conduction membranes has been by the equation (35) for the case of steady-state, diffusion limited oxygen transport.

$$J_{O_2} = \frac{2\pi r_1 r_2 w C_i k_{io}}{S(r_1 + r_2)} \left(\sqrt{\frac{P_1}{P_0}} - \sqrt{\frac{P_2}{P_0}} \right) \tag{35}$$

Where r_1 and r_2 are the outer and the inner radius of the membrane tube respectively, w is the effective length of the tube, S is the effective area of the membrane tube, C_i is the density of oxygen ions, k_{io} is the surface exchange coefficient, P_1 is the partial pressure of oxygen at the feed side, P_2 is the partial pressure of oxygen at the permeate side and P_0 is 1 atm oxygen pressure. From above equation is valid if only the surface exchange limited to oxygen transport and the oxygen permeation flux J_{O_2} should be linearly proportional to the pressure term $(P_1/P_0)^{0.5}$-$(P_2/P_0)^{0.5}$.

The permeation of oxygen flux has been investigated experimentally under different pressure at feed side and temperatures for different material configurations. Many relations has been derived for oxygen permeation for such conditions as ionic diffusion as well as the surface exchange reactions on the membrane surface through the bulk material as mentioned in chapter 2.

3.1.1 Methodology:

For the computational modeling of the performance of the OTR membrane, the commercial code FLUENT 12.1.2 is used. The study focused on the effect of oxygen partial pressure across the membrane and the membrane temperature on the oxygen permeation flux. A CFD model has been developed to predict the performance of ITM membrane of the type $Ba_{0.5}Sr_{0.5}Co_{0.8}Fe_{0.2}O_{3-\delta}$ for oxygen separation. In general, separation of gas from a mixture through membrane can be modelled by considering two different phenomena, the fluid dynamic behaviour of the gas mixture in the membrane module and the transport of the species in the mixture across the membrane.

3.1.2 Governing Equations:

The numerical simulations are based on the CFD methodology developed by Coroneo et al. [76] which was developed in the realm of a finite-volume method. The velocity and the pressure fields of the gas mixture are obtained from the numerical solution of the mass, momentum and energy equations, while the species concentration distribution and the fluxes at the permeate and the feed side are obtained by the scalar convection-diffusion equation including source/sink term to account for the mass flow of the species across the membrane. The following equations for conservation of mass, momentum, energy and species for Newtonian fluids are considered:

$$\nabla.(\rho U)=S_i$$

$$\nabla.(\rho UU)=-\nabla p+\mu\nabla^2 U$$

$$(\rho C_p)U\cdot\nabla T=\nabla\cdot(k\nabla T)$$

$$\nabla\cdot(\rho UY_i)-\nabla\cdot(\rho D_{i,m}\nabla Y_i)=S_i$$

Where U is the velocity vector, ρ is the fluid density, p is the pressure, μ is the dynamic viscosity, S_i is the source or sink term. The S_i source/sink term is account for the mass flow of species across the membrane. At the membrane boundary cells the species (O_2) are allowed to disappear from one of the membrane sides (air side) through a sink term and to come out on the other (sweep side) through a source term. To apply this methodology the preliminary knowledge of the permeability characteristic of the membrane is required to formulate the source term. In the present work, the Oxygen transport membranes have been considered, which are permeable to oxygen only; therefore the source term takes into consideration only oxygen permeation.

$$S_i = \begin{cases} +\dfrac{J_{O_2} \cdot A_{cell} \cdot MW_{O_2}}{V_{cell}} & \text{at low partial pressure of } O_2 \\ -\dfrac{J_{O_2} \cdot A_{cell} \cdot MW_{O_2}}{V_{cell}} & \text{at high partial pressure of } O_2 \end{cases}$$

The term S_i is equivalent to zero unless $i=O_2$ and the computational cell is adjacent to the membrane. The diffusion coefficient was determined by specifying, the binary mass diffusion coefficient of the component i in the component j (other species). The corresponding diffusion coefficient in the mixture is computed as follows [81]:

$$D_{i,m} = \frac{1-X_i}{\sum_{j,j\neq i}\left(\dfrac{X_i}{D_{i,j}}\right)}$$

The binary mass diffusion coefficient, $D_{i,j}$, is calculated by Chapman-Enskog formula using the kinetic theory [82]. Special source terms are applied in the continuity and species transport equations in the computational cells adjacent to the membrane. It is worth observing that the driving force in the source term is evaluated adopting local values. Fluid density is calculated using ideal gas law. Density, viscosity, specific heat and thermal conductivity in the mixture according to the ideal gas mixing laws as follows [82] and same method of calculating these properties was also used by Nick and Alexander [83, 84] for modeling ITM model.

$$\rho_{mix} = (P_{op}+P)/\Re T\sum_{i}(m_i/M_i)$$

$$C_{p,\,mix} = \sum_{i} m_i C_{p,\,i}$$

$$\lambda_{mix} = \sum_{i}\left[X_i\lambda_i/\left(\sum_{i}X_j\varphi_{i,j}\right)\right]$$

$$\mu_{mix} = \sum_{i}\left[X_i\lambda_i/\left(\sum_{j}X_i\varphi_{i,j}\right)\right]$$

$$\varphi_{i,j} = \frac{\left[1+(\mu_i/\mu_j)^{1/2}(M_j/M_i)^{1/4}\right]^2}{\left[8(1+(M_i/M_j)\right]^{1/2}}$$

3.1.3 User Defined Function (UDF):

The equation developed by Kim et al [44] shown by equation (35) used by Haihui et al [58] to investigate the equation validity and found promising good. The O_2 permeation equations (35) involve the global partial pressures of O_2 of feed and permeate side. So, in order to convert global partial pressure terms to local partial pressure fitting of experimental data is done and develop an equation which accounts for local O_2 partial pressures.

$$J_{O2} = K_1 K_2 (T) \left(\sqrt{\frac{P_1}{P_0}} - \sqrt{\frac{P_2}{P_0}} \right)^{0.623} \tag{36}$$

$$K_1 = \frac{2\pi r_1 r_2 w}{S(r_1 + r_2)}$$

Where K_1 is a geometric constant and K_2 is a constant which depends on temperature.

Permeation of oxygen across the membrane is modelled using a series of user-defined functions that are written in VC++ and compiled and hooked in FLUENT 12.1.2 software. The issue of hydraulic jump across the membrane was resolved by patching the cells from the upper and lower zones with two different values of initial partial pressures of species. The source and sink terms in the UDF will be calculated by using the relation given below [58].

$$S_i = \frac{A_{cell}}{V_{cell}} \frac{2\pi r_1 r_2 w C_i k_{io}}{S(r_1 + r_2)} \left(\sqrt{\frac{P_1}{P_0}} - \sqrt{\frac{P_2}{P_0}} \right)$$

$$S_i = \frac{A_{cell}}{V_{cell}} \frac{2\pi r_1 r_2 w C_i k_{io}}{S(r_1 + r_2)} \left(\left(\frac{X_1 P}{P_0} \right)^{0.5} - \left(\frac{X_2 P}{P_0} \right)^{0.5} \right)$$

$$S_i = \frac{A_{cell}}{V_{cell}} K_1 K_2 \left(\left(\frac{X_1 P}{P_0} \right)^{0.5} - \left(\frac{X_2 P}{P_0} \right)^{0.5} \right)^{0.623}$$

The three different Macros used in UDF are ‘Define Initialize’, ‘Define Source’ and ‘Define Adjust’ as defined in FLUENT software. These macros link the cell index across the membrane which allows the addition and subtraction of the source term in continuity and species transport equation. Additionally, the UDF updates the solver data with the new parameter at the membrane wall for every iteration. The partial pressure given in the oxygen flux equation is calculated as concentration Y_i (% wt.) and the following flowchart (Figure 19) is applied for solving the O_2 permeation flux. The mass fraction, Y_i, will be converted into mole fraction and then applied in calculating the source term.

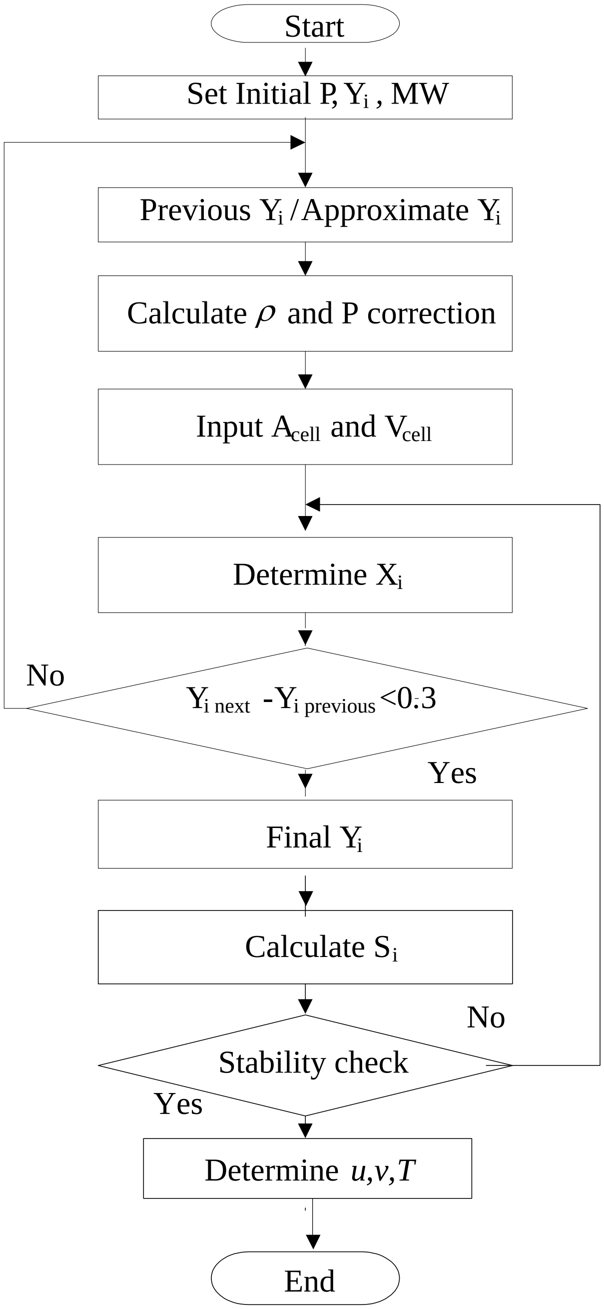

Figure 19 Solution strategy for oxygen transport though the membrane.

3.2 Combustion Mechanism

The kinetic mechanisms used to model hydrocarbon combustion are generally composed of a large number of elementary reactions to describe a single comprehensive overall reaction in which the initial fuel and oxidizer combine to form the final products. The rates in which reactions proceed are primarily dictated by collisions of two molecules that may have the capability to react. Therefore, the most common elementary reactions used in mechanism construction are bimolecular in which two species collide and react to form two new species. To illustrate, consider an arbitrary bimolecular second order reaction

$$\mathrm{A+B \rightarrow C+D}$$

The rate at which such reaction proceeds is proportional to the concentration of the reactant species,

$$\frac{\mathrm{d[A]}}{\mathrm{dt}}=\mathrm{-k[A][B]}$$

where the notation [A],[B] denotes the molar concentration of species A and B. The rate constant k is a function of temperature T and is the parameter used to describe each elementary reaction composing the entire kinetic mechanism [85,86,87]. A reaction will only take place, however, if the colliding molecules possess an adequate amount of energy called the activation energy E_a. the kinetic theory shows that the fraction of all collisions that possess energy greater than E_a is given by the Boltzmann factor $\exp\left(-E_a/RT\right)$

Determination of reaction rates also requires that the frequency of molecular collisions be taken into account in the form of a pre-exponential factor A. The rate constant k is then typically expressed in a modified Arrhenius form as

$$k=AT^{\beta}\exp\left(\frac{-E_a}{RT}\right)$$

Where A, β are parameters determined experimentally and R is the universal gas constant. The exponent β becomes particularly important in systems where temperatures vary widely.

The most common combustion processes encountered in engineering field are those which convert a hydrocarbon fuel into carbon dioxide and water. These combustion reactions are usually exothermic in nature.

3.2.1 Reaction Mechanism for methane combustion:

The Single step kinetic reaction mechanism for combustion of methane also follows the same mechanism as shown below.

$$CH_4+2O_2\xrightarrow{k}2H_2O+CO_2$$

$$k=AT^{\beta}\exp\left(\frac{-E_a}{RT}\right)$$

$$\frac{d\left[CH_4\right]}{dt}=-k\left[CH_4\right]^{n_{CH_4}}\left[O_2\right]^{n_{O_2}}$$

$$\frac{d\left[O_2\right]}{dt} = -2k\left[CH_4\right]^{n_{CH4}}\left[O_2\right]^{n_{O_2}}$$

$$\frac{d\left[CO_2\right]}{dt} = k\left[CH_4\right]^{n_{CH4}}\left[O_2\right]^{n_{O_2}}$$

$$\frac{d\left[H_2O\right]}{dt} = 2k\left[CH_4\right]^{n_{CH4}}\left[O_2\right]^{n_{O2}}$$

$$n_{CH_4}=0.2,\ n_{O_2}=1.3,\quad n_{CO_2}=0,\ n_{H_2O}=0$$

$$A=2.119\times10^{11},\ E_a = 2.027\times10^{8}\ \text{J/kg-mol},\ \beta=0$$

Now using both membrane permeation model and combustion together will be a challenging part in order to model ITM reactor.

The oxygen transport reactor considered for study is of cylindrical shape in which a mixture of CH_4 and CO_2 are injected from one side and the oxygen permeates through the ITM walls of the reactor. The study focuses on the effect of the sweep gas mixture (CO_2 and CH_4) on the oxygen permeation process through the ITM membrane for the two cases of co-current and counter-current flow regimes and validation of the computational model against the available experimental data. The ITM membrane has a tubular shape similar to that used in the experimental work by Wang et al. [58] and a schematic of the membrane is shown in Figure 20. The membrane comprised of a highly dense perovskite BSCFO with an effective surface area 12.56 cm^2 while the area used for model validation is of 2.531 cm^2. The experimental conditions were maintained at steady state with laminar flow on both sides. The outcome of this study represents the first step in designing ion transport reactors since it provides information about the size and geometry of the combustion region (based on the oxygen content of the mixture) for different mass fraction of CH_4 and CO_2 of the sweep gas.

After studying the cold combustion (mixing) the reaction mechanism is activated to study the temperature and combustion characteristics of the ITM reactor. The axisymmetric model of ITM reactor is shown in figure 21.

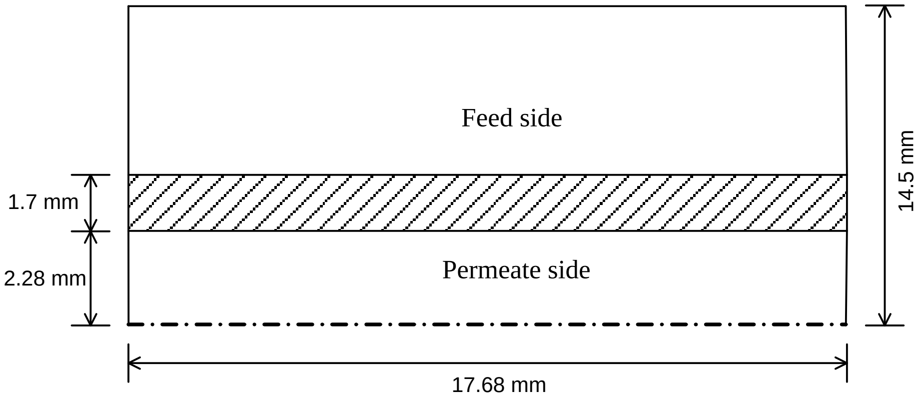

Figure 20 Axi-symmetric geometrical view for Wang et al [58]

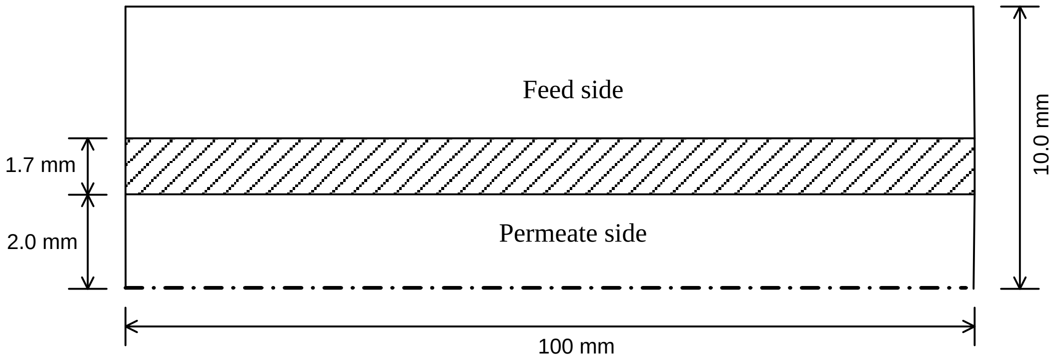

Figure 21 Domain for oxyfuel Ion transport membrane reactor

3.3 Numerical Scheme and Boundary conditions

In these simulations, the properties of the gas mixture at inlet of both inner and outer regions were first assumed the same as those considered in the experimental work of Wang et al. [58]. The discretization of the governing equations is done using a segregated solver in which each governing equation is solved separately. The Semi-Implicit Method for Pressure-Linked Equations (SIMPLE) formulation was used as a part of pressure-velocity coupling algorithm [88]. The convergence criteria for the continuity and momentum parameters were set to 10^{-6} and species and energy equation were set to 10^{-9} to allow sufficient iterations for complete convergence at all grid points. The gas density is calculated using the ideal gas law and the gas viscosity, specific heat and thermal conductivity are calculated as a mass fraction-weighted average of all species. The specific heat of each species is calculated using a piecewise polynomial fit of temperature [81] and tabulated in table 2.To obtain a stable solution, under-relaxation factors of 0.3 and 0.7 were used for pressures and velocities at all nodal points in the solution domain. The pressure staggered scheme (PRESTO) was used for pressure and the second-order upwind discretization scheme was used for momentum, species and energy equation [88]. To enhance the convergence of the numerical solution, the Aggressive Advanced Multigrid (AMG) scheme was used. The AMG cycle type for the coupled equations involving pressure, momentum, energy and species were set to fixed 'F-cycle' as a recursive process [81]. To avoid irregular convergence patterns 'Biconjugate Gradient Stabilized Method' (BCGSTAB) was employed. Properties of species used in single step combustion reaction are tabulated in table 3.

Table 2 Coefficients of polynomial functions* belonging to temperature-dependent thermal properties of species, taken from the material property database given by Fluent Inc. [81]

		a_0	a_1	a_2	a_3	a_4
CH_4	C_p	$4.03585 \cdot 10^{2a}$	9.05734	$-1.44200 \cdot 10^{-2}$	$1.58052 \cdot 10^{-5}$	$-6.34305 \cdot 10^{-9}$
		$8.72467 \cdot 10^{2b}$	5.30547	$-2.00829 \cdot 10^{-3}$	$3.51665 \cdot 10^{-7}$	$-2.33391 \cdot 10^{-11}$
	λ	$3\cdot32000 \cdot 10^{-2}$	0	0	0	0
	μ	$1.08700 \cdot 10^{-5}$	0	0	0	0
CO_2	C_p	$4\cdot29929 \cdot 10^{2}$	1.87447	$-1.96649 \cdot 10^{-3}$	$1.29725 \cdot 10^{-6}$	$-3.99996 \cdot 10^{-10}$
		$8.41377 \cdot 10^{2}$	$5.93239 \cdot 10^{-1}$	$-2.41517 \cdot 10^{-4}$	$4.52273 \cdot 10^{-8}$	$-3.15313 \cdot 10^{-12}$
	λ	$1.45000 \cdot 10^{-2}$	0	0	0	0
	μ	$1.37000 \cdot 10^{-5}$	0	0	0	0
H_2O	C_p	$1\cdot56308 \cdot 10^{3}$	1.60376	$-2.93278 \cdot 10^{-3}$	$3.21610 \cdot 10^{-6}$	$-1.15683 \cdot 10^{-9}$
		$1\cdot23323 \cdot 10^{3}$	1.41052	$-4.02914 \cdot 10^{-4}$	$5.54277 \cdot 10^{-8}$	$-2.94982 \cdot 10^{-12}$
	λ	$-7\cdot96800 \cdot 10^{-3}$	$6.88133 \cdot 10^{-5}$	$4.49046 \cdot 10^{-8}$	$-9.09994 \cdot 10^{-12}$	$6.17331 \cdot 10^{-16}$
	μ	$-4\cdot41894 \cdot 10^{-6}$	$4.68764 \cdot 10^{-8}$	$-5.38943 \cdot 10^{-12}$	$3.20286 \cdot 10^{-16}$	$4\cdot91918 \cdot 10^{-22}$
O_2	C_p	$8.34827 \cdot 10^{2}$	$2.92958 \cdot 10^{-1}$	$-1.49564 \cdot 10^{-4}$	$3.41389 \cdot 10^{-7}$	$-2.27836 \cdot 10^{-10}$
		$9.60752 \cdot 10^{2}$	$1.59413 \cdot 10^{-1}$	$-3.27089 \cdot 10^{-5}$	$4.61277 \cdot 10^{-9}$	$-2.95283 \cdot 10^{-13}$
	λ	$3.92175 \cdot 10^{-3}$	$8.08121 \cdot 10^{-5}$	$-1.35409 \cdot 10^{-8}$	$2.22044 \cdot 10^{-12}$	$-1.41614 \cdot 10^{-16}$
	μ	$7.87943 \cdot 10^{-6}$	$4.92495 \cdot 10^{-8}$	$-9.85155 \cdot 10^{-12}$	$1.52741 \cdot 10^{-15}$	$-9.42567 \cdot 10^{-20}$
N_2	C_p	$9.79043 \cdot 10^{2}$	$4.17964 \cdot 10^{-1}$	$-1.17628 \cdot 10^{-3}$	$1.67439 \cdot 10^{-6}$	$-7\cdot25630 \cdot 10^{-10}$
		$8.68623 \cdot 10^{2}$	$4.41630 \cdot 10^{-1}$	$-1.68723 \cdot 10^{-4}$	$2.99679 \cdot 10^{-8}$	$-2\cdot00439 \cdot 10^{-12}$
	λ	$4.73711 \cdot 10^{-3}$	$7.27194 \cdot 10^{-5}$	$-1.12202 \cdot 10^{-8}$	$1.45490 \cdot 10^{-12}$	$-7.87173 \cdot 10^{-17}$
	μ	$7.47331 \cdot 10^{-6}$	$4.08369 \cdot 10^{-8}$	$-8.24463 \cdot 10^{-12}$	$1.30563 \cdot 10^{-15}$	$-8.17794 \cdot 10^{-20}$

*Polynomial functions are defined as $\psi(T) = a_0+a_1T^1+a_2T^2+a_3T^3+a_4T^4$; [a]valid for temperature interval 300-1000 K; [b]valid for temperature interval 1000-5000 K.

Table 3 Properties of reactant and product species.

Species	**M[a] [Kg/mol]**	**H[a] [J/Kmol}**	**LHV[a][J/Kmol]**
CH_4	16.04303	-7.48952×10^7	-8.023×10^8
CO_2	44.00995	-3.93532×10^8	-
H_2O	18.01534	-2.41838×10^8	-
O_2	31.9988	-	-

[a] taken from the material property database given by Fluent Inc. [81]

CHAPTER 4

NUMERICAL STUDY

The control volume approach is used to discretize the governing equations using FLUENT^{TM} 12.1.2 code [81]. All variables are computed at each grid point except the velocities, which are determined midway between the grid points. A staggered grid arrangement is used in the present study, which links the pressure through the continuity equation and is known as SIMPLE algorithm [88].

The permeation of oxygen through the membranes and combustion is solved as a two dimensional axisymmetric problem using the double-precision solver. In addition to the scaled residuals, the temperature, mass fraction of CO_2 and H_2O (in case of combustion) at the outlet of the fuel zone is monitored using surface monitors to ensure convergence. Second order upwind schemes are used for discretization of momentum and energy equations.

4.1 Grid Independence

A numerical mesh generator GAMBIT is used to create the geometry and mesh the domain using hexahedral elements. A fine mesh is created to capture the large gradients normal to the flow direction. Three different grids for ITM reactor model of figure 21 with 10000, 12500 and 15000 are created to examine the grid independence. Figure 22 compares the mass fraction of O_2 along the axis obtained using the three grids by considering CH_4 at the fuel inlet without combustion and shows a good agreement between the mass fraction values. Figure 23 shows the mass fraction of oxygen through the membrane for the above mentioned grids with combustion and it can be seen that for all the three grids the O_2 mass fractions are in good agreement. Figure 24 shows the temperature variation for the same three different grids and found in very good agreement. From the above analysis, it can be concluded that the solution is grid independent for the selected grids.

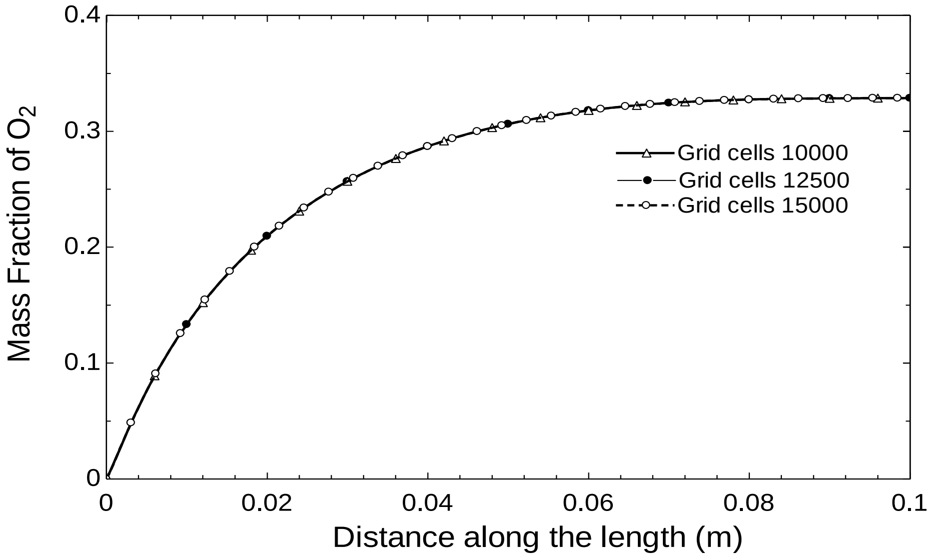

Figure 22 Mass Fraction of O_2 with three different grids without combustion

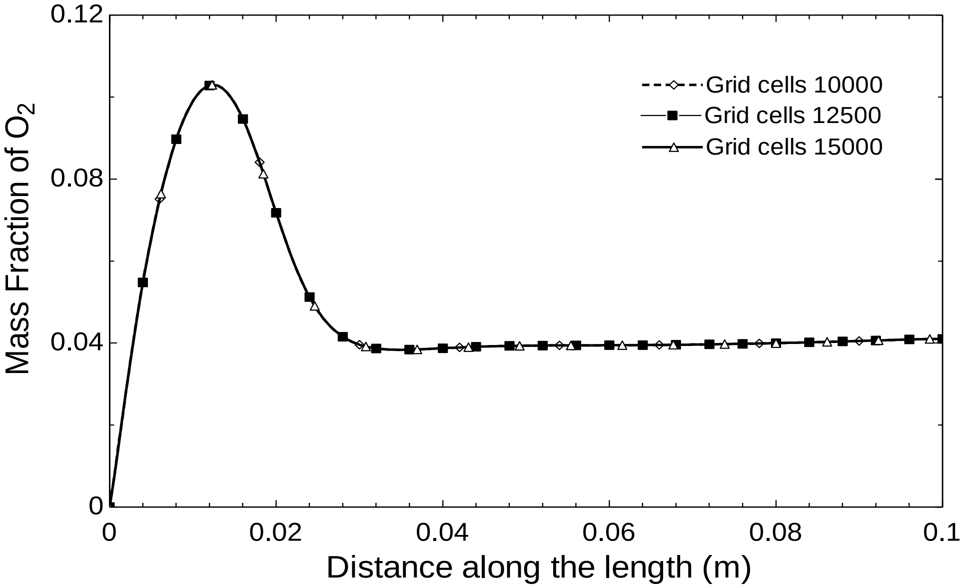

Figure 23 Mass Fraction of O_2 for three different grids with combustion

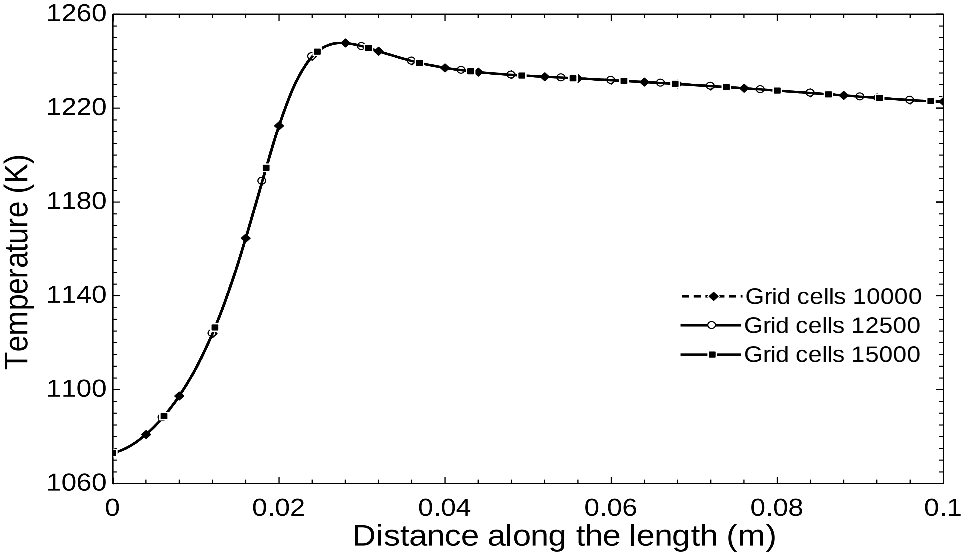

Figure 24 Temperature variation along the axis for three different grids

4.2 Validation

In order to verify the accuracy of the computational model, the performance of the ion transport reactor with the dimensions given in Figure 20 was predicted and compared with the experimental data of Wang et al. [58]. In this problem, the oxygen permeation flux through the membrane (BSCFO type) is investigated for different partial pressures and temperature. The air in the feed side is considered as a mixture of only O_2 and N_2 and the O_2 partial pressure is changed by changing the mole fraction. The air flow rate is 300 ml/min and Helium was used as sweeping gas in the inner region with a flow rate of 60 ml/min. The simulations are carried out for three temperatures and for oxygen partial pressures ranging from 0.09 atm to 1.0 atm. In all simulations, the pressure within the reactor is assumed atmospheric. Figure 25 shows the variation of O_2 permation flux and O_2 partial pressure at the reactor outlet for different values of O_2 partial pressure at inlet of the outer region considering operation at three different temperatures. The figure shows a significant increase in the O_2 permation flux with the increase of oxygen partial pressure in the feed side. The figure also shows a considerable increase in the oxygen flux at higher temperatures. A simple comparison between the model prediction and the measured values of O_2 permation flux shows a good accuracy especially at high oxygen partial pressue in the feed side. The largest deviation was about 15% occurring at 900^{o}C and 0.19 atm. This deviation may be attributed to experimental uncertaninties at high temperatures. The outlet partial pressure of O_2 at permeate side is also predicted and compared with the experimental results and shown above in Figure 26. The comparison with experimental measurements shows a good agreement over all the partial pressure range (P_1) with maximum deviation of the same order (≈ 15%) occurring at the high temperature of 900°C and P_1=0.19 atm.

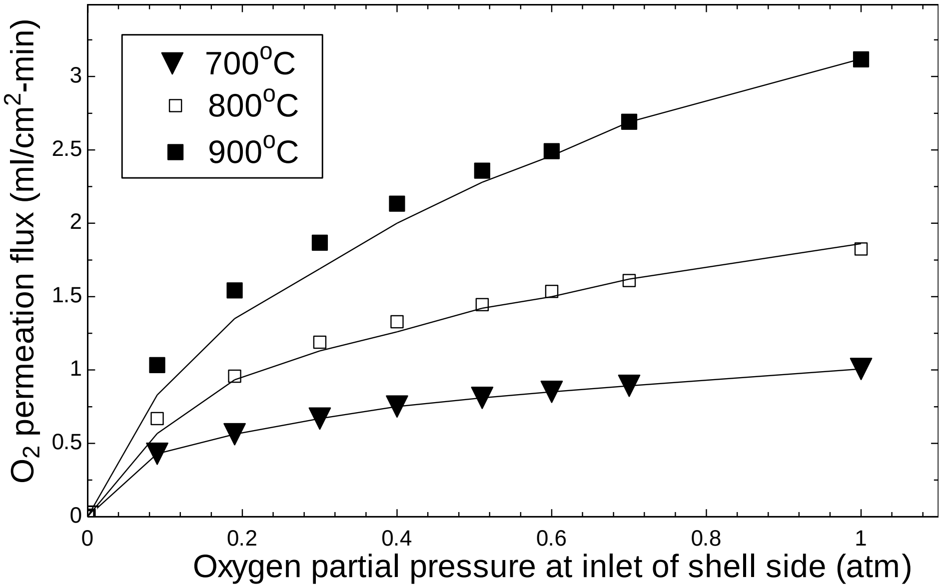

Figure 25 Variation of O_2 permeation flux with oxygen partial pressure at inlet of shell side, (■ □ ▼), experimental data; (——), present numerical results

Figure 27 shows the variation of the O_2 permeation flux over the reactor length at different operating temperatures and different inlet partial pressures (P_1). It is clear from the figure that the O_2 permeation rate is high in the vicinity of the reactor entrance and decreases downstream. This is attributed to the reduction in O_2 partial pressure difference across the membrane towards the exit section. As the temperature of membrane increases, the activation energy of the surface exchange increases resulting in higher permeation rates.

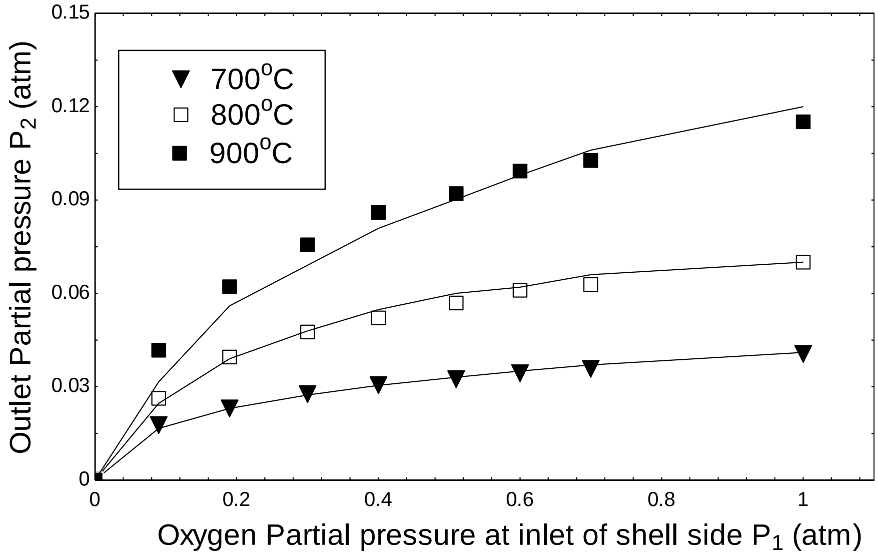

Figure 26 Variation of O_2 permeation flux and O_2 outlet partial pressure with O_2 partial pressure in the outer region. (■ □ ▼), experimental data; (——), present numerical results

Similarly, the permeation rate increases with the O_2 partial pressure on the feed side. Figure 28 shows the variation in O_2 concentration at the permeate side under different conditions of partial pressure values (P_1). The figure indicates that the permeation rate increases as P_1 increases. The figure also shows a maximum concentration of 0.21 in the case of P_1= 0.09 atm, this increases to around 0.94 as the pressure P_1 reaches 1.0 atm.

The O_2 mass fraction shown in figure 28 is related with mole fraction which is nothing but partial pressure since the reactor is working under atmospheric conditions. From this, it can be clearly seen that with increase of partial pressure at feed side then partial pressure difference across the membrane is increased leading higher O_2 permeation flux. Thus, it is advantageous to work at high O_2 partial pressure at feed side but the objective of this work is to separate O_2 from air. In that the O_2 concentration is fixed to 21% by volume. Hence for the separation of O_2 with these membranes having sweep gas mixture (CH_4 and CO_2) partial pressure of O_2 is fixed to 0.21 atm. The effect of difference of partial pressure across the membrane can be seen in figure 29. It is evident that higher the difference of partial pressure more the O_2 permeated and it is experimentally validated as shown. So in order to increases the difference in partial pressure one method is to create vacuum at permeate side and other method is to reduces the incoming O_2 by reforming or combustion.

The above comparisons give enough confidence in the computational model for investigating the effect of using the fuel mixture (CH_4 and CO_2) as sweeping gas on the performance of the ITM reactor.

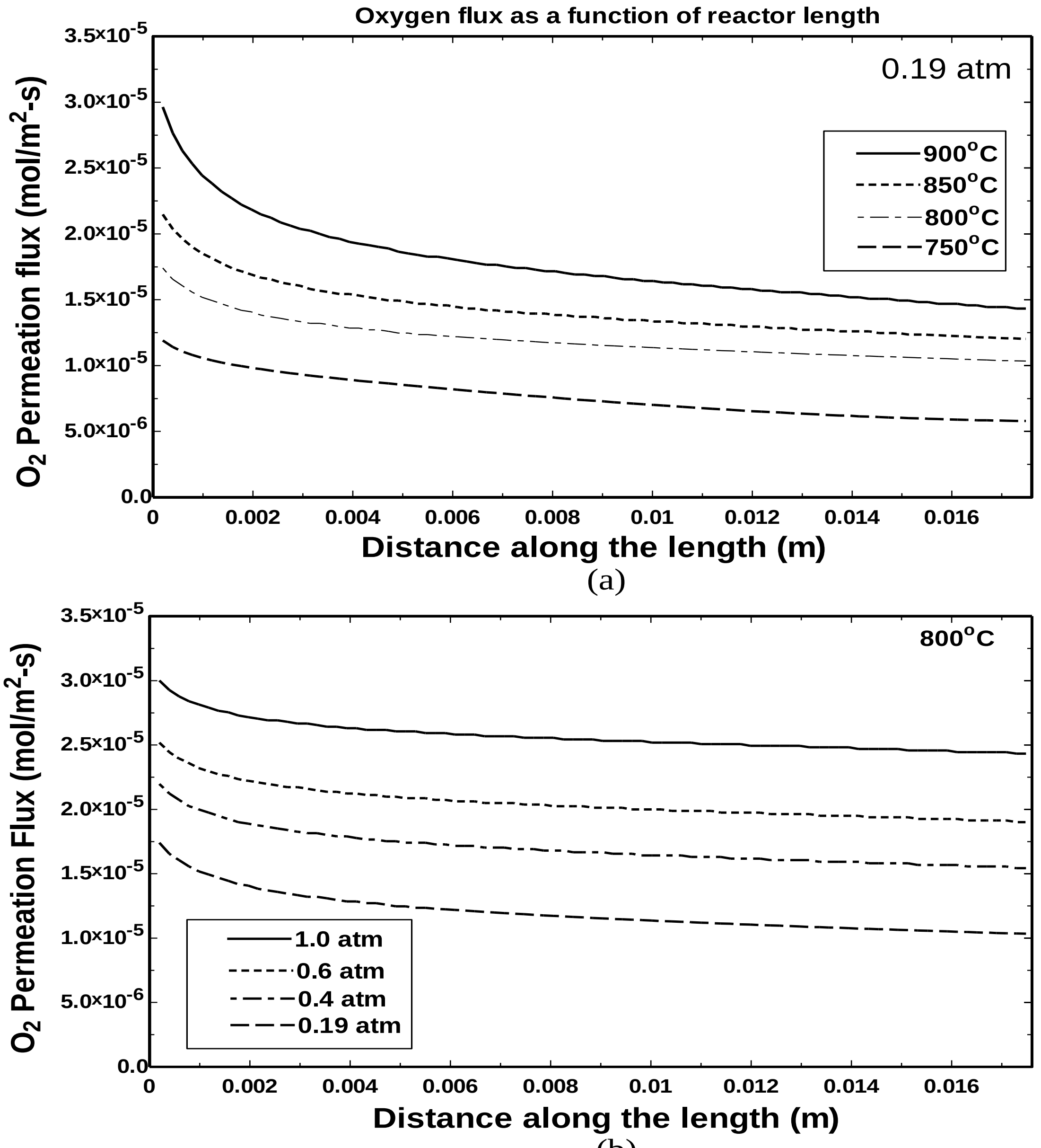

(a)

(b)

Figure 27 Variation of the O_2 permeation flux over the reactor length for a) different operating temperatures, and b) different inlet partial pressures (P_1)

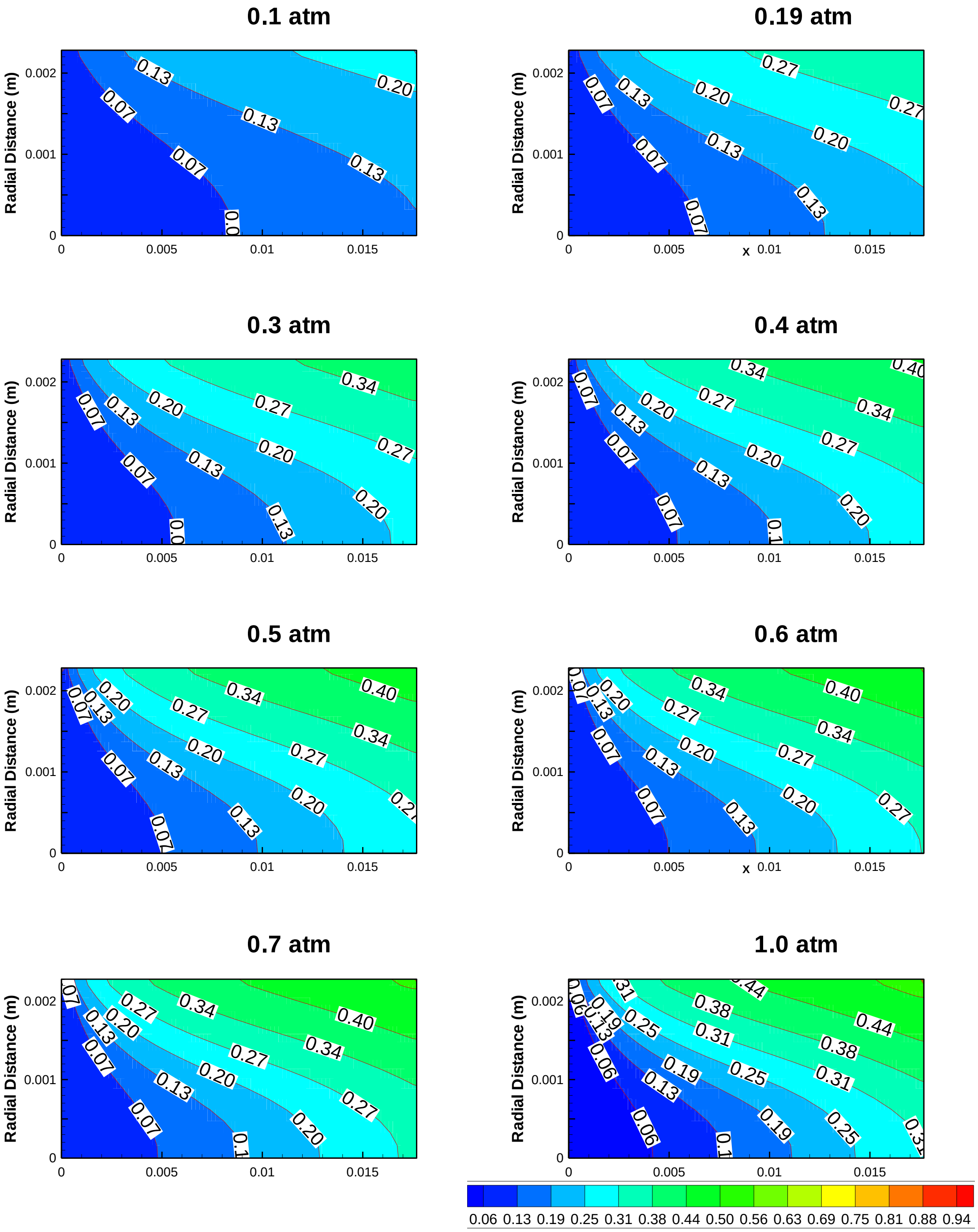
0.1 atm

0.19 atm

0.3 atm

0.4 atm

0.5 atm

0.6 atm

0.7 atm

1.0 atm

Figure 28 Variation of O_2 mass fraction within the reactor for different values of P_1 at the operating temperature of 800^0C

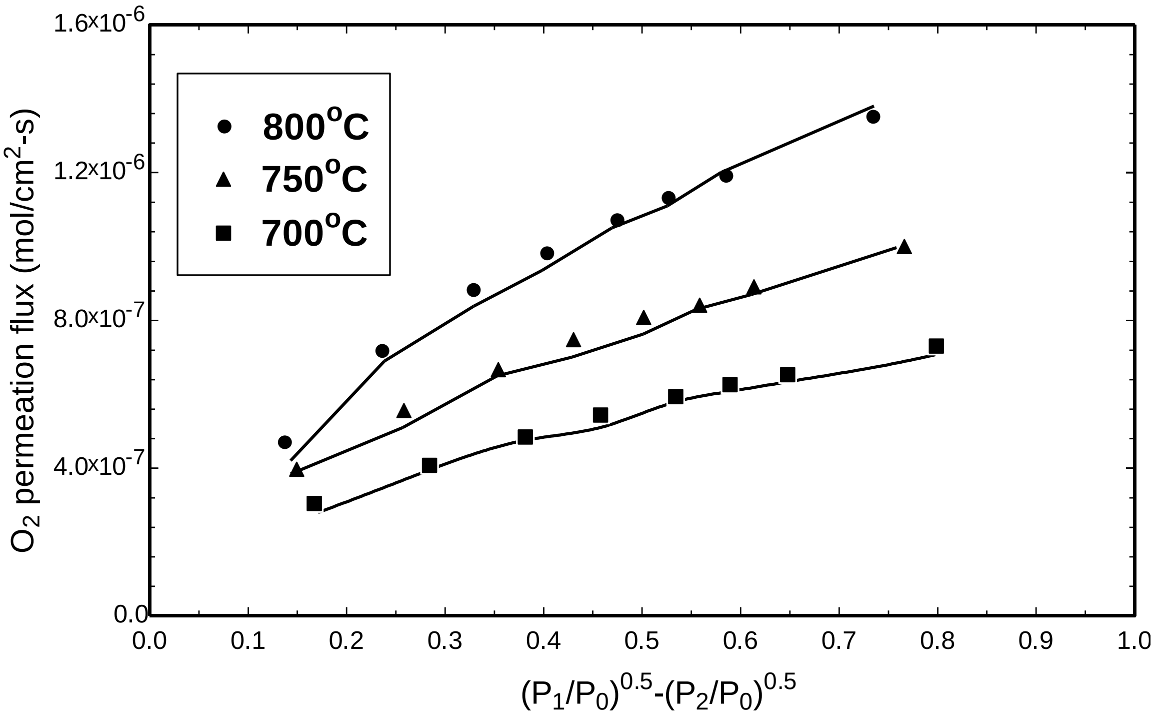

Figure 29 Oxygen permeation flux against $(P_1/P_0)^{0.5}$-$(P_2/P_0)^{0.5}$ at different temperatures

(● ▲ ■) shows the experimental data and (——) shows the numerical results.

In order to validate combustion model, the Norton and Vlachos micro burner geometry [89] is selected as shown in figure 30. The micro-burner consists of two parallel, infinitely wide plates of length of 1 cm. The distance between the two plates is 0.6 mm and the thickness of the wall is taken as 0.2 mm. The case is modeled as 2-D symmetric about the centre line as the gravity effects are neglected. The wall top is given a boundary condition of no convective heat transfer. The sides of the wall are insulated with no heat flux boundary condition. At the inlet, mass flow inlet boundary condition is applied and at the outlet a known pressure is specified. At the interface between the wall and the fluid, no-slip boundary condition and no-species flux normal to the wall surface are employed. The parameters used are V_0 = 0.5 m/s, thermal conductivity of wall = 7.5 W/m/K, h = 0 $W/m^2/K$. Premixed, stoichiometric methane/air mixtures are fed to a micro-burner. A finite-difference method is used to discretize the 2-D continuity, momentum, energy and species conservation equations in the fluid and the 2-D energy equation in the wall. Steady-steady simulations are performed. Figure 31 shows the centre line temperature profile for premixed air/methane combustion for micro-burner. It is evident that the temperature profile obtained by Norton and Vlachos [89] is in good agreement with the present calculation. With this combustion results validation we get enough confidence to perform the combustion in ITM reactor with O_2 separation.

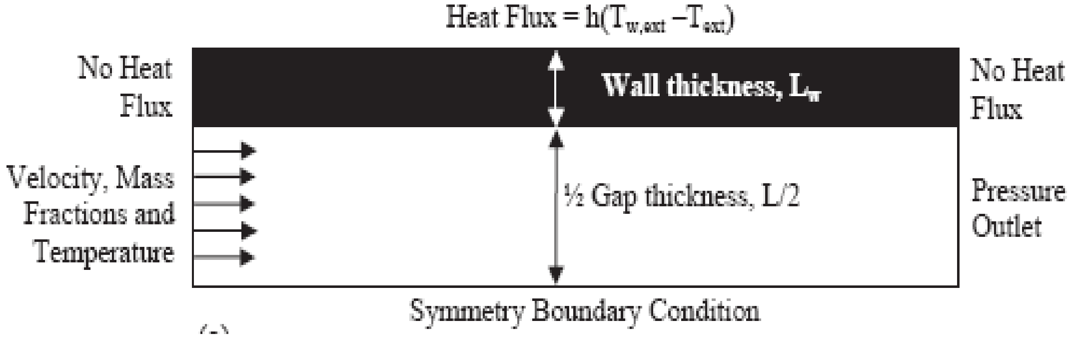

Figure 30 Schematic of computational domain along with a description of some of the boundary conditions used in the model by Norton and Vlachos [89]

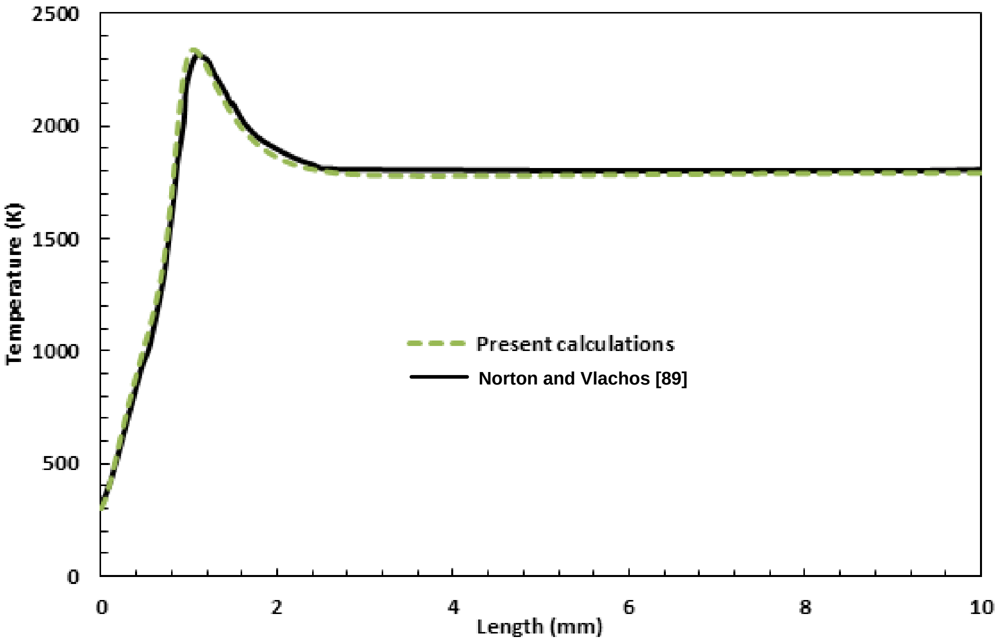

Figure 31 Centre line temperature profile for premixed combustion of air/methane mixture

CHAPTER 5

RESULTS AND DISCUSSION

This chapter consists of two sections. In the first section, the oxygen transport reactor is simulated on cold basis and the effect of O_2 permeation flux on sweep gas mixture variation is studied and in the second section, the combustion characteristics of methane within the reactor is presented and the effect of reducing environment on O_2 permeation flux is discussed. The results presented in each section pertain to the objectives discussed in the first chapter.

5.1 Cold Combustion (Mixing)

In this work, the performance of an ion transport reactor utilizing ITM-BSCFO membrane [$Ba_{0.5}Sr_{0.5}Co_{0.8}Fe_{0.2}O_{3-\delta}$] with the dimensions given in Figure 21 was investigated. The reactor operates with air at the feed side and a mixture of CH_4 and CO_2 (as sweep gas) at the permeate side. The study focuses on the effect of pressures and temperatures at the feed side on the composition of the gas mixture at the permeate side when operating at 1 atm. Air is assume to contain only N_2 (77% by mass) and O_2 (23%) in all cases.

Figures 32 and 33 present the contours of ratio of mass fraction of oxygen to methane ratio within the domain of the reactor for the co-current and counter-current regimes, respectively. This ratio is important to characterize the region in which combustion can take place. In both regimes, the ratio of oxygen to methane increases for decreasing percentage of CH_4 at inlet of the sweep side. As a result, the combustible region increases with the decrease of the CO_2 to CH_4 ratio. The influence of the sweep ratio (percentage of CO_2/CH_4 by mass) on the oxygen methane mixture composition for the co-current regime is shown in Figure 32. In order to control the oxygen to methane ratio within the reactor and to determine the regions of combustible mixture, the sweep ratio varies from 0% to 98%. The inlet region shows a rich mixture having a fuel to oxygen ratio outside the flammability region. This is attributed to the low oxygen flux at inlet of the reactor. The size of this region diminishes as the sweep ratio increases. The mixture starts to fall within the flammability limits at approximately $x/L = 0.05$. The stoichiometric mixture (ratio of O_2/CH_4 by mass equal to 4.0) appears only for CO_2/CH_4 ratio of 0.98/0.02. For this ratio, a large region around the stoichiometric value that lies within the flammability limits (regions having the ratio of O_2/CH_4 between 1.4 and 8.4) appeared.

The influence of the sweep ratio on the oxygen methane mixture composition for the counter-current regime is presented in Figure 33 where the percentage of CO_2 changes from 0% to 98%. Regions having O_2/CH_4 mixture within the flammability limits are shown at high sweep ratios in Figure 33. The figure indicates that changing the sweep ratio influences the boundaries of the flammability limits significantly. For example, for zero sweep ratio the region of flammability limits is formed only in the entrance region $[0 < X/L < 0.05]$. As the sweep ratio increases, the size of this region increases and the region out of flammability limits diminishes. As well, at low sweep ratios, the mixture is shown to be lean and does not reach stoichiometric composition. As the sweep ratio reaches 0.94/.06, the mixture is found to include a combustible region around the stoichiometric ratio. As the sweep ratio reaches 0.98/.02, the mixture becomes mostly lean mixture. A comparison between Figures 32 and 33 shows that the counter flow regime exhibits better mixing of fuel and oxygen. In addition, the counter flow regime results in more homogeneous difference in O_2 partial pressures across the membrane and, therefore, provides more uniform oxygen flux along the reactor wall. Figures 34 and 35 present the distribution of mass fractions of O_2, CH_4 and CO_2 along the reactor axis for different sweep ratios for the co-current and counter-current flow regimes, respectively. The figures indicate that the mixture is rich at low sweep ratios and reaches stoichiometric at higher values.

The variation of O_2/CH_4 ratio in the mixture along the reactor length is presented in Figures 36 for the two cases of co-current and counter-current flow regimes. The results indicate that the sweep ratio has a significant effect on the magnitude and distribution of the O_2/CH_4 mixture along the reactor. In the counter flow regime, the maximum ratio of O_2/CH_4 attained along the reactor is higher than that in the co-current case for all sweep ratios. On the other hand, a uniform distribution of the O_2/CH_4 ratio occurs over a larger distance along the reactor in the co-current regime for almost all values of the sweep ratio. Figure 37 presents the regions within the reactor that falls within the recommended flammability limits (O_2/CH_4 ratio between 4.1 and 4.8) for three sweep ratios (15.67, 24.0, 49.0) considering the two cases of co-current and counter-current regimes. These recommended flammability limits correspond to stoichiometric oxygen to methane ratio up to 10 to 30% excess oxygen. The three considered sweep ratios are the ones that guarantee mixtures within the flammability limits. However, as shown in the figure only the mixture having sweep ratio of around 24 for the co-current flow and around 15.67 for the counter-current flow lie within the recommended mixture composition. Other sweep ratios show either rich or lean mixtures. The figure also confirms that the counter-current flow requires less sweep ratio for achieving the recommended O_2/CH_4 ratio because of the higher O_2 permeation flux. It should be noted here that achieving a nearly uniform mixture composition along the membrane leads to nearly homogeneous reaction rates that are likely to result in achieving constant temperature along the membrane. This is essential for avoiding any thermal stresses along the membrane surface and achieving membrane stability.

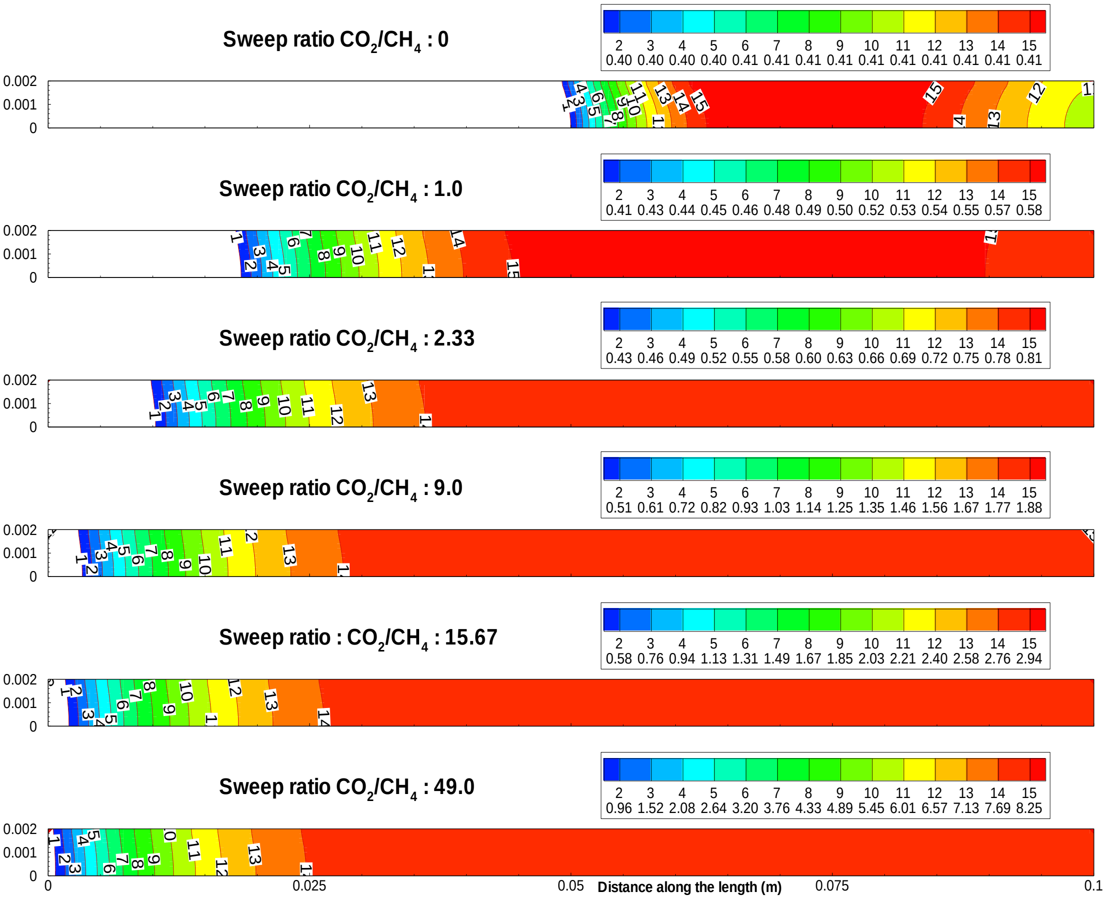

Figure 32 Oxygen to methane mass fraction ratio for different inlet conditions of sweep ratio (CO_2/ CH_4) for co-current configuration

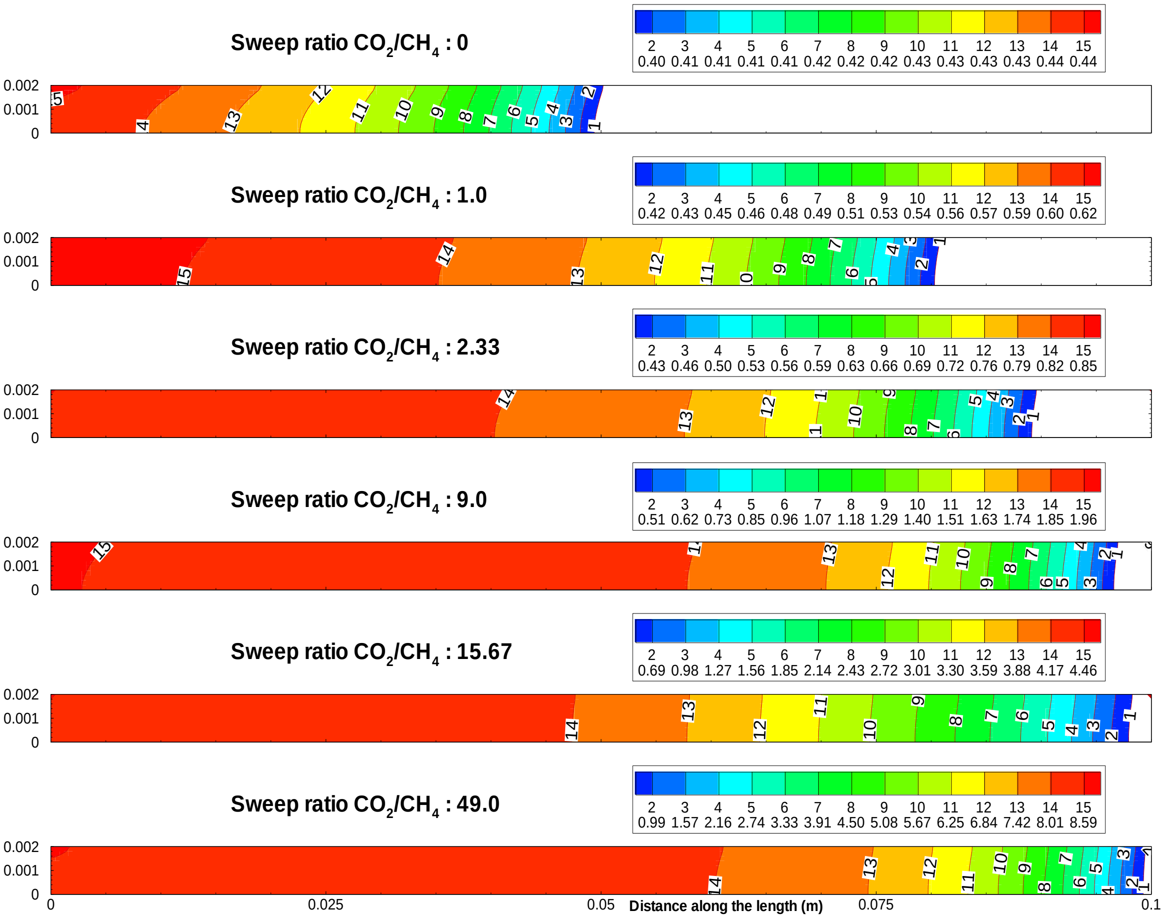

Figure 33 Oxygen to methane mass fraction ratio for different inlet conditions of sweep ratio (CO_2/ CH_4) for counter-current regime

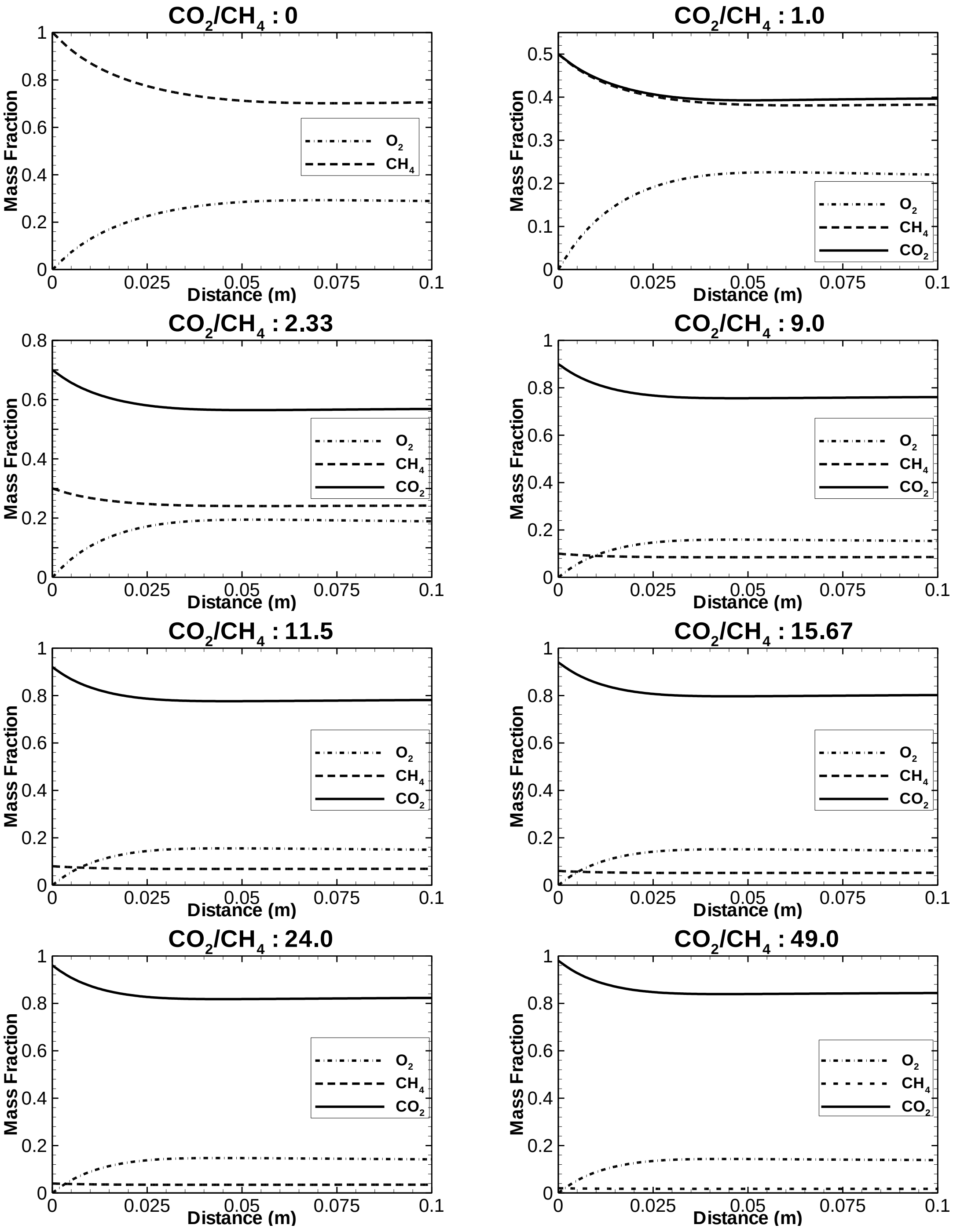

Figure 34 Mass fraction of species for different sweep ratios (CO_2/ CH_4) at inlet for co-current regime

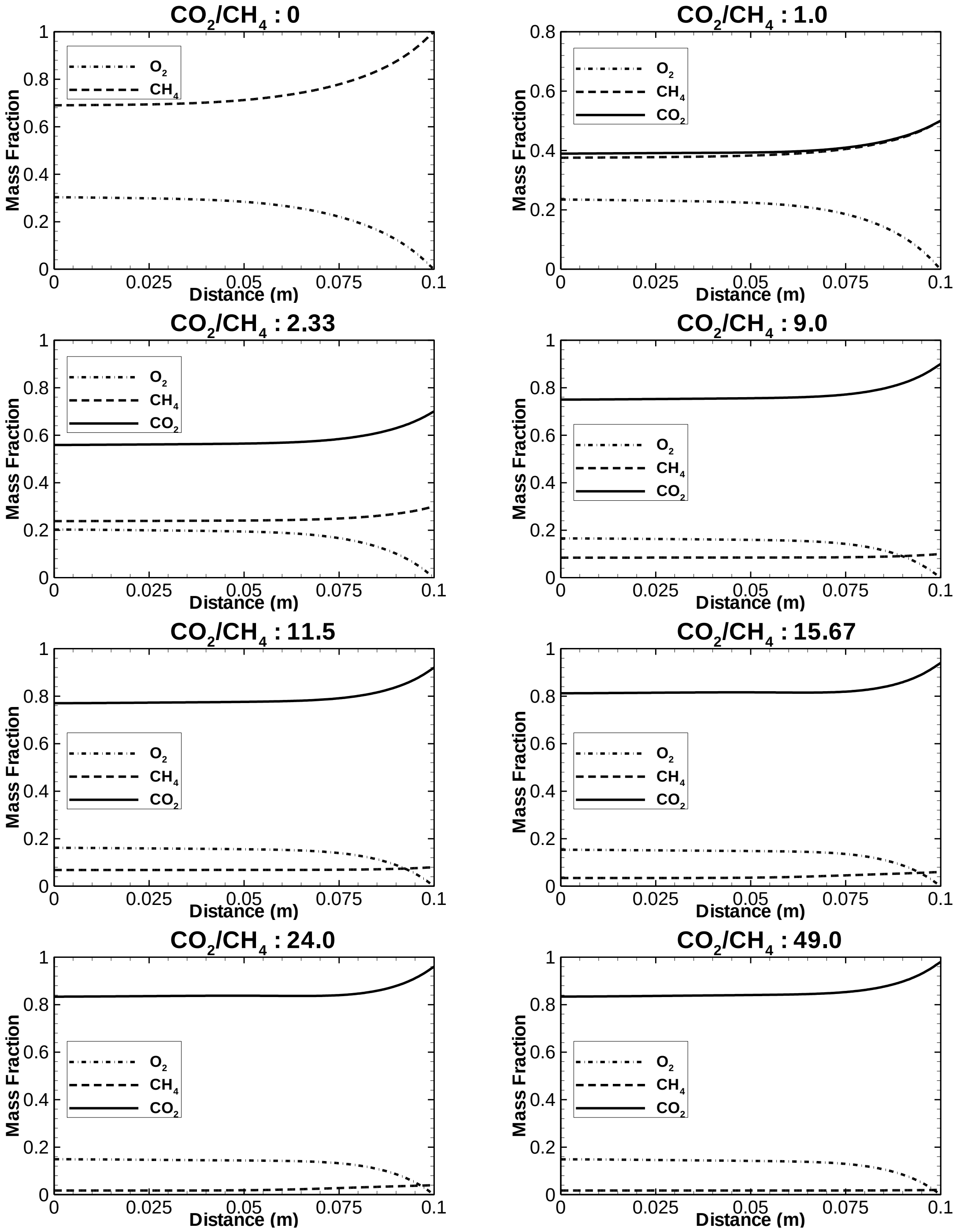

Figure 35 Mass fraction of species for different sweep ratios (CO_2/ CH_4) at inlet for counter-current regime

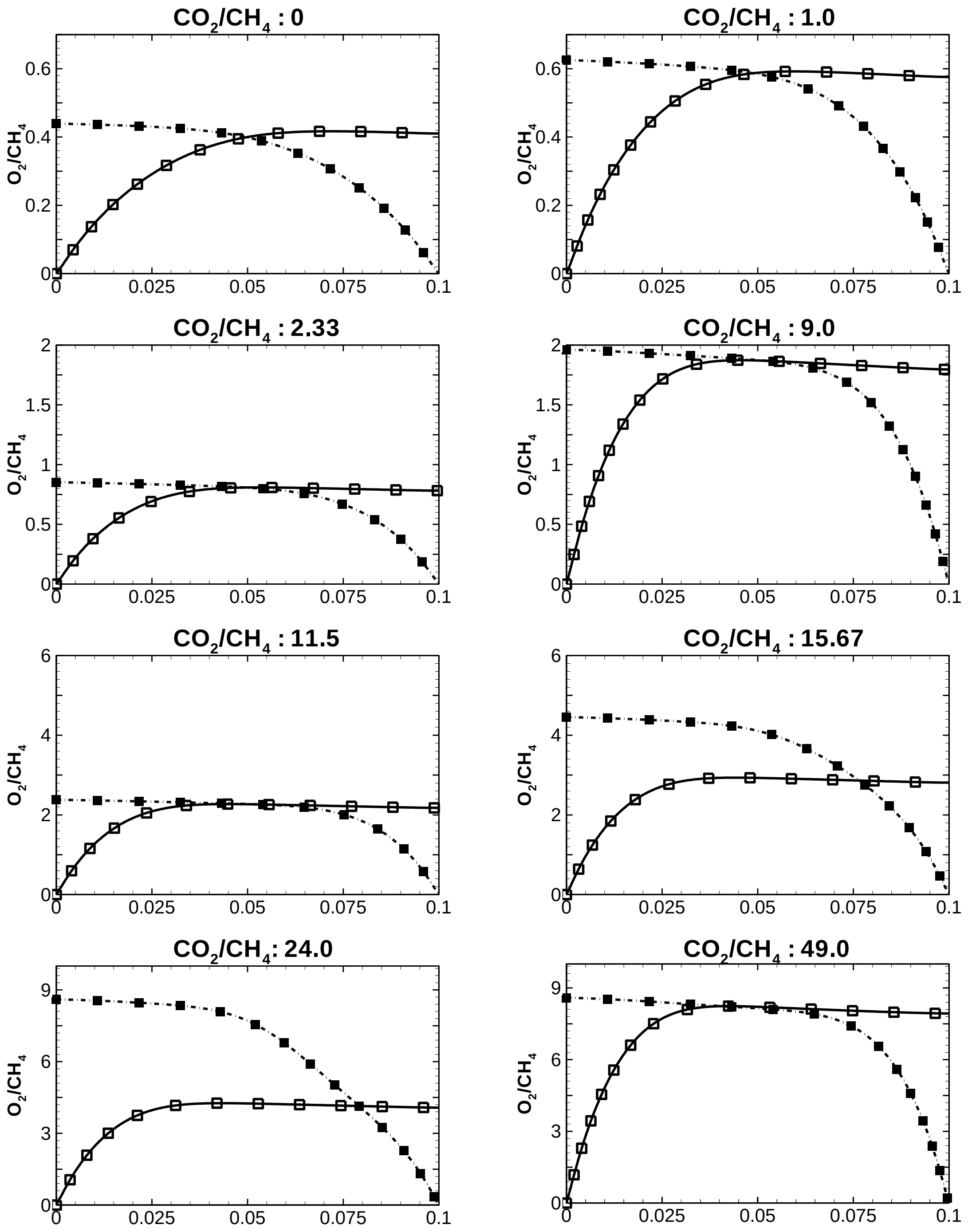

Figure 36 Ratio of O_2/CH_4 for different sweep ratios (CO_2/CH_4)

(□□□) co-current regime and (■■■) counter-current regime

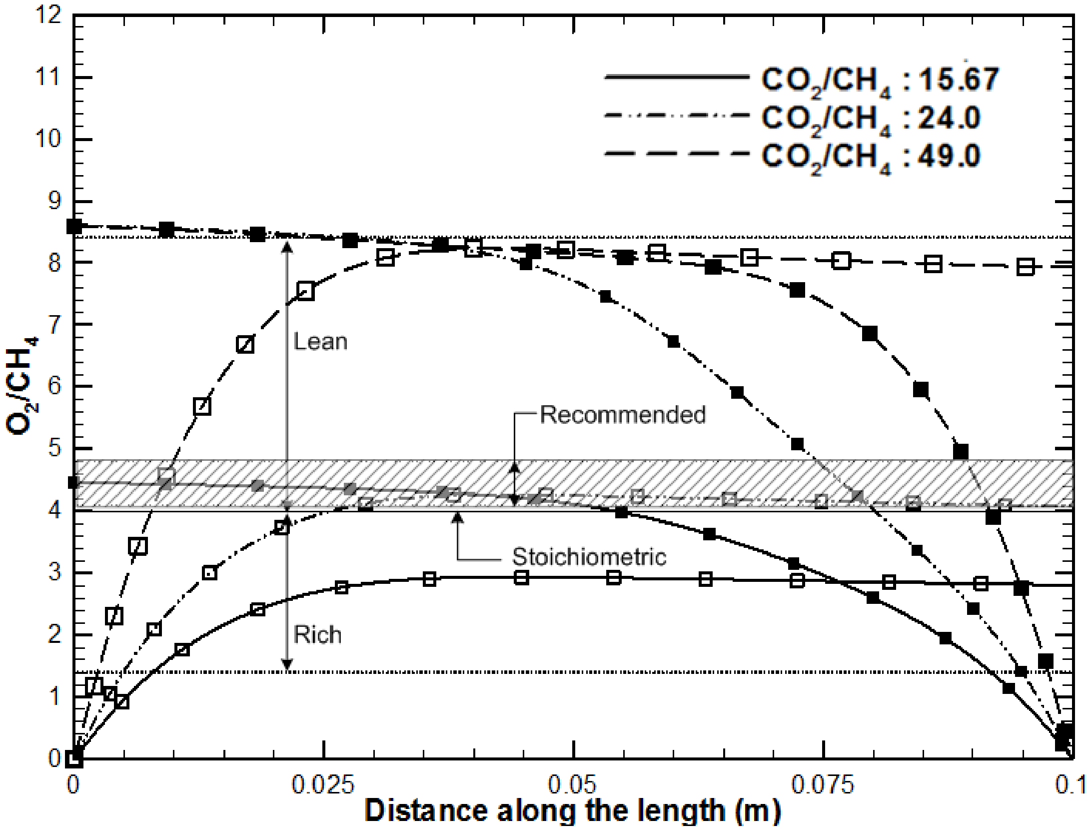

Figure 37 Variation of O_2/CH_4 along the reactor axis for different sweep ratios

(CO_2/CH_4);

(□○△) co-current regime and (■●▲) counter-current regime

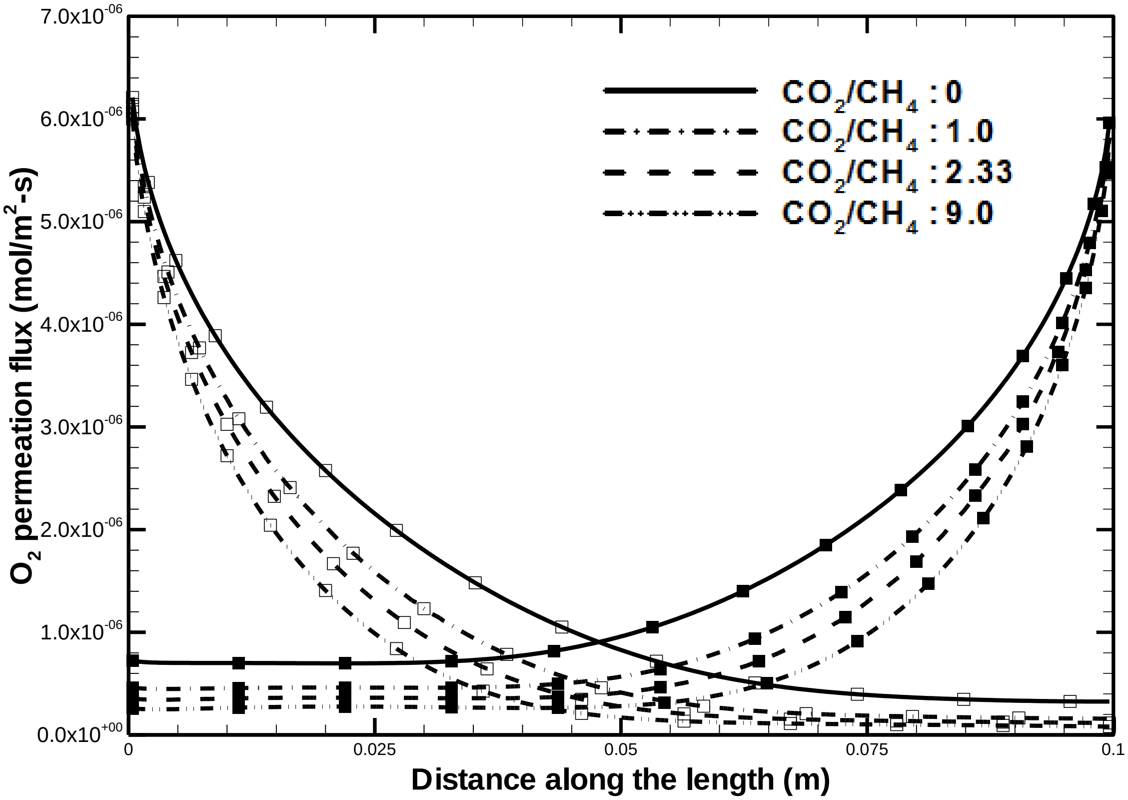

Figure 38 Variation of the oxygen permeation flux along the membrane surface for different sweep ratios (CO_2/CH_4), (○ △ □ ◇) co-current regime and (● ▲ ■ ◆) counter-current regime

The variation of the oxygen permeation flux along the membrane surface for the co-current and counter-current regimes are plotted in Figure 38 for different compositions of the sweep gas. The figure indicates that the O_2 permeation rate decreases along the length and reaches 5.97×10^{-06} (mol/m^2/s) at exit for 100% CH_4 at the inlet for counter-current flow as compared to 3.26×10^{-07} (mol/m^2/s) at exit for co-current. In general, the oxygen flux through the membrane surface in the counter-current regime has higher values as compared with the co-current case. In both regimes, the total O_2 permeation rate decreases with the increase of CO_2 in the sweep gas mixture and the same phenomenon was reported by [90] and [41]. In another study by [91], the decrease of O_2 permeation due to the increase of CO_2 in the sweep gas was attributed to the formation of carbonates on the membrane surface which reduces oxygen permeation at high temperature. Figure 39 shows a comparison between the total O_2 permeation rate in the co-current and counter-current regimes. The obtained results indicate that the total O_2 permeation rate is always higher in the counter-current regime for all sweep gas compositions. As the percentage of CH_4 in the sweep gas changes from 100% to 10%, the counter-current regime results in permeation rates that are 6.62% to 12.75% higher than those of the co-current regime. Manccini and Mitsos [83,84] have developed a block box model for modelling an ITM reactor and got similar results which show that the counter-current regime is more viable than the co-current.

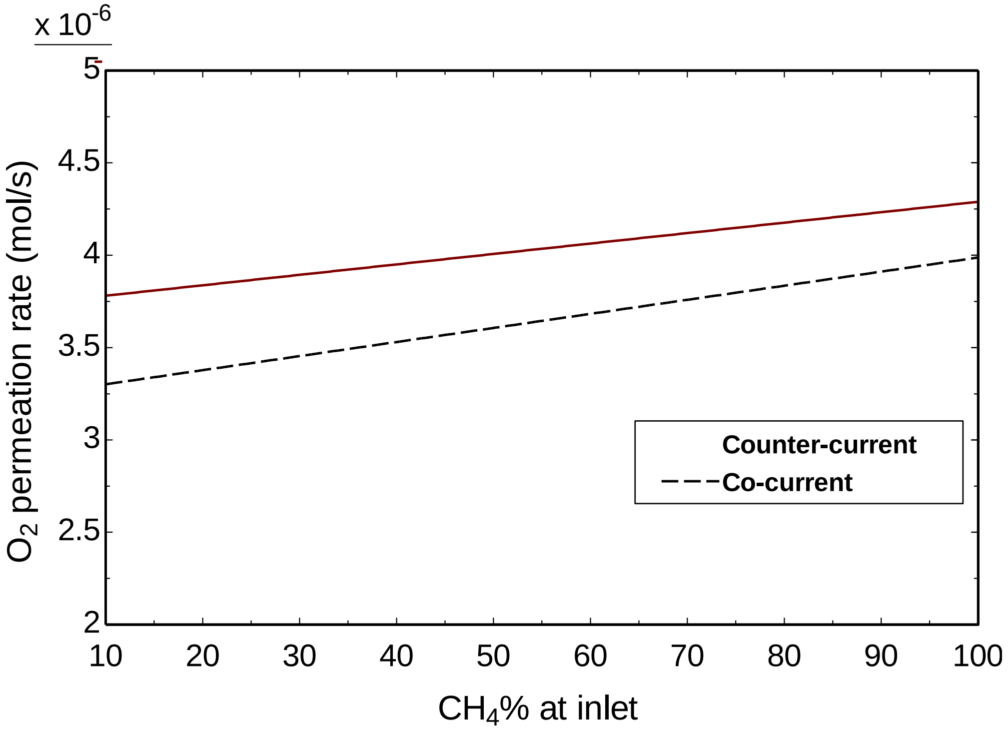

Figure 39 Variation of total oxygen permeation rate with percentage of CH4 in the sweep mixture

5.2 Combustion in ITM Reactor

Ion Transport Membranes made in monolith honeycomb reactor can play an important role in combustion chamber for gas turbines used in power generation where methane is the main reactant [92]. This honeycomb reactor contains hundereds of parallel tubes of ITMs that are of the order of 2-4 mm in diameter. The oxygen that comes from the ITM reacts with methane and combustion take place. In this section, the investigation has been extended to include from mixing of CH_4 and CO_2 with O_2 to create combustion with single-step chemistry. At present the model can be assumed as a single ITM tube of monolith honeycomb reactor as shown in Figure 40, the wall of the reactor is assumed to be adiabatic [58,92] to ensure similarity with the experimental model for permeation done by Wang et al[58]. Bouyancy and the heat flux by radiation are neglected because of the small diameter of ITM reactor that leads to high convective heat transfer coefficients, implying that the differnce of membrane temperature and free stream is small. The flow considered is laminar and steady in nature. It is also assumed that combustion doesn’t affect oxygen permeation flux equation. By considering the same boundary conditions for the case of mixing, single-step chemistry for methane combustion is activated to see the viability of ITM reactor.

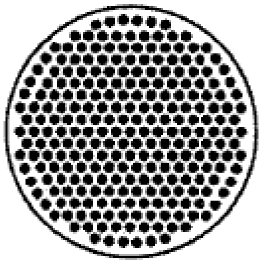

Figure 40. The cross section of the monolith reactor [92]

Table 4 List of model parameter values

Parameter	Value
$\dot{m}_{\text{inlet,permeate}}$	1.625×10^{-7} Kg/s
$\dot{m}_{\text{inlet,feed}}$	5.85×10^{-6} Kg/s
$T_{\text{inlet,permeate}}$	1073 K
$T_{\text{inlet,feed}}$	1073 K
$(Y_{CH_4};Y_{CO_2})_{\text{permeate}}$	0.33 ; 0.67
$(Y_{O_2};Y_{N_2})_{\text{air}}$	0.23 ; 0.77
ρ_{membrane}	3000 Kg/m^3
$\lambda_{\text{membrane}}$	20 W/m/K [96]

A reactive ITM combines the separation of oxygen from air and oxidation of methane in order to reduce the overall size of the reactor and number of equipments in cycle. The chemical reaction at the permeate side produces high partial pressure difference along the membrane which in turn increases the oxygen permeation flux significantly. If the fuel combustion kinetics are significantly faster than the rate at which oxygen is getting permeated through the ITM membrane, the partial pressure of oxygen at permeate side will be very low that significantly enhances oxygen flux. To study the ITM characteristics and combustion characteristics the numerical simulations are carried out with the conditions shown in table 4. Thermal conductivity of perovskite membranes such as LSCF, $BaCeO_3$, $BaZrO_3$ ranges from 5-12 W/m/K for temperature operation in the range 500-1000 ^oC [93,94, 95]. The thermal conductivity is still unknown for BSCF and the analysis done by Kaisare and Vlachos [96] suggested that for ceramic membrane the thermal conductivity is very low and varies from 3 to 100 W/m/K. In the present simulation the thermal conductivity of BSCF is assumed 20 W/m/K.

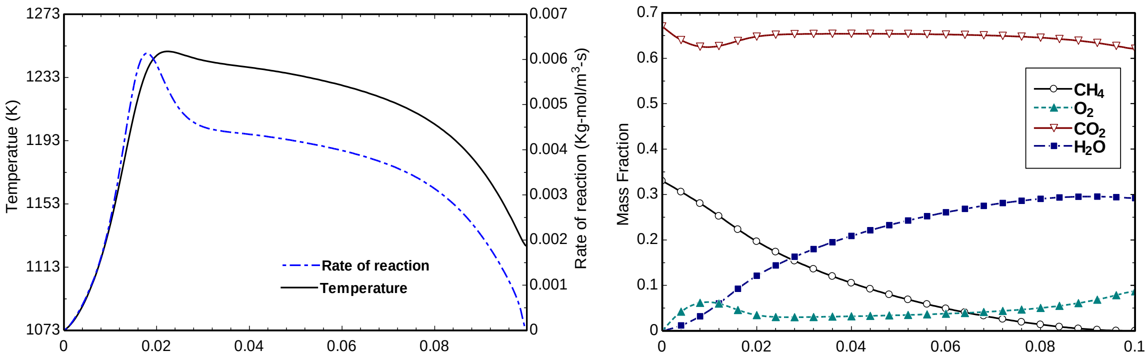

(a) (b)

Figure 41 Temperature, reaction rate and composition profiles

Figure 41 (a) shows the temperature and kinetic rate of reaction for the simulations conditions shown in table 5. The axial temperature within the reactor increases along with the rate of reaction and reaches a maximum of 1249.5 K then rate of reaction drops as the methane is getting consumed. Figure 41 (b) shows the composition profiles which indicates clearly where the fuel is consumed, and the mass fraction of O_2 increases downstream signifacantly. The mass fracton of O_2 first increases very fast then deceases till the methane is consumed, this is due to fast comsumption of fuel. For the given fuel mass fraction and mass flow rate in table 4, the amount of O_2 permeated through the membrane is 8.68×10^{-06} mol/s for the surface area of 12.56 cm^2 which constitutes of O_2/CH_4 of 5.178.

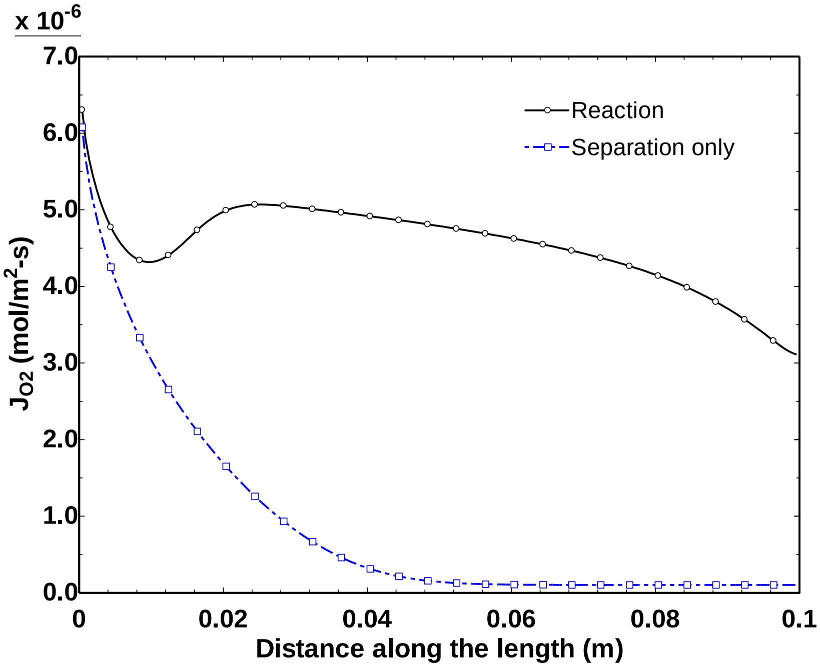

Figure 42 Oxygen permeation Flux for the reactive and separation only case.

Figure 42 shows the O_2 permeation flux (J_{O2}) for the same case considering reactive and separation-only modes. From the figure, it is clear that for the reactive case, the O_2 permeation flux decreases till the reaction starts then increases till the rate of reaction is maximum and then deceases gradually till fuel is totally consumed. It is evident from the figure that with the reaction mode at the permeate side, the O_2 permeation flux is very high compared to separation-only mode due to the high partial pressure difference of O_2 created across the membrane by chemical reaction. It gives conclusive remark that with chemical reaction for a particular membrane surface, the amount of O_2 permeated is higher compare to separation-only mode; thereby the length of the ITM reactor can be greatly reduced.

In order to study temperature and reaction kinetics for different sweep mixture compositions a parametric study is carried for the conditions shown in table 5.

Table 5 List of operating conditions for the reactive mode. Feed gas is air and sweep gas is CH_4/CO_2 mixture.

Case	P_{1,O_2} (atm)	Y_{CH_4} ; Y_{CO_2}	$\dot{m}_{permeate,inlet}\times10^{-7}$ (Kg/s)	$\dot{m}_{feed,\ inlet}\times10^{-6}$ (Kg/s)
1	0.21	0.1 ; 0.9	1.625	5.85
2		0.3 ; 0.7		
3		0.5 ; 0.5		
4		0.7 ; 0.3		
5		1.0 ; 0		
6	0.21	0.1 ; 0.9	4.625	5.85
7		0.3 ; 0.7		
8		0.5 ; 0.5		
9		0.7 ; 0.3		
10		1.0 ; 0		
11	0.21	0.1 ; 0.9	8.625	5.85
12		0.3 ; 0.7		
13		0.5 ; 0.5		
14		0.7 ; 0.3		
15		1.0 ; 0		

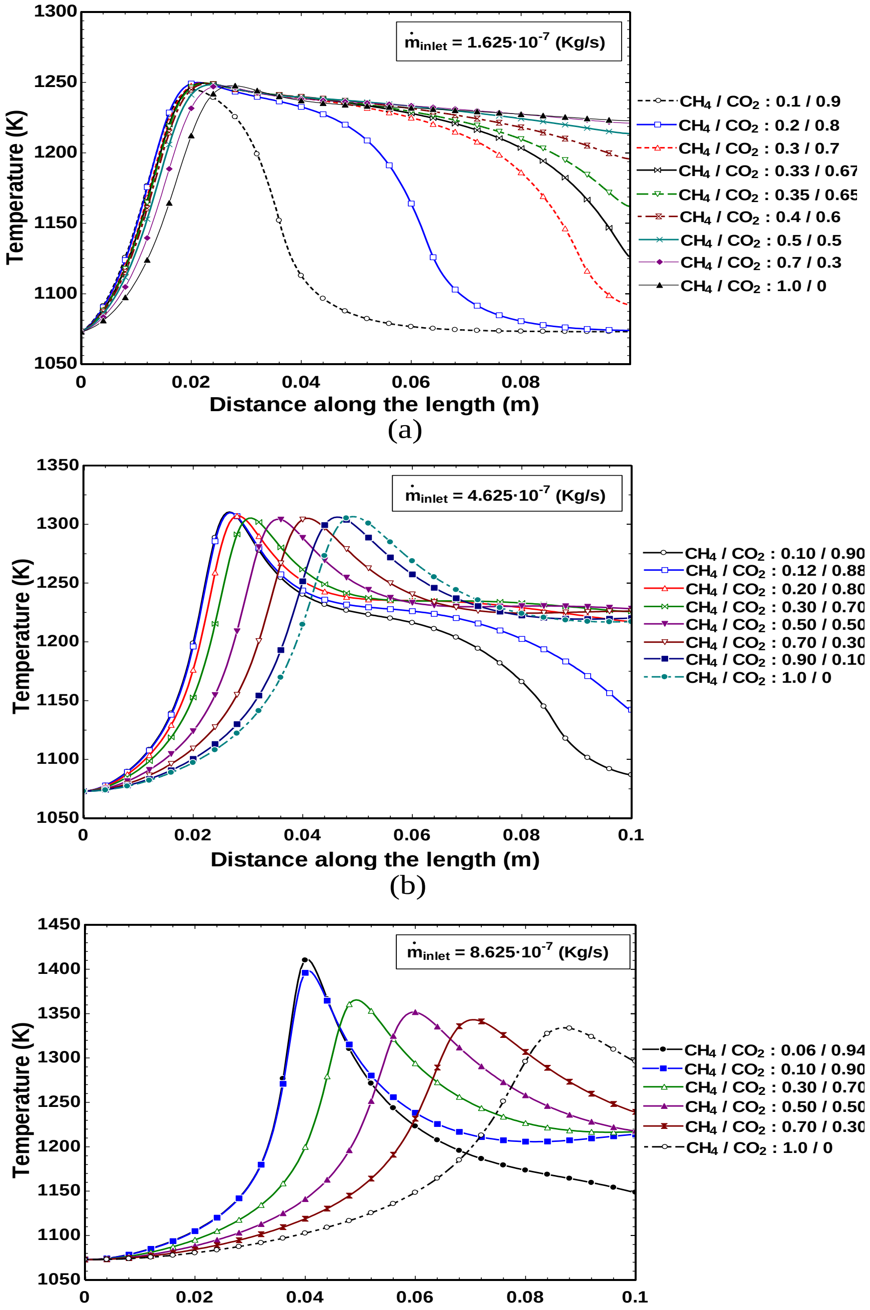

(a)

(b)

(c)

Figure 43 Temperature profiles for the different sweep gas mixture for three different mass flow rates.

5.2.1 Temperature characteristics:

The axial temperature profiles within the reactor for different sweep gas mixture composition are shown in Figure 43. For the low mass flow rate of 1.625×10^{-7} Kg/s at the inlet the temperature rises quickly to 1250 K at 1/5th of the length from inlet of the reactor and then downstream. This drop is due to the cooling of the flue gases by permeating O_2 from the membrane. When the mixture composition of CH_4/CO_2 (mass ratio m_R) increases beyond 0.4/0.6, the exit temperature of the reactor becomes almost constant at about 1222 K. Figure 43 (b) shows the temperature profile for the mass flow rate of 4.625×10^{-7} Kg/s for the same composition mixtures mentioned in table 5. From the figure, it is evident that the maximum temperature reaches 1310 K for almost all the mass ratios m_R and the exit temperature is about 1220 K except for the first two cases of mass ratio m_R of 0.1/0.9 and 0.12/0.88. This is mainly because the fuel is completely consumed within the reactor and the incoming O_2 lower the exit temperature to 1142 K for the case with the mass ratio m_R of 0.12/0.88. Figure 43 (c) shows the temperature profile for the mass flow rate of 8.625×10^{-07} Kg/s where the maximum temperature drops from 1411 K to 1334 K for the composition CH_4/CO_2 mass ratio of 0.06/0.94 to 1.0/0. Unlike the cases of mass flow rate of 1.625×10^{-07} Kg/s and 4.625×10^{-07} Kg/s, the exit temperature in the present case varies for the from 1214 K to 1297 K composition mass ratio m_R of 0.1/0.9 to 1.0/0 except for 0.06/0.94 is 1149 K and this is due to the complete combustion before the exit of the reactor and it can be clearly explained by the rate of reaction profiles.

Figure 44 shows the rate of reaction profiles for the aforementioned mass flow rates of 1.625×10^{-07} Kg/s, 4.625×10^{-07} Kg/s and 8.625×10^{-07} Kg/s. In figure 44 (a), it is shown that the rate of reaction reaches to nearly 0.0062 Kg-mol/m^3-s and drops along the length of the reactor. For the composition CH_4/CO_2 mass ratio m_R of 0.1/0.9 to 0.3/0.7 the rate of reaction becomes zero within the reactor and for m_R = 0.33/0.67 the rate of reaction becomes zero at exit of the reactor and this is due to the fact the fuel is totally consumed. It is noted that temperatures and rate of reaction profiles for the m_R ranging from 0.5/0.5 to 1.0/0 is almost the same leaving some unburned fuel at the exit with high temperatures. If the reactor is designed to follow uniform temperature combustion process more closely, then the temperature related problems could be significantly mitigated. So, the composition m_R = 0.5/0.5 to 1.0/0 could be used and the ITM reactor could be split into a series of units where the exhaust of the first reactor unit is feed in second and so on till the fuel is totally consumed. With increase of mass flow rate from 1.625×10^{-07} Kg/s to 4.625×10^{-07} Kg/s the maximum value of rate of reaction increased to 0.00108 Kg-mol/m^3-s and the reaction started earlier at the left side of the reactor. This is due to the fact the rate of O_2 permeation is same but the velocity of fuel is increased and hence it takes time to start the reaction kinetics.

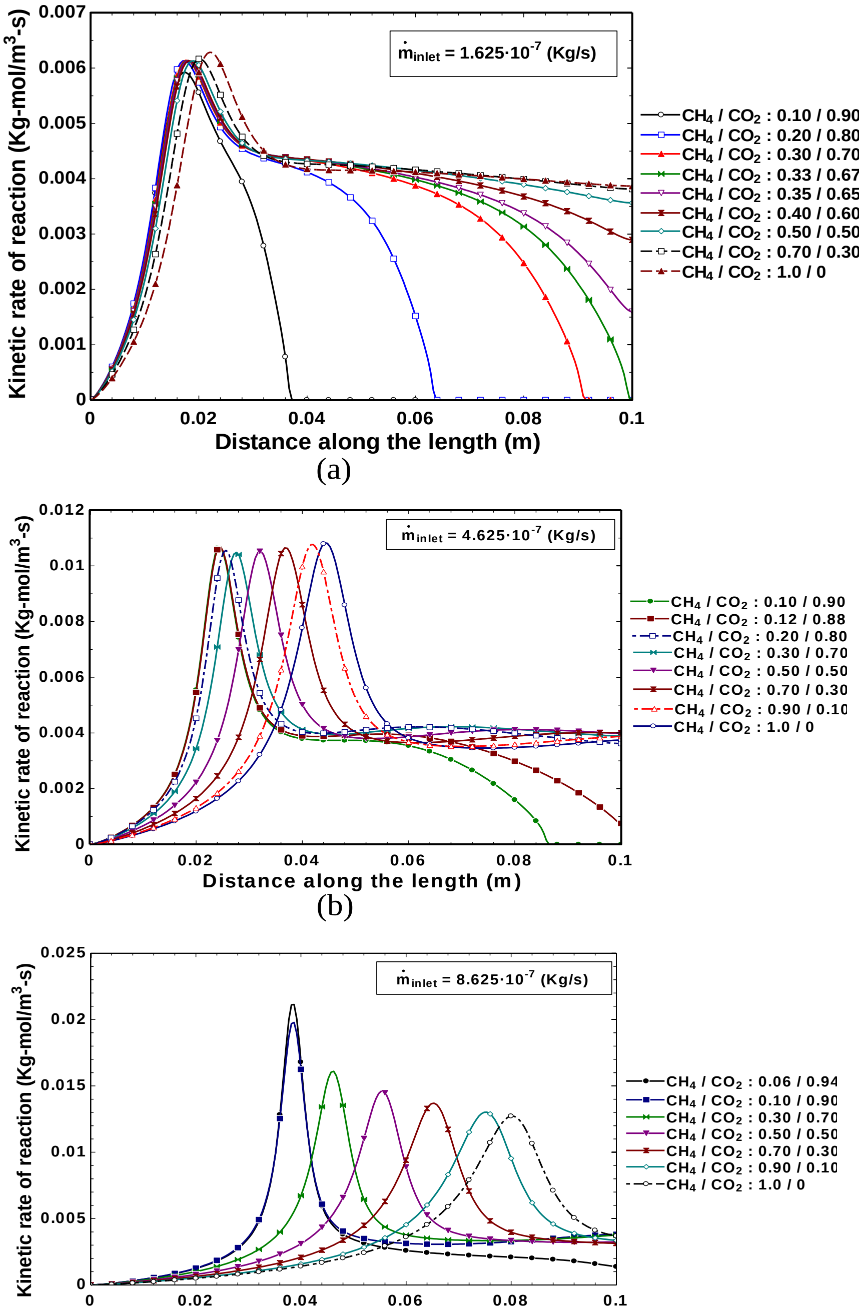

(a)

(b)

(c)

Figure 44 Kinetic rate of reaction profiles for different sweep gas mixture for three different mass flow rates.

Figure 44 (c) shows the reaction rate profiles for the mass flow rate of 8.625×10^{-07} Kg/s. It can be seen that the magnitude of maximum reaction rate decreases as we increase m_R and the start of the reaction shifts to almost middle of the reactor, this is due to the fact the O_2/CH_4 value decreases along the length of the reactor and can be seen in Figure 45. It is clear from the figure that for high mass flow rate, the increase of CH_4 content reduces the reaction kinetics and the CH_4 conversion percentage gets reduced. From the above discussion, it can be concluded that with less diluent CO_2 at inlet high maximum temperatures can be achieved for increasing mass flow rate. This is accompanied by a reduction in conversion percentage of CH_4. With split ITM reactor design, the problem of fuel conversion can be overcome with uniform temperature along the reactor.

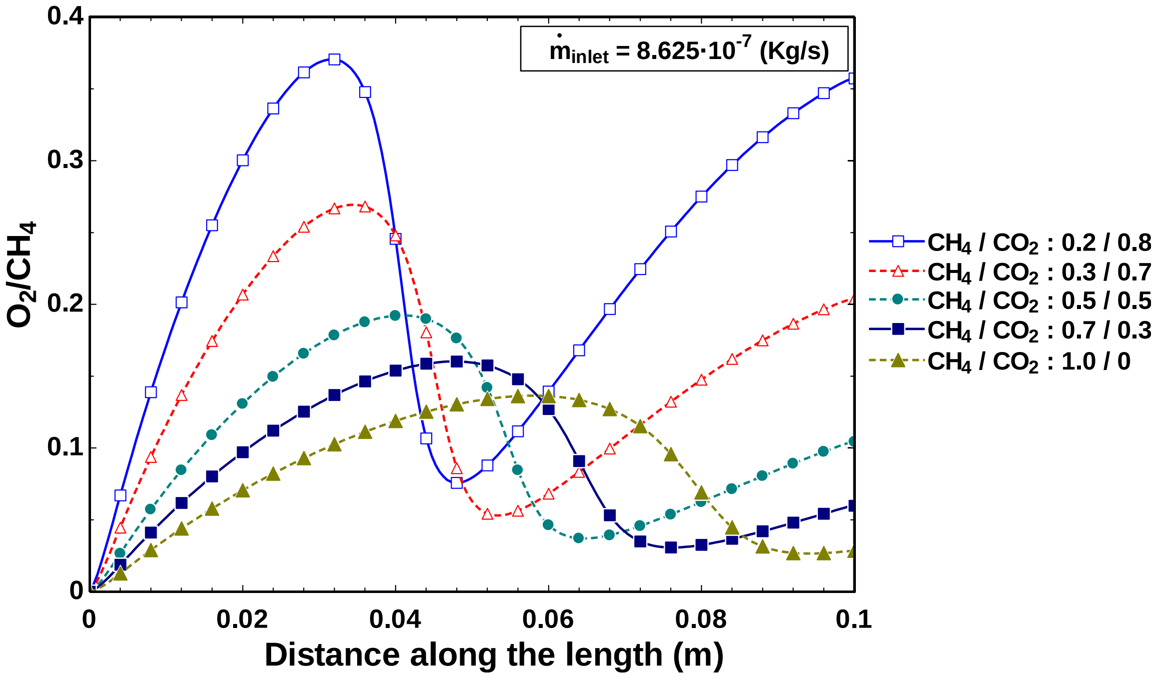

Figure 45 O_2/CH_4 profiles for the different sweep gas composition

5.2.2 Combustion characteristics:

For the optimal design of ITM reactor which combines O_2 separation and fuel oxidation, the amount of CH_4 conversion is an important parameter that is affected by the diluent CO_2 concentration and O_2 permeation flux. Figure 46 shows the CH_4 mass fraction profiles for different CH_4/CO_2 m_R compositions for increasing mass flow rates. It is evident that the conversion of CH_4 to combustible products decreases with the increase of CH_4 percentage at the inlet. For more diluent of CO_2 at higher mass flow rate at inlet, the maximum temperature is reached but the exit temperature for all the simulations ranges from 1148 K to 1297 K. In order to increase the O_2 permeation flux from ITM there must be sufficient methane input so that the chemical reaction doesn't stop at the first part of the reactor. For m_R in the range 0.1/0.9 to 0.3/0.7 for mass flow rate of 1.625×10^{-07} Kg/s all the CH_4 is consumed and the permeating O_2 downstream cools the flue gases resulting in a decrease in the temperature. As discussed earlier, for the case of m_R of 0.33/0.67 in figure 41, the reaction ends near the exit of the reactor and ΔT is not much less compared to the lower percentage of CH_4 at inlet. For $m_R > 0.33/0,67$ in feed for mass flow rate of 1.625×10^{-07} Kg/s, the CH_4 conversion reduced to 36.8% for $m_R = 1.0/0$ can be seen in figure 47. For the mass flow rate of 4.625×10^{-07} Kg/s 100% CH_4 conversion is obtained for $m_R = 0.12/0.88$ or less and CH_4 conversion is greatly reduced to 13.5% for $m_R = 1.0/0$. The mass flow rate of 8.625×10^{-07} Kg/s yields to 7.5% CH_4 conversion for $m_R = 1.0/0$ and 100% CH_4 conversion at very low $m_R = 0.06/0.94$ or less. On the whole, the amount of CH_4 burned does not vary much since it depends on the O_2 available for combustion. In order to get to burn more amount of CH_4, the surface area of the membrane must be increased in such a way that the surface to volume ratio of the reactor must be high. Figure 46(b) and (c) depicts that the consumption of CH_4 is delayed due to the increase of the flow velocity and hence the length to attain O_2-CH_4 in flammability limit is increased. In order to maintain a uniform temperature within the reactor, the maximum methane percentage is required, from the three mass flow rates presented 1.625×10^{-07} Kg/s, 4.625×10^{-07} Kg/s, and 8.625×10^{-07} Kg/s, the lowest giving the uniform temperature with the composition of m_R above 0.5/0.5.

Figure 48 show the percentage of CH_4 and O_2 conversion for increasing percentage of CH_4 at the inlet. It is evident from the figure, that upto 33% of CH_4 at inlet with flow rate of 1.625×10^{-07} Kg/s the CH_4 conversion is 100%. O_2 conversion increases till 40% CH_4 and becomes constant with 93% conversion. Figure also represents the O2 permeation rate which becomes constant above 33% CH_4 at inlet to a value of 9.33×10^{-06} mol/s, similar profile for O_2 permeation rate and conversion of CH_4 and O_2 is obtained by Tan et al [57] for LSCF-ITM membrane.

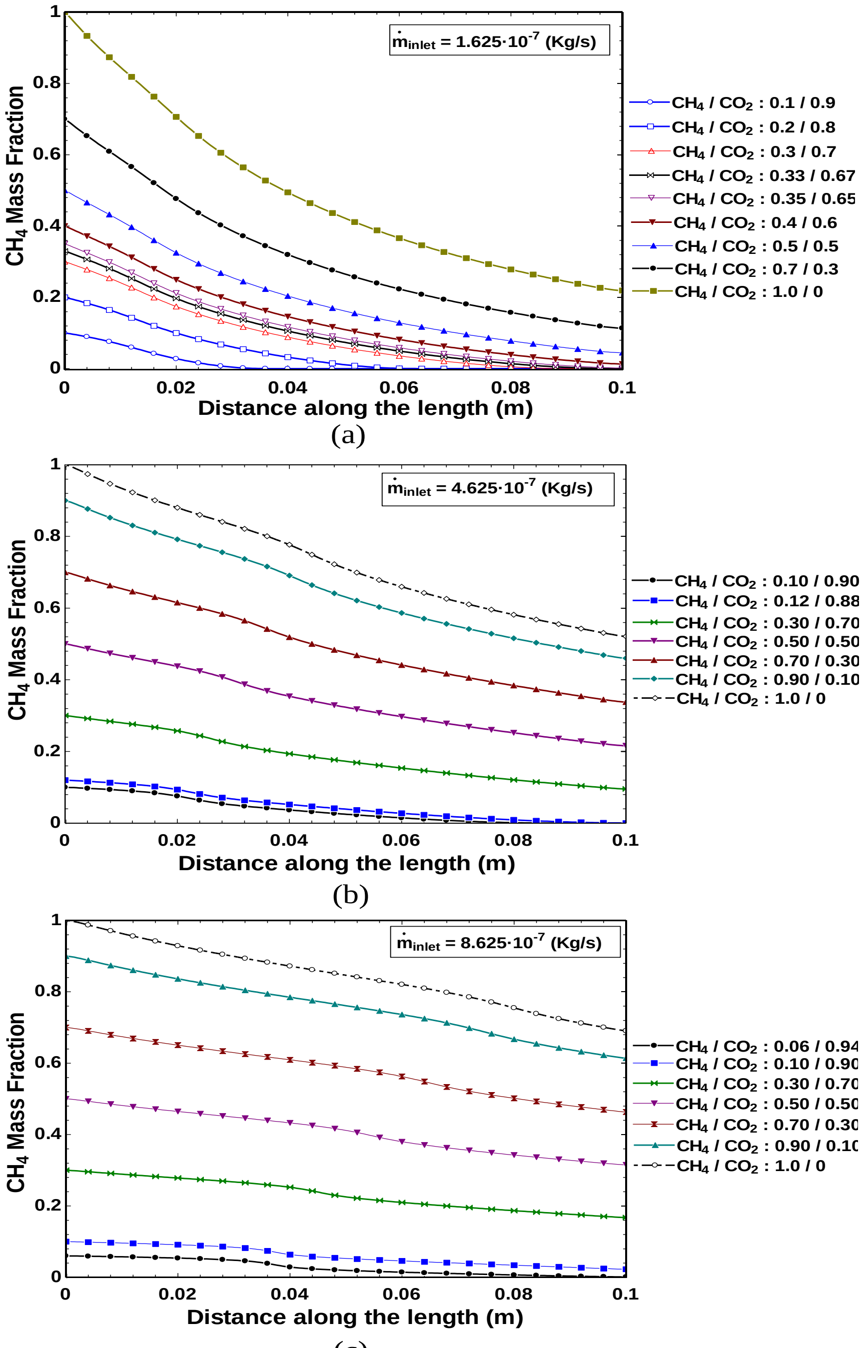

(a)

(b)

(c)

Figure 46 CH_4 Mass fraction profiles for different sweep gas composition

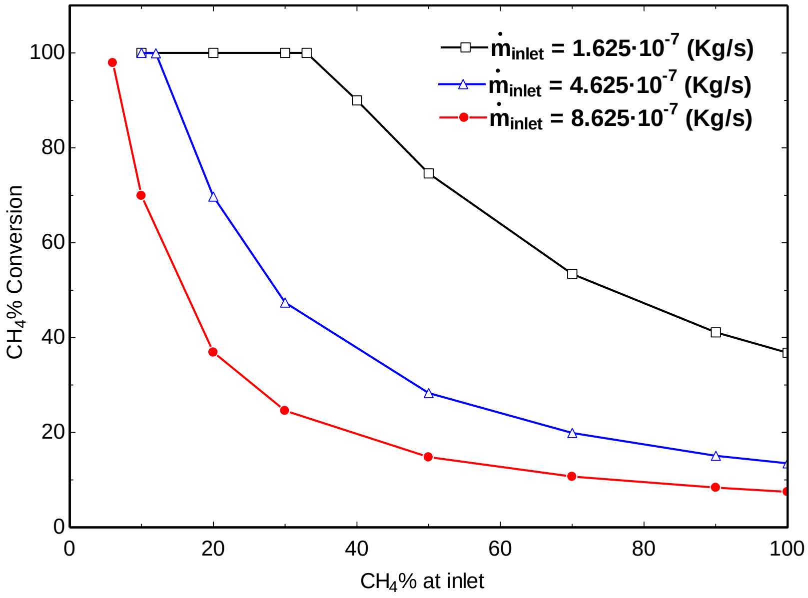

Figure 47 Percentage CH_4 conversion for different mass flow rates

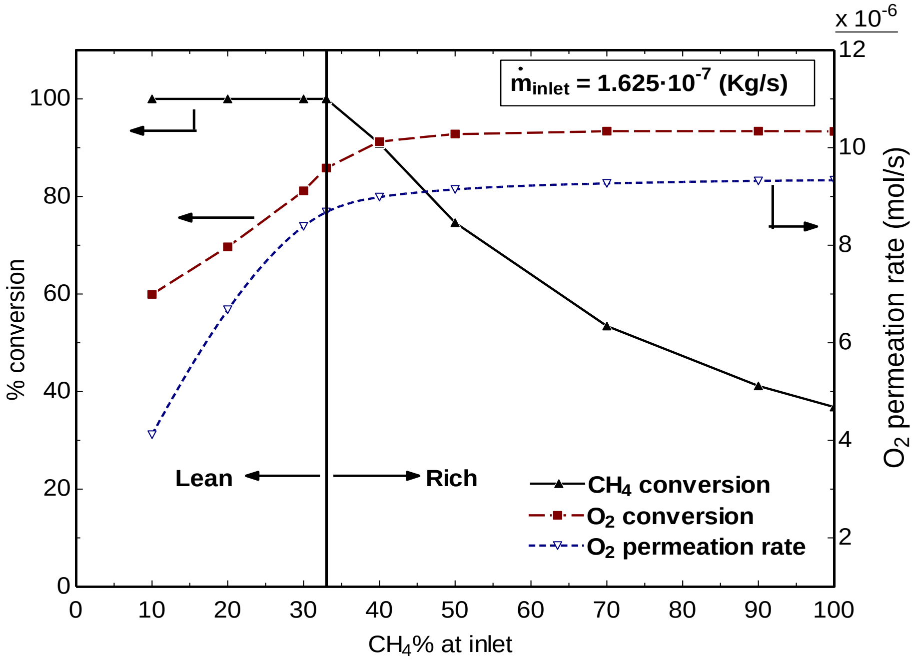

Figure 48 Percentage of O_2 & CH_4 conversion and O_2 permeation rate for mass flow rate of 1.625×10^{-07} Kg/s

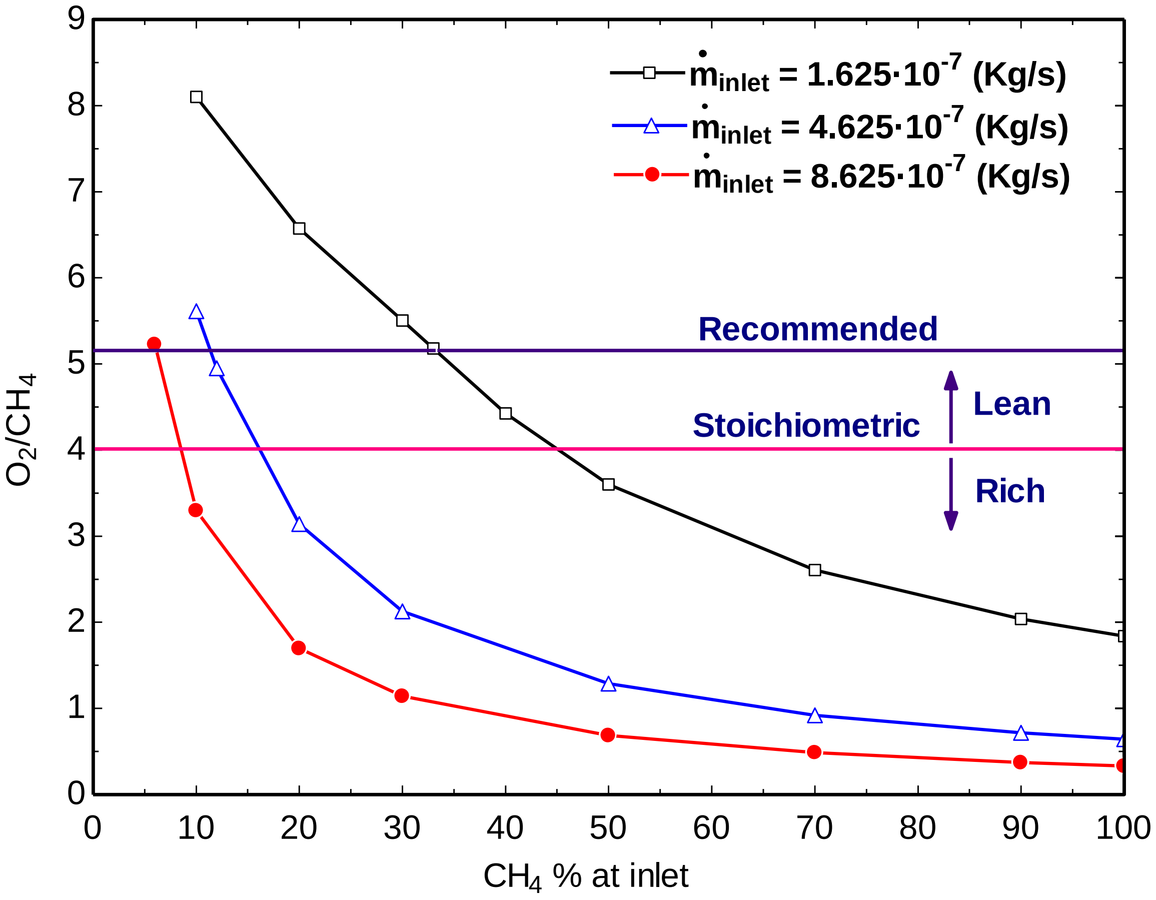

Figure 49 O_2/CH_4 vs Percentage of CH_4 at inlet for different mass flow rates

O_2/CH_4 value is an important parameter to decide the region of flammability limit for combustion. Figure 49 shows the representation of all the three mass flow rates with different CH_4% at inlet. It can be seen that the only low mass flow rate of 1.625×10^{-07} Kg/s comes under lean region with 100% conversion of CH_4 with O_2/CH_4 value of 5.178. This is because the combustion of CH4 in ITM reactor is non-premixed and is highly dependent on mixing of species.

Figure 50 shows the O_2 mass fraction for increasing CH_4% concentration at inlet for three different mass flow rates. The O_2 mass fractions are important since the mass fraction is related with mole fraction. Since the ITM reactor is operating at atmospheric pressure, the mole fraction is nothing but O_2 partial pressure and permeation rate is highly dependent on that O_2 partial pressure. Figure 50 and 51 are related since O_2 permeation flux J_{O2} is dependent on O_2 partial pressure across the membrane. Since the O_2 partial pressure at feed is fixed (0.21 atm) as per equation (36) then variation of J_{O2} is more governed by O_2 partial pressure at permeate side than temperature since the temperature rise within the reactor is nearly of the order of 200 K. The lesser the O_2 partial pressure at the permeate side the higher the O_2 permeation flux. Figure 50 (a) shows, that the O_2 partial pressure is zero at inlet of the permeate side and hence the maximum O_2 permeation flux. Along the length of the reactor O_2 mass fraction increases till O_2 is sufficient to burn CH_4 then decreases till the reaction rate becomes maximum. For m_R of 0.1/0.9 the reaction is ended at X/L of 0.25 as the total CH_4 is consumed and O_2 mass fraction increases downstream while O_2 permeation decreases till the exit of the reactor. For the m_R ranging from 0.2/0.8 to 0.33/0.67, the trend of O_2 mass fraction follows as that of previous ratio except the magnitude increases and reaction zone increased. For higher $m_R > 0.33/0.67$, the O_2 mass fraction is almost constant leading to almost constant O_2 permeation flux as shown in Figure 51 (a). For the increased mass flow rates at inlet of 4.625×10^{-07} Kg/s and 8.625×10^{-07} Kg/s the maximum value of O_2 mass fraction is almost the same but the peak is shifted from X/L of 0.25 to 0.6. This is attributed to the shift in the rate of reaction as can be seen in figure 34. At the higher mass flow rate of

8.625×10^{-07} Kg/s, the O_2 permeation flux decreases till X/L of 0.7 for $m_R = 1.0/0$. From the above discussion, it is depicted that for an ideal ITM reactor the mass flow rate of 1.625×10^{-07} Kg/s with composition m_R of above 0.5/0.5 to 1.0/0 is suitable for uniform temperature operations. This results in maximum O_2 permeation flux with 75% CH_4 conversion for $m_R = 0.5/0.5$ to 37% for $m_R = 1.0/0$. A simple analysis of Figures 38 and 51 (a) shoes that the oxygen permeation flux through this type of membranes is more sensitive to the changes in O_2 partial pressure in the reaction side. For the case without reaction (separation-only), oxygen permeate does not react with the sweep gases (CH_4+CO_2). Therefore, O_2 partial pressure at permeate side (P_2) is much larger in the case of non-reacting medium. As a result, the driving force $[(P_1)^{1/2} - (P_2)^{1/2}]^{0.623}$ is lower than that in the case of combustion.

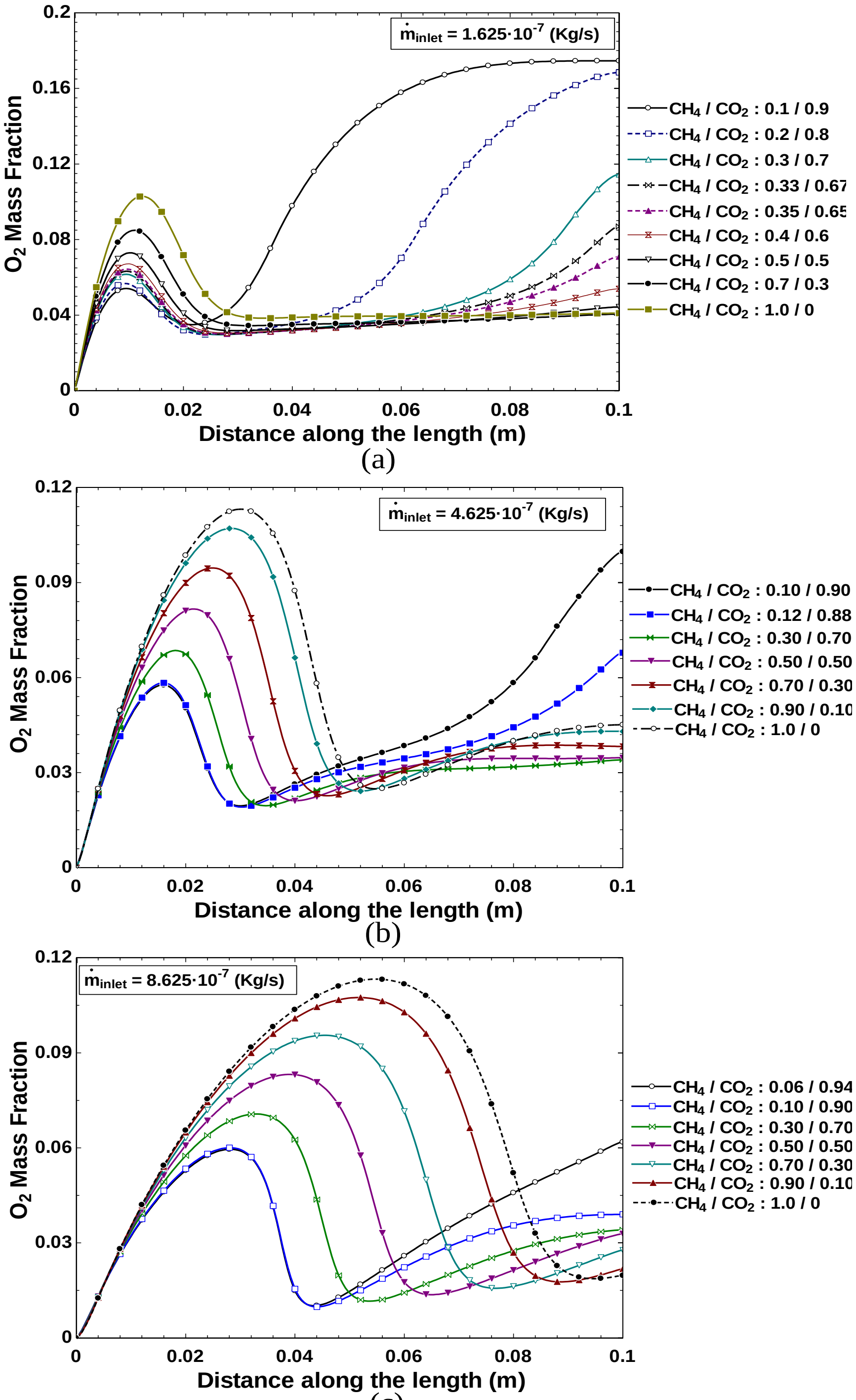

(a)

(b)

(c)

Figure 50 O_2 Mass Fraction Profiles for different sweep gas composition

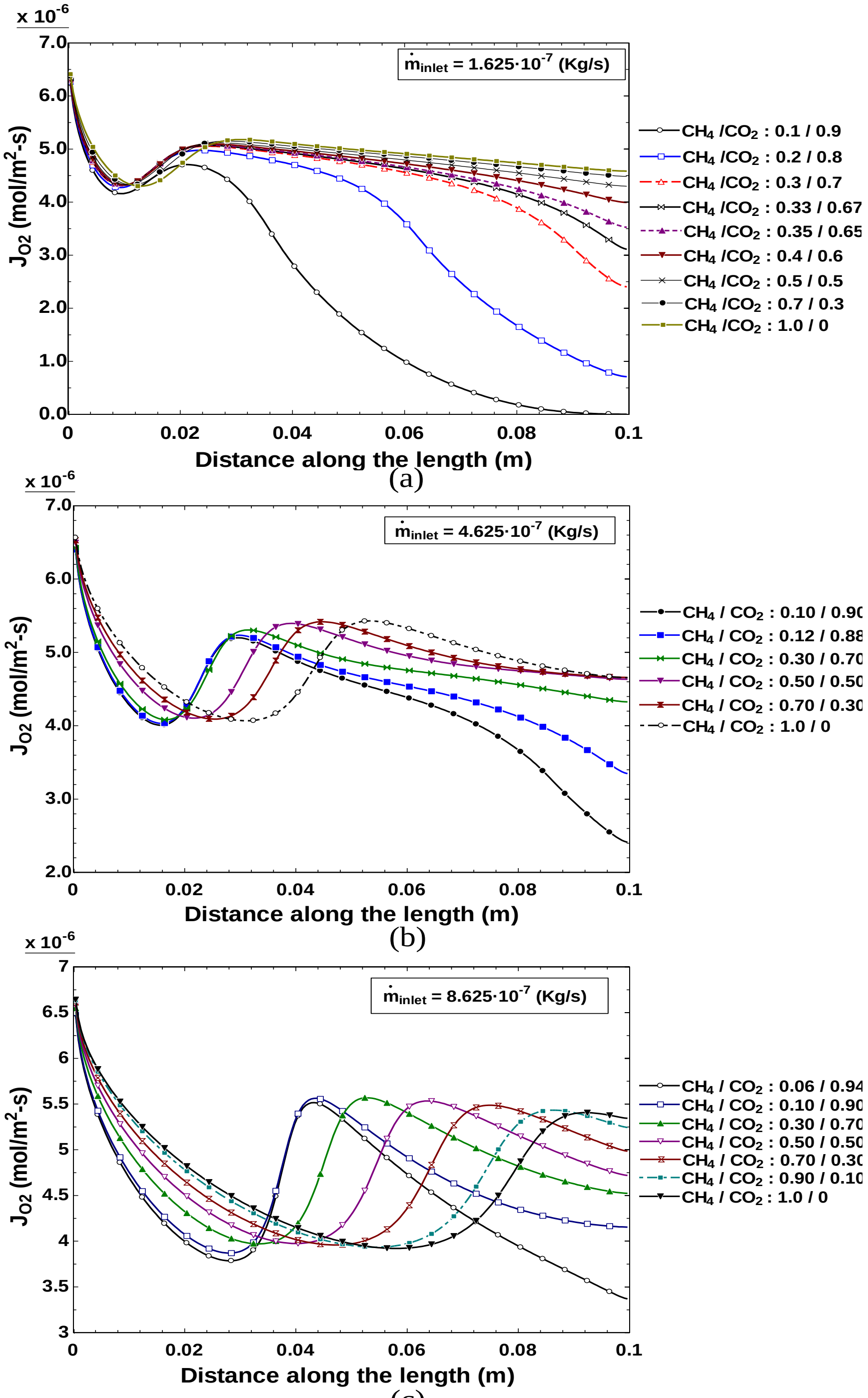

Figure 51 O_2 Permeation flux for different sweep gas composition

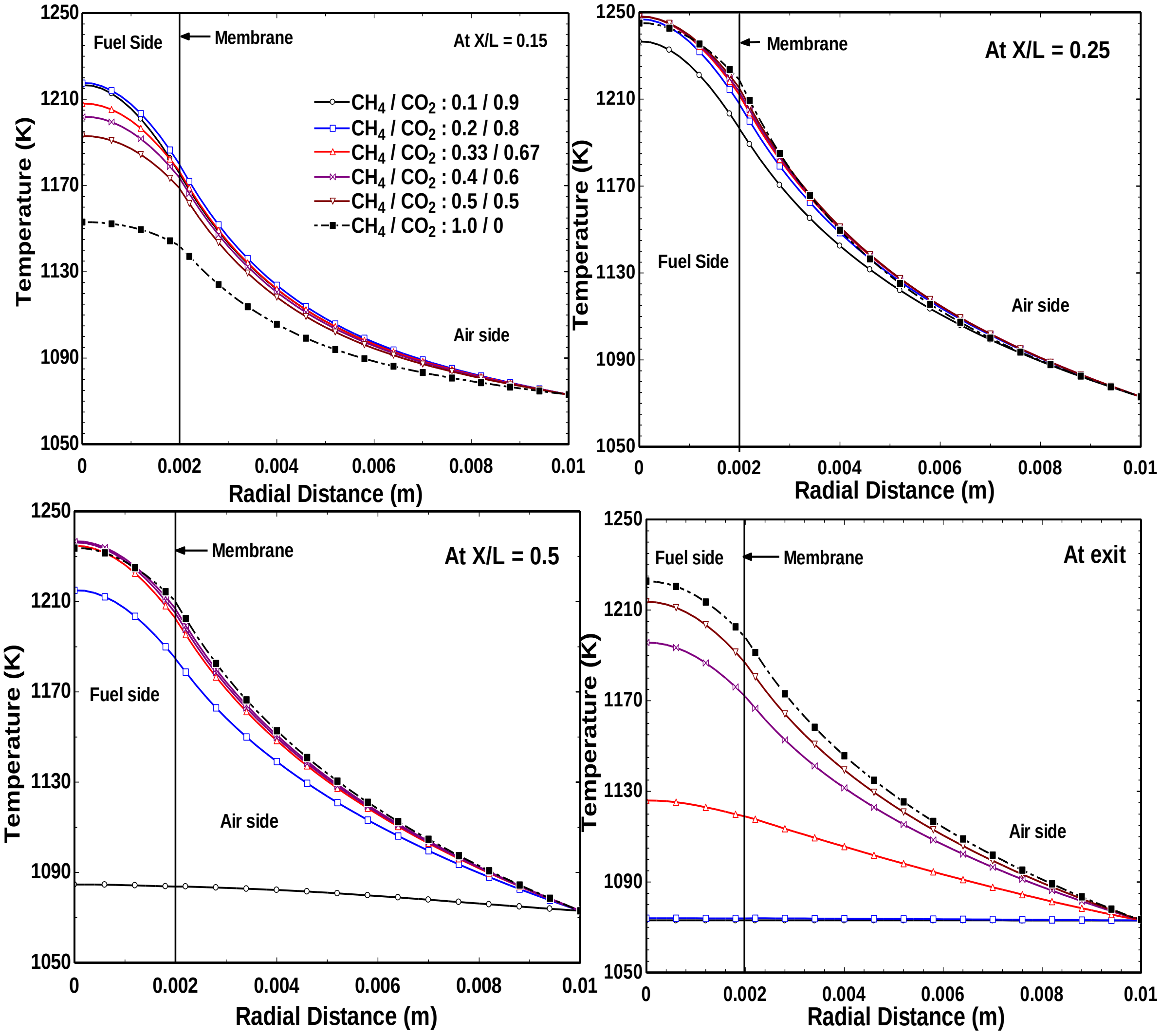

Figure 52 Radial temperature profiles at different sections for mass low rate of

1.625×10^{-07} Kg/s

Figure 52 shows the radial temperature profiles at different sections (X/L = 0.15, 0.25, 0.5 and at 1.0) for the mass flow rate of 1.625×10^{-07} Kg/s. At X/L=0.15, the reaction is just started and the temperature start rising and at X/L=0.25 the reaction rates are maximum for almost all composition mixtures. At X/L=0.5 the temperature is dropped for low CH_4 mixture composition due to the depletion of CH_4. The temperature dropped for m_R less than 0.5/0.5 at exit due drop of high CH_4 conversion.

Figure 53 shows the radial profiles of O_2 mass fraction for a mass flow rate of 1.625×10^{-7} Kg/s for three different m_R of 0.1/0.9, 0.5/0.5 and 1.0/0 at four different sections (X/L=0.15, 0.25, 0.5, 1.0). It can be seen that at X/L =0.15 the O_2 mass fraction at feed side drops significantly from 0.225 to 0.218 radially from outer wall of the shell to the membrane surface. At this section O_2 mass fraction at permeate of m_R= 0.1/0 is very low compare to m_R= 0.5/0.5 and 1.0/0 due to early reaction initiation. At section X/L =0.25 the reaction rate of m_R= 0.5/0.5 is maximum compare to other m_R considered. It can be seen that the variation of O_2 mass fraction radially is maximum in this section which gives maximum temperature. From the section X/L =0.5 and 1.0, it is clear that the CH_4 is totally consumed for m_R = 0.1/0.9 and there is no much variation of O_2 mass fraction radially. For m_R = 0.1/0.9 and 1.0/0 there is no much difference in magnitude of O_2 mass fraction and it can be radial temperature profiles (Figure 52) that there is no much difference in their magnitude this is due to O_2 permeation flux becomes constant after m_R =0.33/0.67 which can be seen in figure 48. Figure 54 shows the temperature and composition profiles in radial direction for m_R =0.5/0.5 for mass flow rate of 1.625×10^{-7} Kg/s at different sections (X/L=0.15, 0.25, 0.5, 1.0). It can be seen that the maximum temperature and maximum ΔT along the radial direction is achieved at X/L=0.25, 0.5 and ΔT_{max} is 40 K.

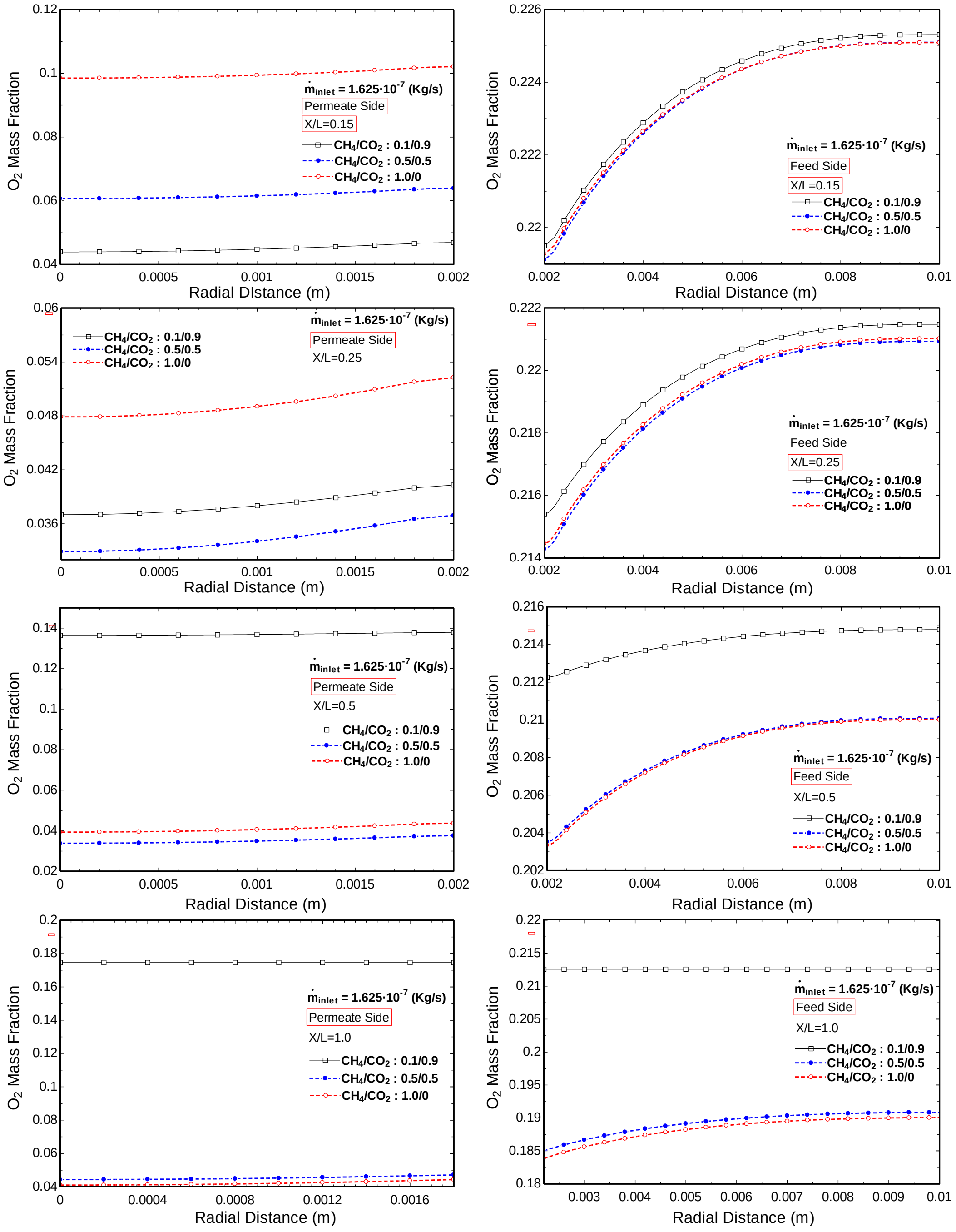

Figure 53 O_2 mass fraction radial profiles for mass flow rate of 1.625×10-7 Kg/s

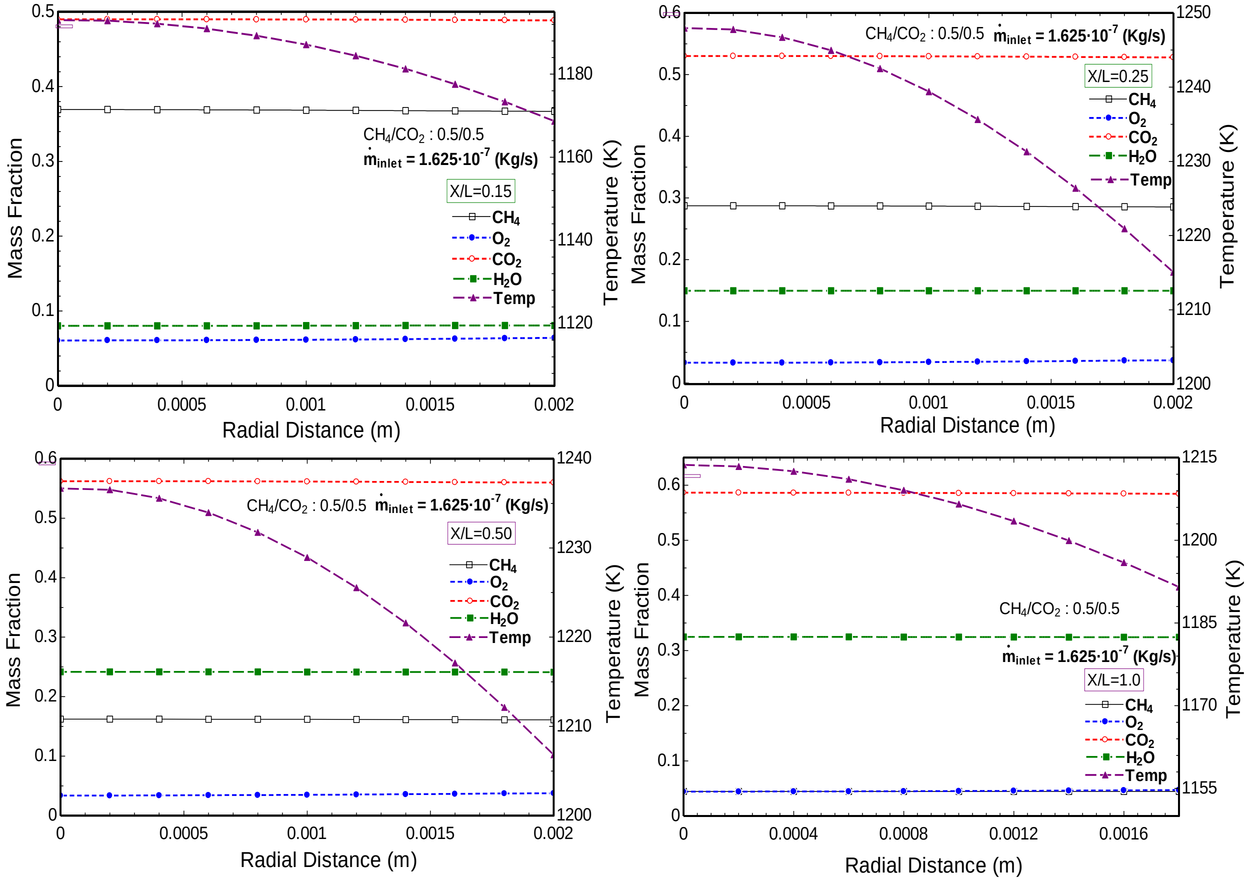

Figure 54 Radial temperature and composition profiles for mass flow rate of 1.625×10^{-7} Kg/s for m_R of 0.5/0.5

Figure 55 shows the temperature, composition profiles for one m_R of 0.5/0.5 for increasing mass flow rates. It can be seen from the figure that the difference in axial temperature and membrane temperature is around 30 K only. For the low mass flow rate CH_4 conversion achieved is highest and the uniform temperature is achieved where the O_2 mass fraction is lowest. After X/L=0.25 the temperature drops and it is attributed to the decrease in the reaction rate because of increasing value of O_2/CH_4. For mass flow rate of 1.625×10^{-7} Kg/s the maximum temperature is increased to 1310 K but the reaction zone is shifted and reaction is delayed to achieve O_2/CH_4 ratio for combustion. The same phenomenon is observed for high mass flow rate of 8.625×10^{-7} Kg/s and the conversion of CH4 is reduced significantly. This data gives information in designing OTR to maintain uniform temperature as well as the amount of CH_4 that can be burnt for a particular surface area membrane reactor.

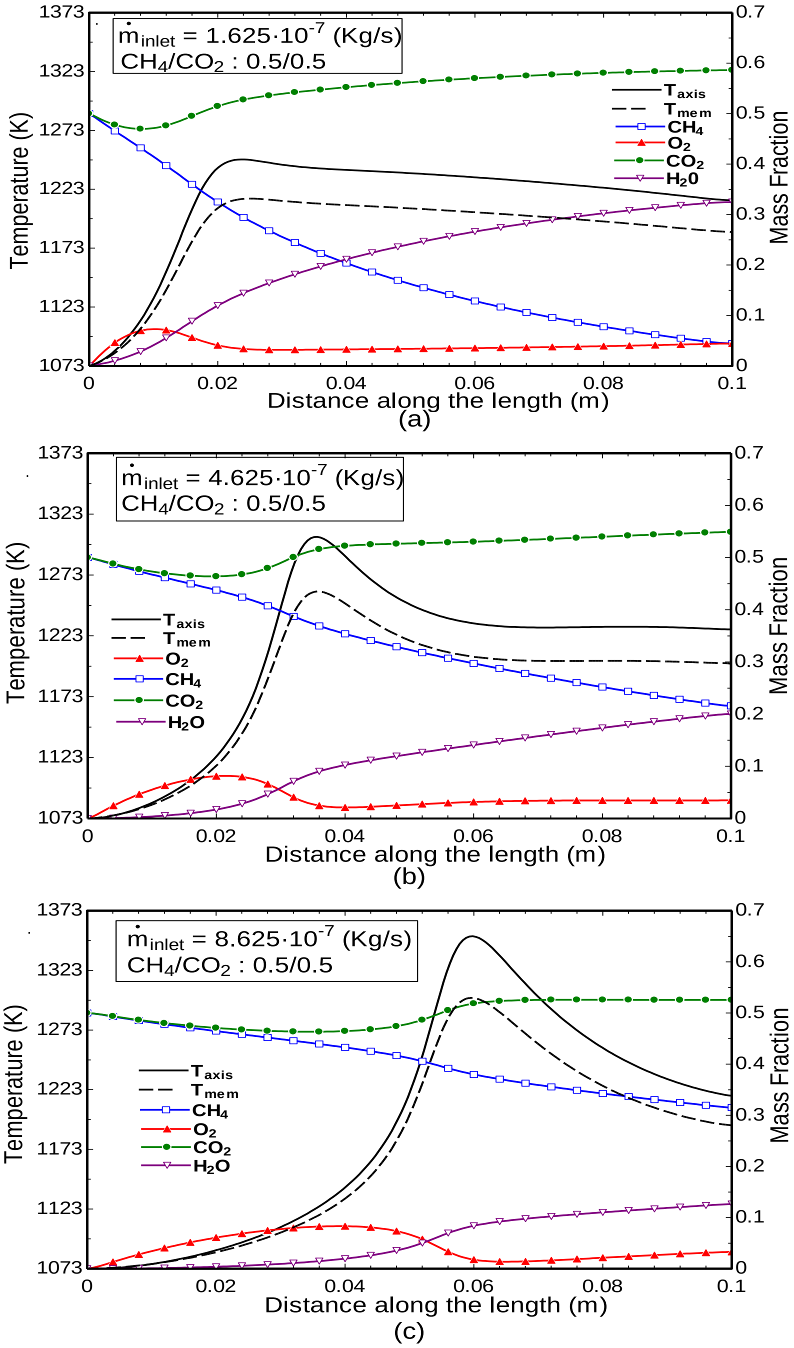

Figure 55 Temperature and composition profiles for three different mass flow rates at m_R =0.5/0.5

5.2.3 Effect of fuel mass flow rate on O_2 permeation flux (J_{O2}):

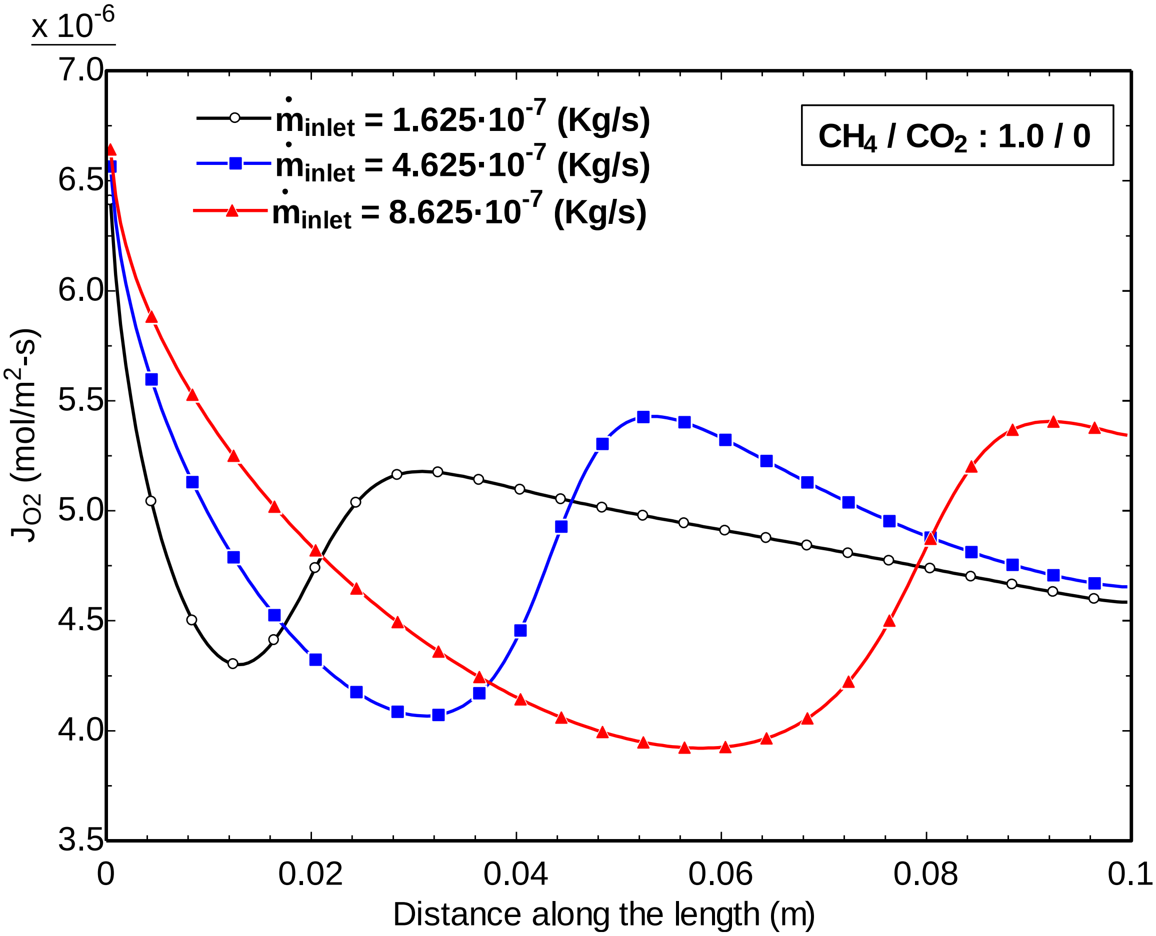

Figure 56 Effect of mass flow rate of fuel on the oxygen permeation flux

The mass flow rate of fuel (CH_4 and CO_2) has a great effect the oxygen permeation flux through ITM. As shown in Figure 56, the increase in sweep gas mass flow rate tends to decrease the O_2 permeation flux for a prolonged distance. Furthermore, the reaction side O_2 partial pressure increases till the reaction starts and then drops and becomes constant for low mass flow rate because of the extinction of fuel.

5.2.4 Effect of fuel mass flow rate on combustion temperature:

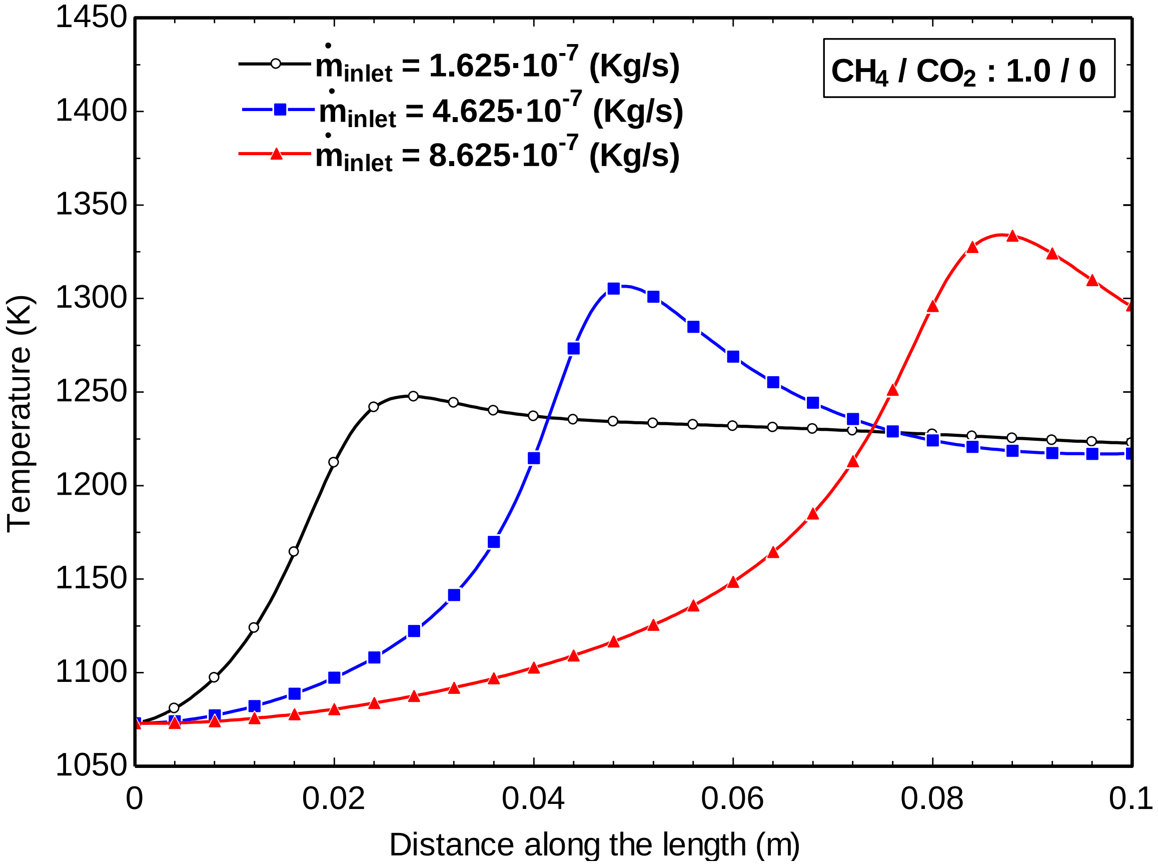

Figure 57 Temperature profiles for different fuel mass flow rates

Figure 57 presents the effect mass flow rate of fuel on the combustion temperature. The figure shows an increase of the combustion temperature with increasing sweep gas mass flow rate till a certain value and then starts to decrease except for mass flow rate of 1.625×10^{-07} Kg/s where the uniform temperature is maintained in more than 75% of the reactor. With increase of fuel mass flow rates, peak temperature increases and then drops but the condition of nearly isothermal operation can be achieved.

5.2.5 Effects of fuel mass flow rate on permeate O_2 partial pressure:

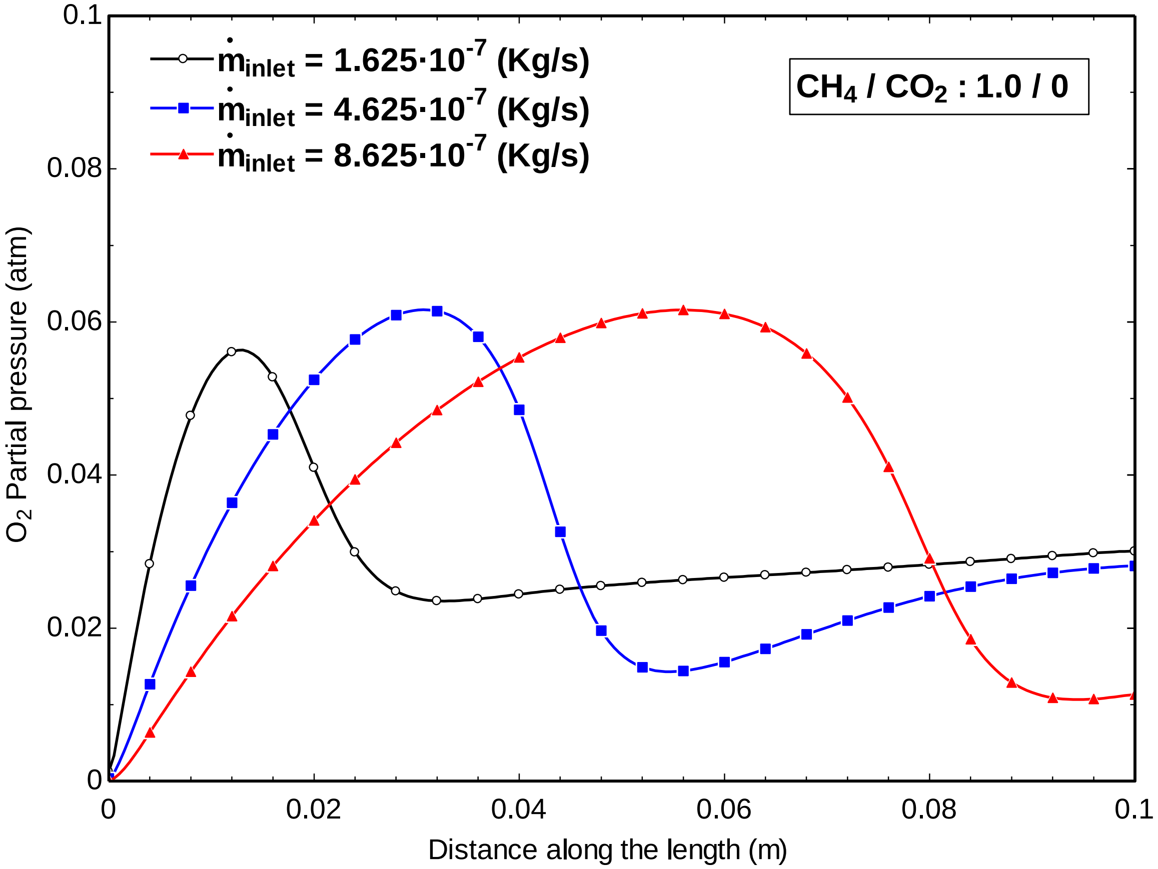

Figure 58 O_2 partial pressure profiles for different fuel mass flow rates

Figure 58 shows the change in oxygen partial pressure as a function of sweep gas mass flow rate for the case when combustion is activated at constant feed oxygen partial pressure of 0.21atm. As shown in the figure, the permeate O_2 partial pressure increases tending to lowering the O_2 permeation flux then when O_2/CH_4 reaches the flammability limit, the O_2 partial pressure drops leading to increase in O_2 permeation flux. This can be easily seen in Figures 50 and 51 which shows the O_2 mass fraction and O_2 permeation flux profiles for increasing sweep gas mass flow rate.

5.2.6 Effect of mass flow rate on O_2/CH_4 ratio:

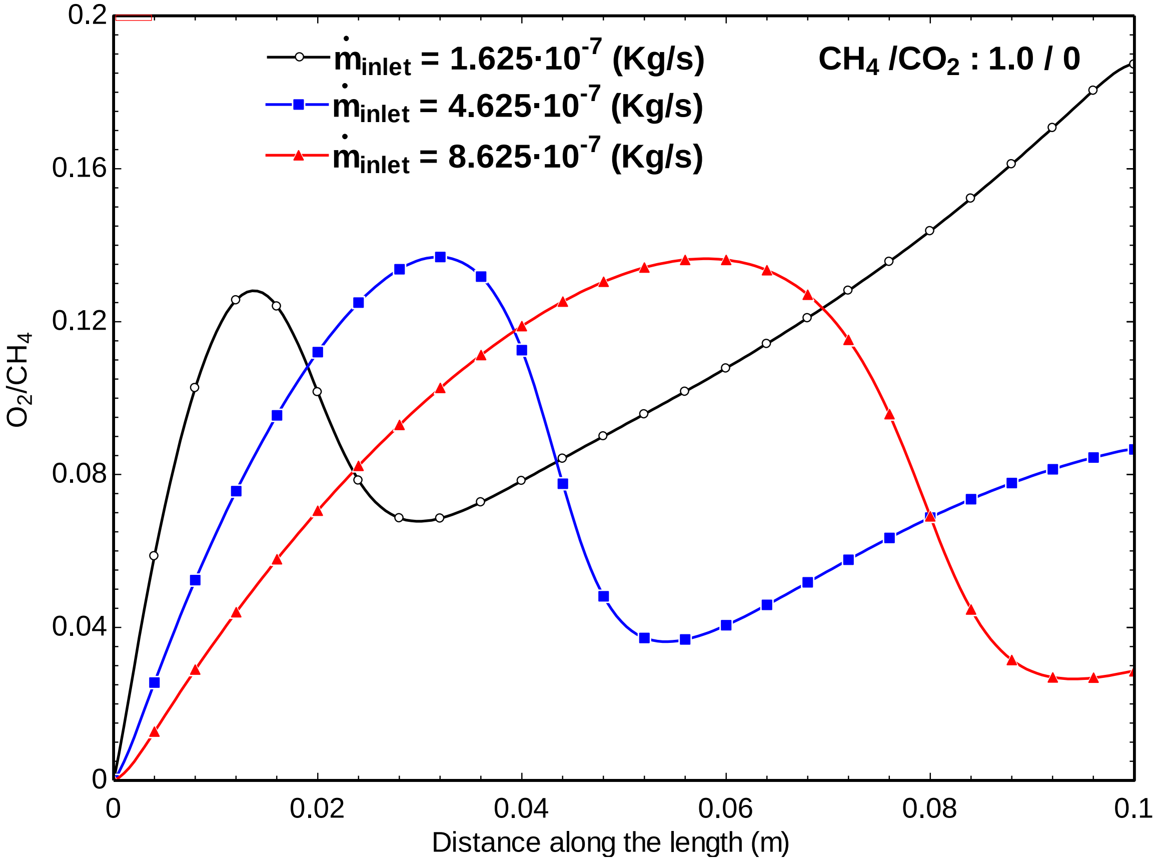

Figure 59 O_2/CH_4 for different mass flow rates

Figure 59 shows the O_2/CH_4 profiles for the different mass flow rate for the sweep gas composition m_R of 1.0/0. With increase of mass flow rate, the O_2/CH_4 ratio increases but the reaction zones shifts near to the exit of the reactor. The maximum temperature is achieved when the peak O_2/CH_4 drops for all the three mass flow rates and can be seen in Figure 57. The closer the peak of O_2/CH_4, more will the reaction zone within OTR. It can be seen that for 1.625×10^{-07} Kg/s the value of O_2/CH_4 increases downstream making reaction rate and temperature uniform in the OTR. From the above discussion it is concluded that more CH_4 at low mass flow rate is favourable to have in the reactor.

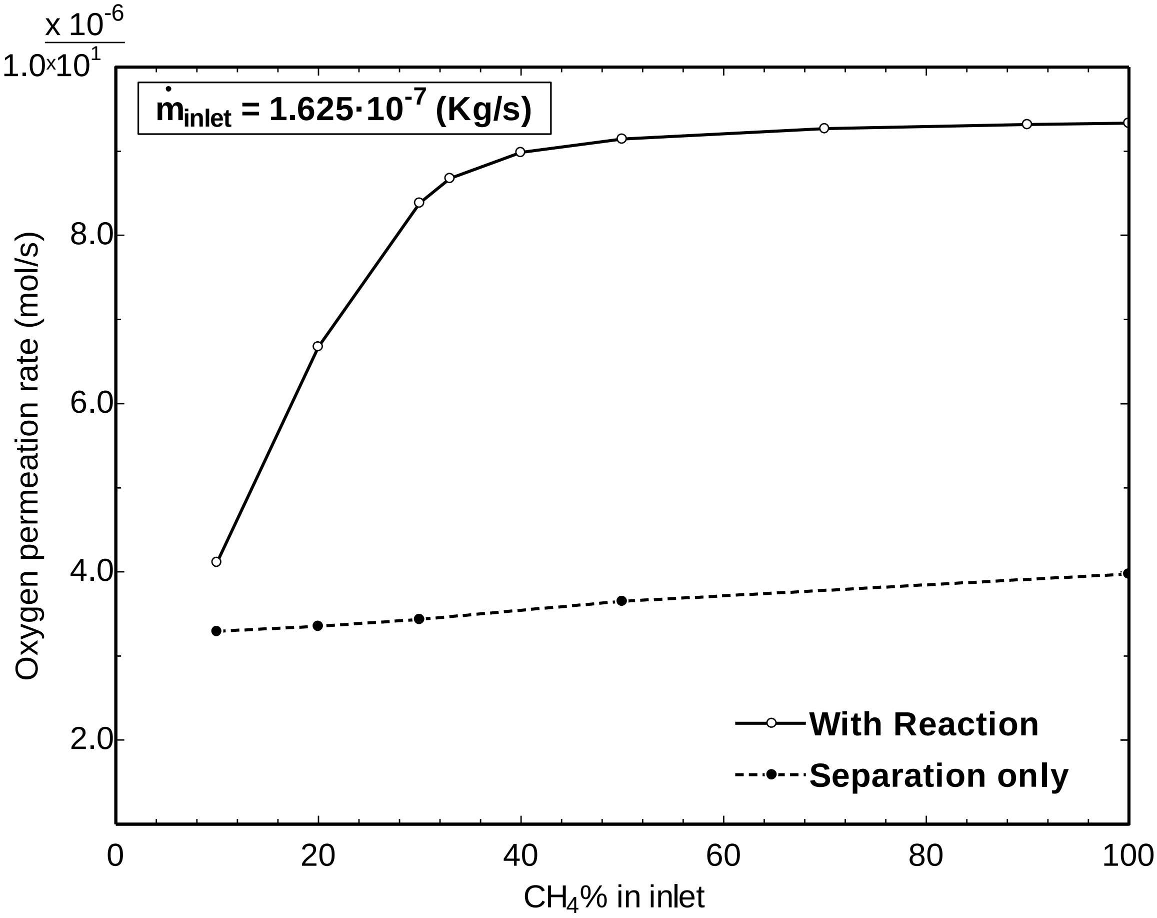

Figure 60 Comparison between oxygen permeation rate from the ITM with and without combustion for mass flow rate of 1.625×10^{-07} Kg/s

Figure 60 shows the oxygen permeation rate in mol/s from the membrane for cold combustion (separation only) and combustion cases. In the figure abscissa is the percentage of CH_4 in fuel mixture while the ordinate is the O_2 permeation rate. The amount of oxygen coming through the membrane towards the permeate side for cold combustion (mixing) is 3.29×10^{-6} mol/s to 3.97×10^{-6} mol/s while for combustion case it is 4.11×10^{-6} mol/s to 9.33×10^{-6} mol/s for 10% to 100% of CH_4 at inlet of fuel mixture. The oxygen permeation rate through the membrane is increases for 10% to 33% CH_4 at inlet and becomes almost constant for the increased CH_4 percentages. This is due to the complete combustion of CH_4 upto 33% at inlet. Oxygen permeation rate through ITM for combustion is very much higher compare with sweep mixture of cold mixing and it is 25% to 135% higher for 10% to 100% CH_4 at inlet.

5.2.7 Temperature contours for different compositions:

Figure 61 shows the temperature contour of different CH_4/CO_2 composition mass ratio m_R for mass flow rate of 1.625×10^{-07} Kg/s. Its can been seen that reaction starts at X/L of 0.15 for almost all the m_R with O_2 partial pressure at feed side P_1= 0.21 atm. As shown, the combustion zone has a maximum temperature of 1250^oC. As the maximum temperature increases, the membrane temperature will also increase; however, part of this heat will be lost to the air domain through the membrane. One can also see from the figure that the temperature around the membrane is less compare to core of the reactor. This will extend the membrane working period and prevent membrane fracture due to thermal stresses on the membrane surface. However more research in required in the membrane materials in order to make it able to withstand higher temperatures with higher oxygen permeation flux. Similar contours can be seen in Figure 61 and 62 for increased mass flow rates. From Figure 61 it is clear that the maximum value of temperature is increased within the reactor but the reaction zone is shifted. For higher mass flow rate of

8.625×10^{-07} Kg/s the reaction zone is shifted to X/L = 0.5. In order to maintain the high O_2 permeation flux the uniform temperature should be maintained for the whole reactor and with the high mass flow rate the uniform temperature ITM cannot be achieved.

Due to the high reactor temperature and small reactor geometry, the strain rate (dU/dx) will be increased due to reduced density and so increased velocity for a particular mass flow rate. This will lead to higher maximum heat release rate in the reaction zone. The flame zone is in the middle of the reactor as shown in Figure 61, 62 and 63. Most of the heat released is lost to air side through the membrane because these membranes have very low thermal resistance.

In order to maximize the CH_4 conversion at high mass flow rates use of catalyst on ITM at permeate side is suggested [92], before proceeding into the catalytic conversion of CH_4 more work has to be done on material development and testing side.

From the above discussion, it is clear that ITM has potential to be implemented in the transforming a conventional combustion chamber to ITM reactor in which separation and oxidation of fuel is done simultaneously by which in turn improves the O_2 separation.

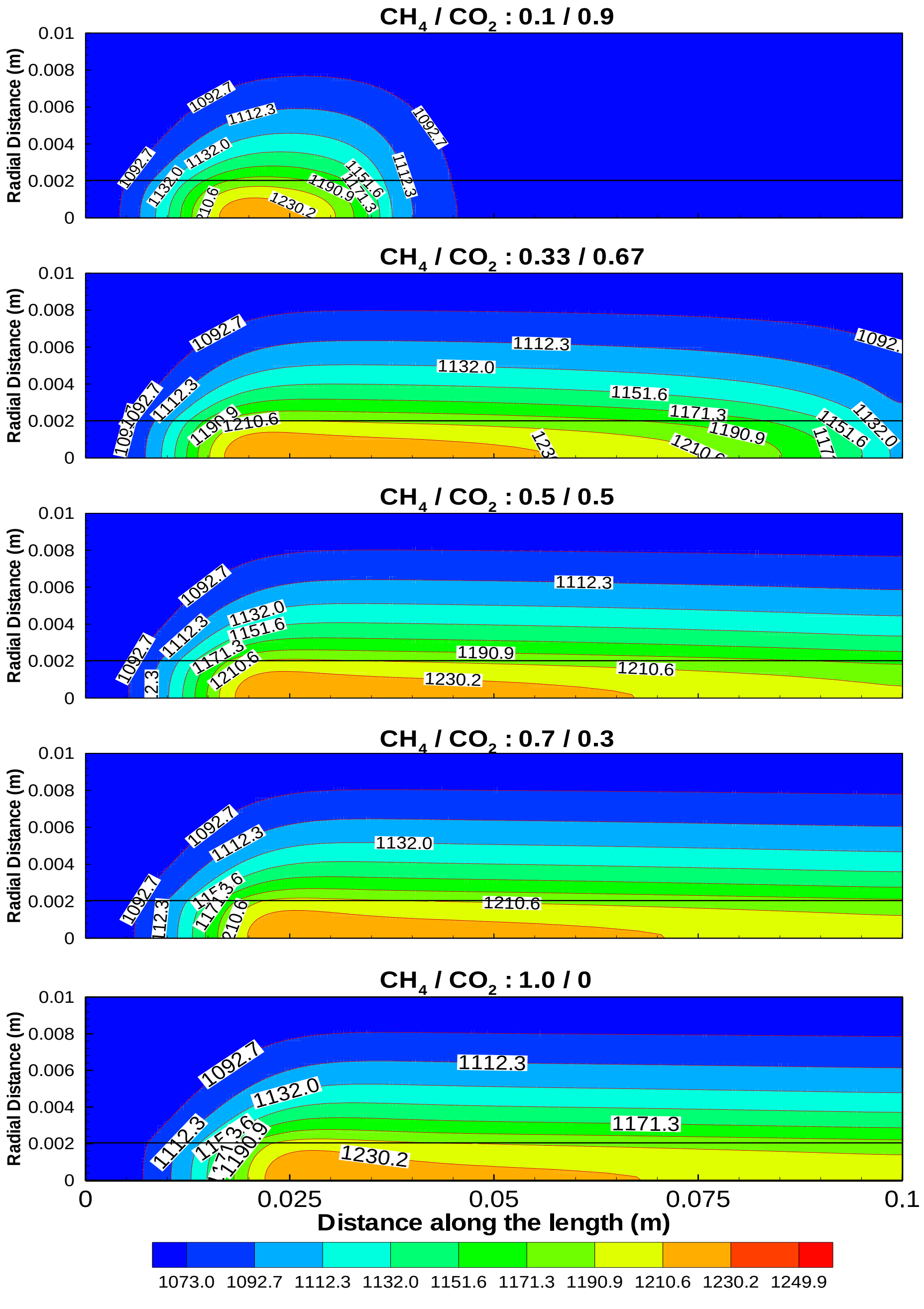

Figure 61 Temperature contour for mass flow rate of 1.625×10^{-07} Kg/s and different

CH_4/CO_2 mixtures mass ratio m_R

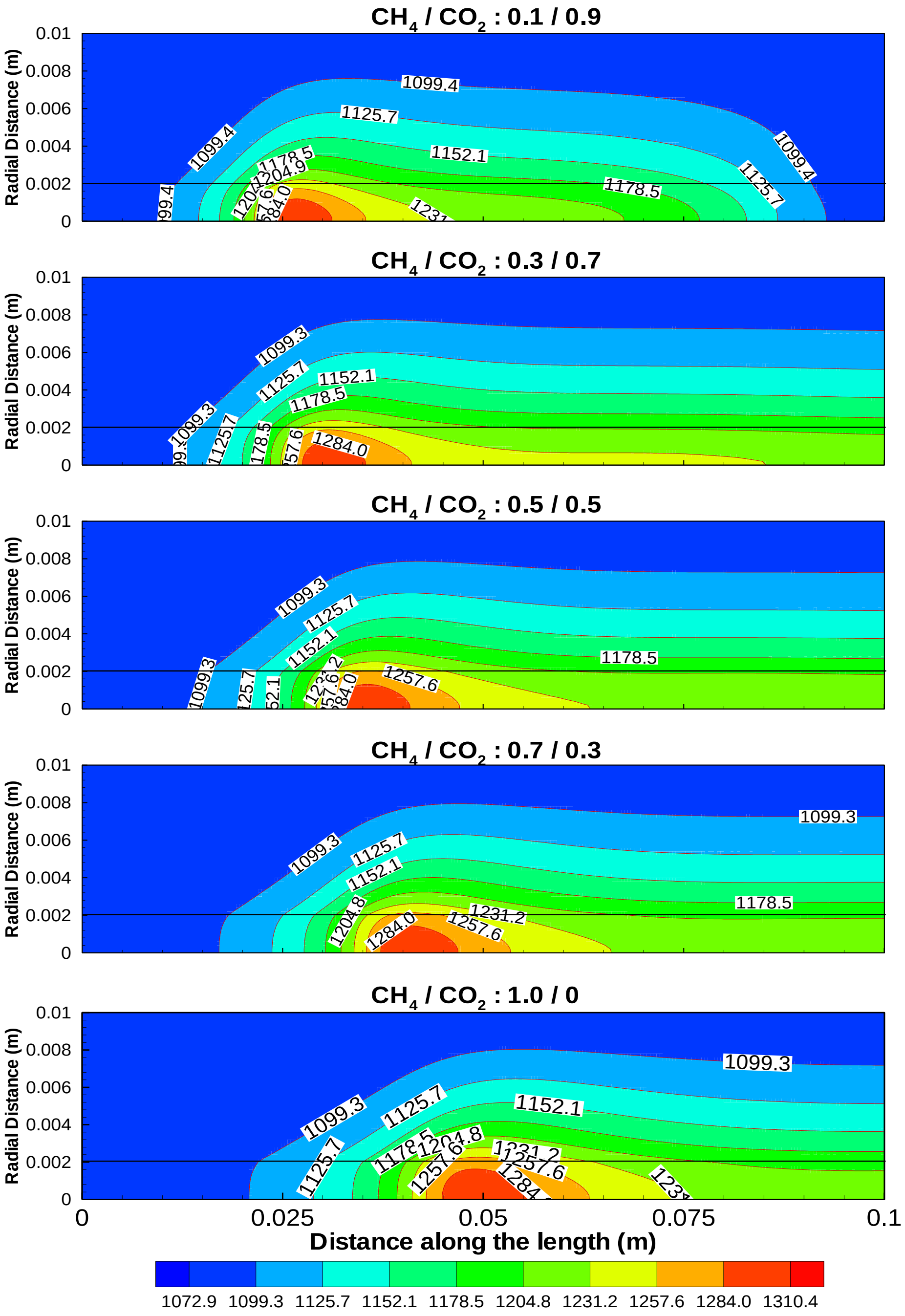

Figure 62 Temperature contour for mass flow rate of 4.625×10^{-07} Kg/s and different CH_4/CO_2 mixtures mass ratio m_R

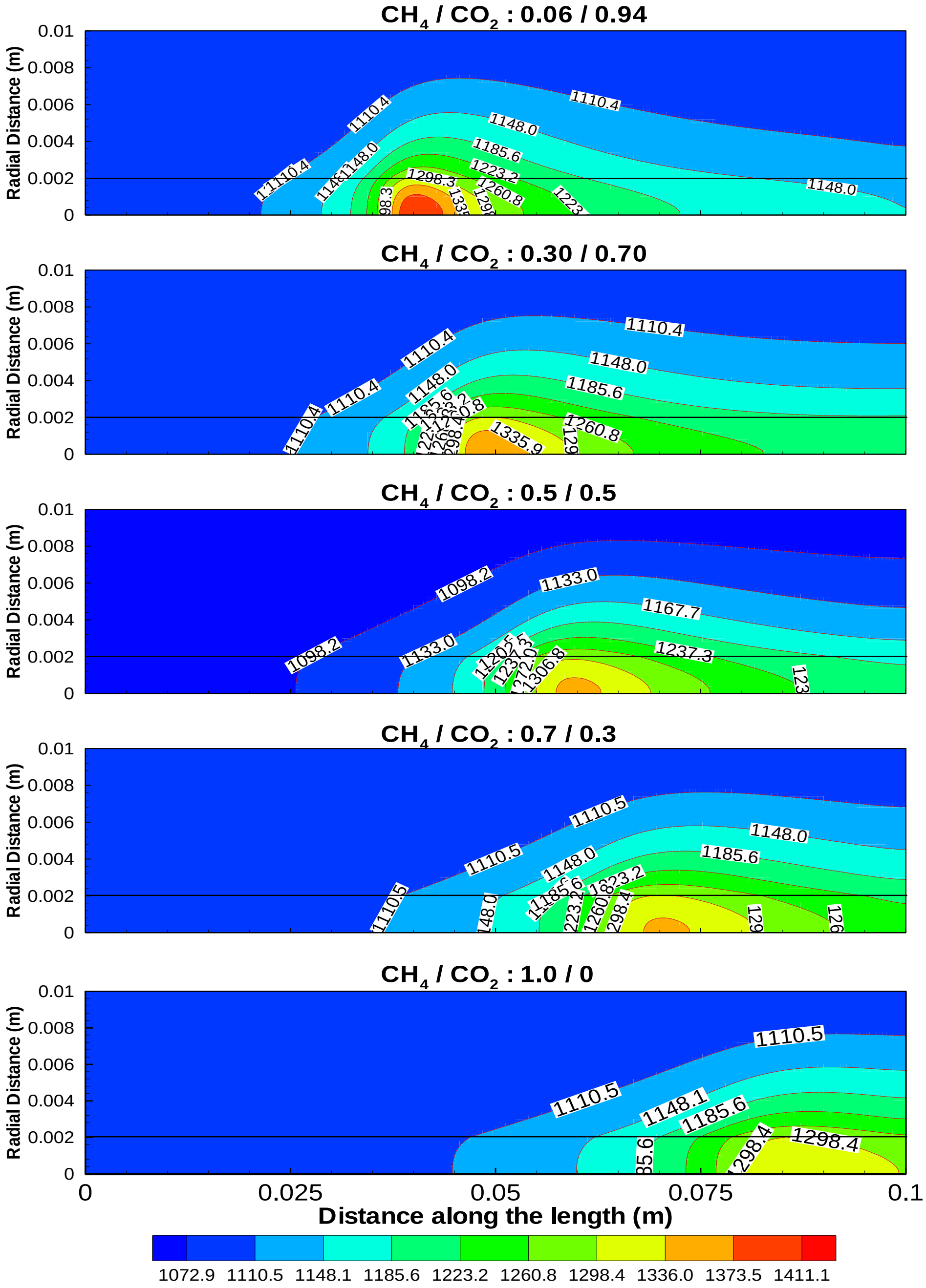

Figure 63 Temperature contour for mass flow rate of 8.625×10^{-07} Kg/s and different CH_4/CO_2 mixtures mass ratio m_R

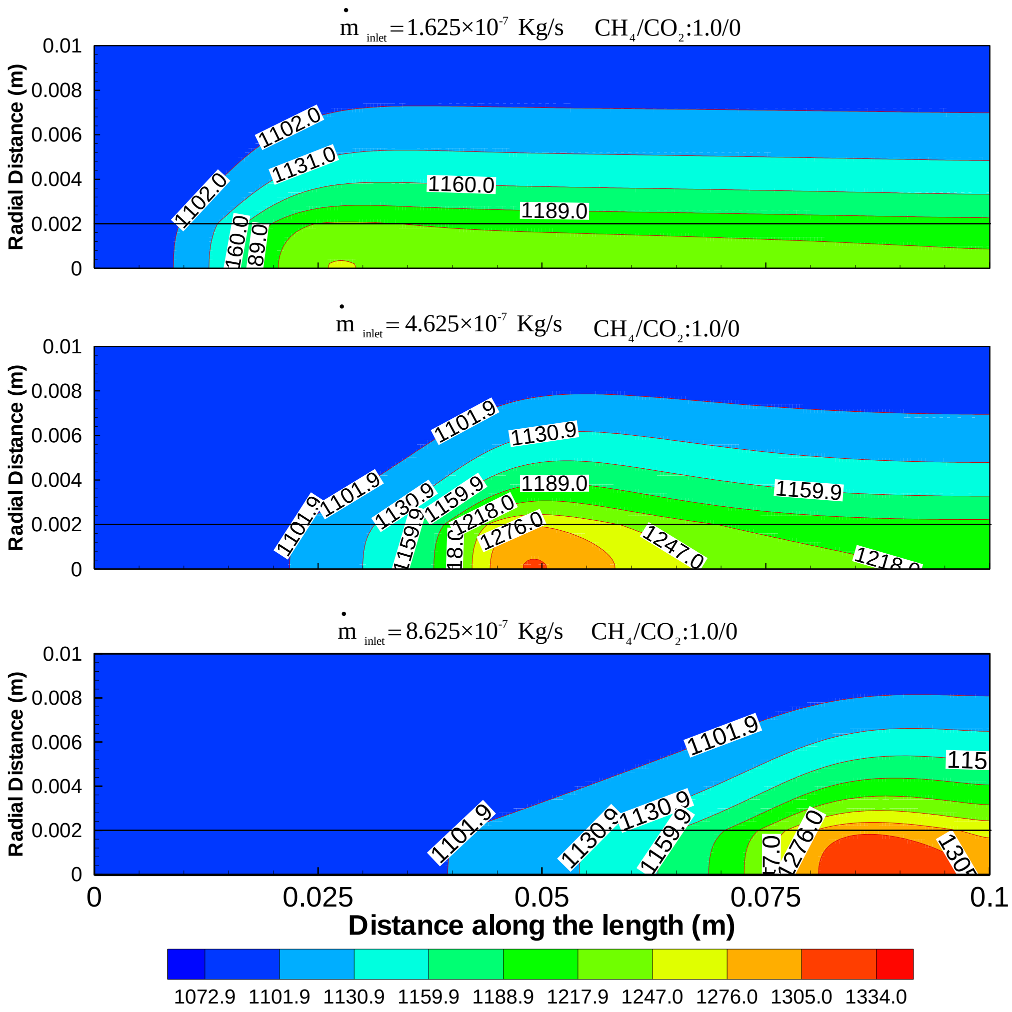

Figure 64 Temperature contour for three different mass flow rate of 8.625×10^{-07} Kg/s for CH4/CO2 of 1.0/0.

Figure 64 shows the temperature contours of three different mass flow rates for a m_R (CH_4/CO_2) of 1.0/0. From the figure, it can depict that with increase of mass flow rate from 1.625×10^{-7} Kg/s to 8.625×10^{-7} Kg/s, the maximum temperature within the reactor is increased. The idea of designing a practical OTR is to maintain uniformity in the temperature to reduce the thermal stresses that may occur with the variation of membrane temperature. So, the uniform temperature within the reactor can be obtained for low mass flow rate of 1.625×10^{-7} Kg/s but with 1250K maximum temperature.

5.3 Energy Balance verification

In order to verify the combustion within ITM reactor, energy balance is done for one particular case with the mass flow rate of 1.625×10^{-07} Kg/s with CH_4/CO_2 of 0.3/0.7. Reactor operates as adiabatic.

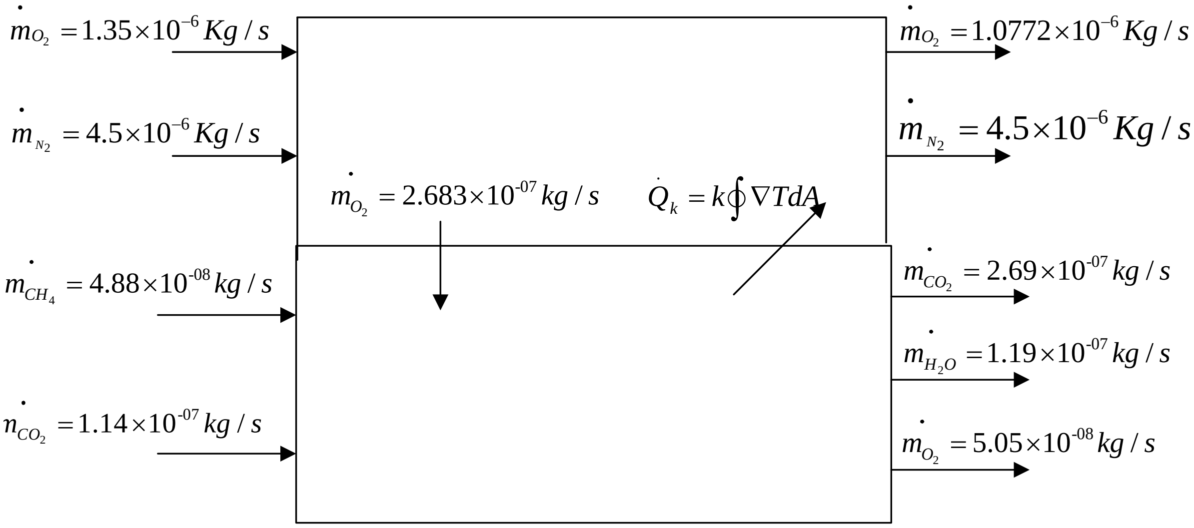

Figure 65 Block Diagram of ITM reactor

In the inlet temperature T_{inlet} = 1073 K, T_r =298.15 K

T_{outlet} =1091.4 K obtained as mass weighted average temperature at outlet of fuel side from FLUENT
T_{Mem} =1084.1 K

Energy balance equation given below.

$$\left(\dot{m}_{CH_4}\right)_{f,inlet}(LCV+Cp_{CH_4}(T_{inlet}-T_r)) + \left(\dot{m}_{CO_2}\right)_{f,inlet} Cp_{CO_2}(T_{inlet}-T_r) +$$

$$\left(\dot{m}_{O_2}\right)_{air,inlet} Cp_{O_2}(T_{inlet}-T_r) + \left(\dot{m}_{N_2}\right)_{air,inlet} Cp_{N_2}(T_{inlet}-T_r)$$

$$= \left(\dot{m}_{CO_2}\right)_{f,outlet} Cp_{CO_2}(T_{f,outlet}-T_r) + \left(\dot{m}_{H_2O}\right)_{f,outlet} Cp_{H_2O}(T_{f,outlet}-T_r) +$$

$$\left(\dot{m}_{O_2}\right)_{f,outlet} Cp_{O_2}(T_{f,outlet}-T_r) + \left(\dot{m}_{N_2}\right)_{air,outlet} Cp_{N_2}(T_{air,outlet}-T_r) +$$

$$\left(\dot{m}_{O_2}\right)_{air,outlet} Cp_{O_2}(T_{air,outlet}-T_r) + k_{mem}\oint_s \nabla T\, dA$$

Energy entering C.V calculation:

$$\left(\dot{m}_{CH_4}\right)_{f,inlet}(LCV+Cp_{CH_4}(T_{inlet}-T_r)) = 4.88\times10^{-8}(5.534\times10^{7}+8.99(1073-298.15))$$

$$= 2.70034 \text{ W}$$

$$\left(\dot{m}_{CO_2}\right)_{f,inlet} Cp_{CO_2}(T_{inlet}-T_r) = 1.14\times10^{-7}\times8.99\times(1073-298.15)$$

$$= 5.86\times10^{-4} \text{ W}$$

$$\left(\dot{m}_{O_2}\right)_{air,inlet} Cp_{O_2}(T_{inlet}-T_r) = 1.35\times10^{-6}\times4.2315\times(1073-298.15)$$

$$= 4.43\times10^{-4} \text{ W}$$

$$\left(\dot{m}_{N_2}\right)_{air,inlet} Cp_{N_2}(T_{inlet}-T_r) = 4.5\times10^{-6}\times3.985\times(1073-298.15)$$

$$= 0.0139 \text{ W}$$

$$\text{Energy\_in} = 2.70034+5.86\times10^{-4}+4.43\times10^{-4}+0.0139$$
$$= 2.716 \text{ W}$$

Energy leaving C.V calculation:

$$\left(\dot{m}_{CO_2}\right)_{f,outlet} Cp_{CO_2}(T_{outlet}-T_r) = 2.695\times10^{-7}\times6.645\times(1091.5-298.15)$$
$$= 1.421\times10^{-3} \text{ W}$$

$$\left(\dot{m}_{H_2O}\right)_{f,outlet} Cp_{H_2O}(T_{outlet}-T_r) = 1.19\times10^{-7}\times5.123\times(1091.5-298.15)$$
$$= 4.84\times10^{-4} \text{ W}$$

$$\left(\dot{m}_{O_2}\right)_{f,outlet} Cp_{O_2}(T_{outlet}-T_r) = 5.05\times10^{-7}\times0.1151\times(1091.5-298.15)$$
$$= 4.611\times10^{-5} \text{ W}$$

$$\left(\dot{m}_{N_2}\right)_{air,outlet} Cp_{N_2}(T_{air,outlet}-T_r) = 4.5\times10^{-6}\times3.9896\times(1081.6-298.15)$$
$$= 0.01406 \text{ W}$$

$$\left(\dot{m}_{O_2}\right)_{air,outlet} Cp_{O_2}(T_{air,outlet}-T_r) = 1.078\times10^{-6}\times4.235\times(1081.6-298.15)$$
$$= 3.577\times10^{-3} \text{ W}$$

$$k_{mem}\oint_s \nabla T dA = 20\times0.136$$
$$= 2.72 \text{ W}$$

$$\text{Energy leaving C.V} = 2.72 + 1.421\times10^{-3} + 4.84\times10^{-4} + 4.611\times10^{-5} + 0.01406$$
$$= 2.721 \text{ W}$$

From the above analysis it is clear that energy is balanced and the combustion of ITM reactor gives affirmative results.

5.4 Effect of local temperature variation along the membrane surface and radiation heat transfer on the combustion process

In the previous analysis, the effects of ITM temperature variation along the membrane surface on the oxygen permeation rate and the radiation heat transfer were neglected. In order to assess the effect of both factors on the combustion process and the resulting thermal field, we conduct detailed computational analysis of three cases. These include the mass flow rate of 1.625×10^{-7} Kg/s and mass ratios m_R=0.1/0.9, 0.5/0.5 and 1.0/0. In all cases, the inlet air and sweep gas temperatures are assumed unchanged (1073K). Both compartments are assumed to have atmospheric pressure.

In the previous calculations, the O_2 permeation flux was based on equation (36) in which the coefficient $K_2(T)$ was assumed constant (corresponding to inlet temperature) along the membrane surface. Since the O_2 permeation flux depends on the local partial pressures of O_2 on both sides of the membrane as well as the local membrane temperature, we must develop a new correlation that takes the membrane temperature variation into consideration. The experimental data of Wang et al. [58] that are shown in Figure 66 forms the basis for obtaining this correlation. The least square method was used for fitting the data (for different temperature ranging from 700 ^oC to 900 ^oC and different partial pressures) assuming an exponential relation between $K_2(T)$ and the temperature. Equation (37) is the obtained correlation that gives the best fit to all data points.

$$J_{O2} = 0.2609 K_1 \exp(-\frac{4270}{T})\left(\sqrt{\frac{P_1}{P_0}} - \sqrt{\frac{P_2}{P_0}}\right) \tag{37}$$

$$K_1 = \frac{2\pi r_1 r_2 w}{S(r_1 + r_2)}$$

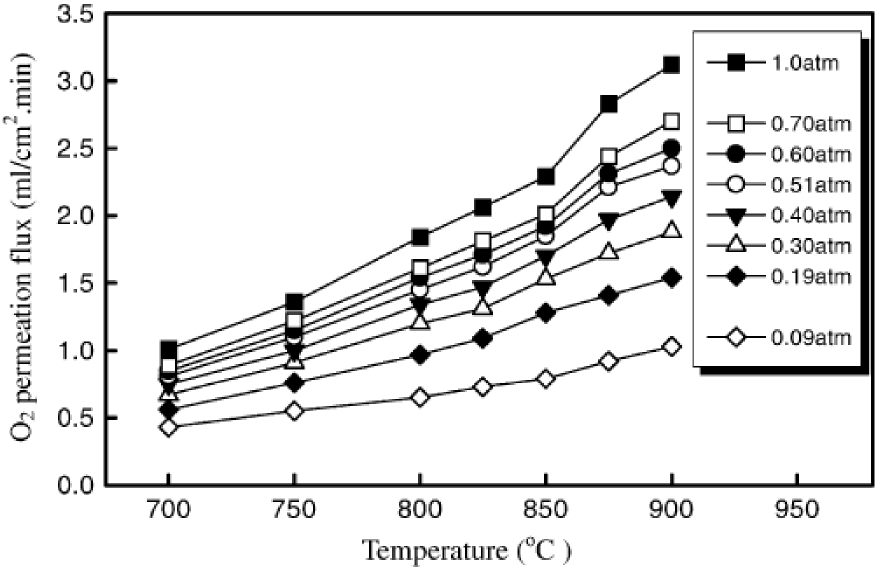

Figure 66 Oxygen Permeation flux through the BSCF membrane tube as a function of temperature [58].

Figure 67 represents the O_2 permeation flux for different partial pressure of O_2 at shell side for increasing temperatures. A simple comparison between the model prediction and the measured values of O_2 permeation flux shows a reasonable accuracy. The largest deviation was about 15% occurring at 900 °C and 0.2 atm. This deviation may be attributed to experimental uncertainties at high temperatures.

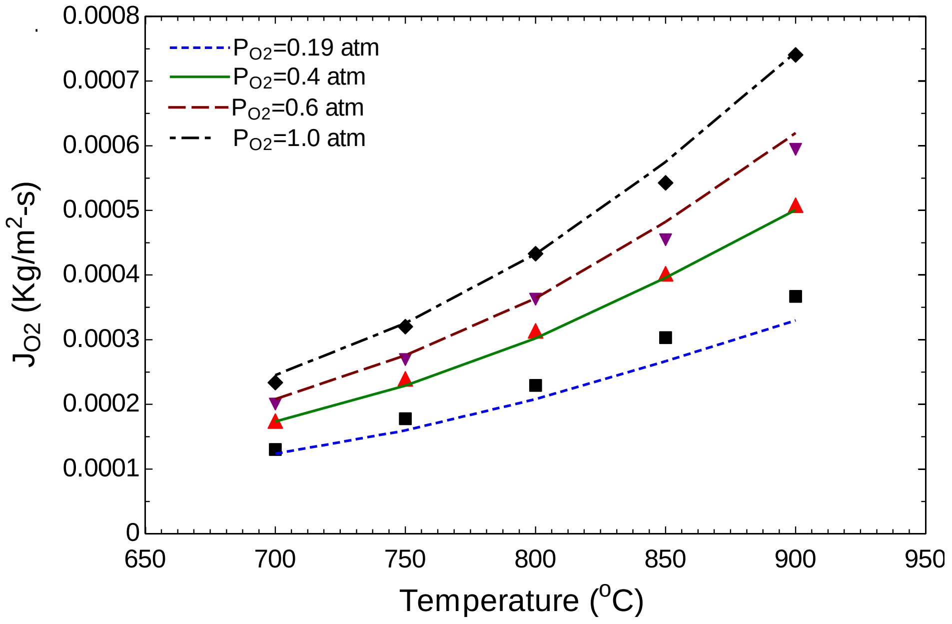

Figure 67 O_2 permeation flux for different temperature for increasing partial pressure at shell side.

In the present simulations, Discrete Ordinate (DO) radiation model is activated and the absorption coefficient was estimated by Weighted Sum of Gray Gas Model (WSGGM). Figure 68 (a) shows the temperature along the axis of the reactor for mass flow rate of 1.625×10^{-7} Kg/s for m_R=0.1/0.9 considering the new O_2 permeation flux equation (37) and the radiation heat transfer model. The figure shows that the maximum temperature is increased by an amount of 25K when the local temperature effect is considered in the O_2

permeation equation. Figure 68 (b) shows the temperature variation along the reactor axis for the same flow rate but with a mass ratio m_R=0.5/0.5.

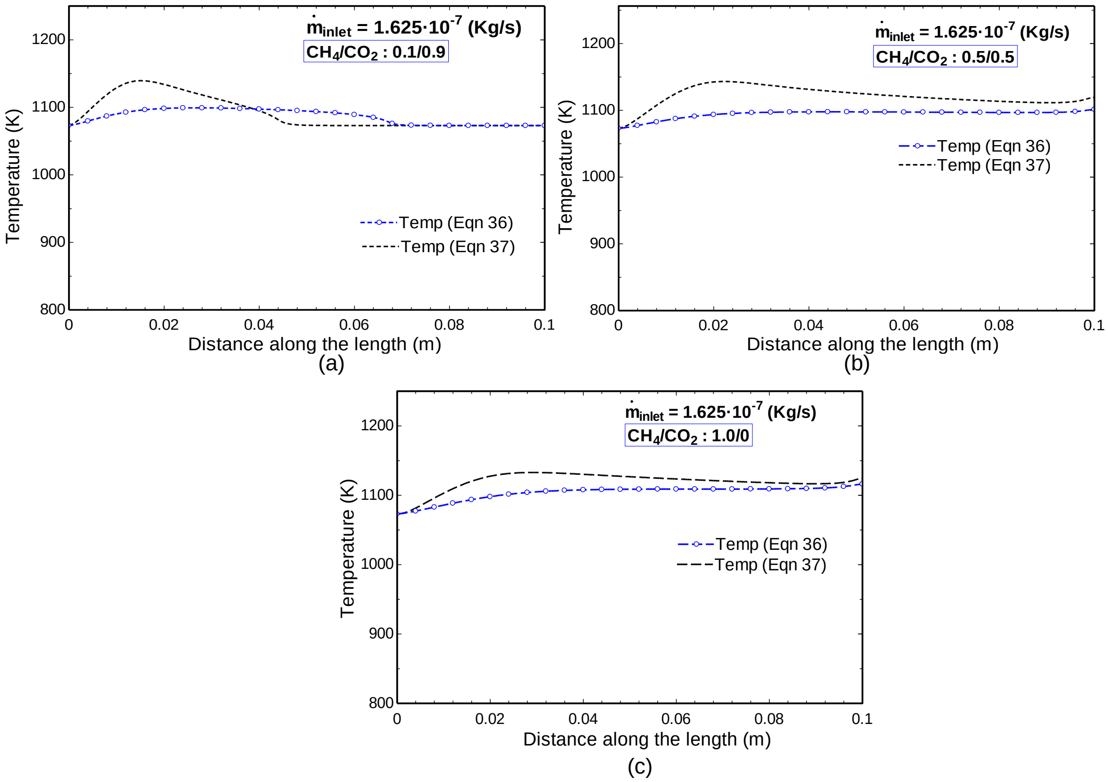

Figure 68 Temperature along the axis of the reactor for mass flow rate of 1.625×10^{-7} Kg/s for a) m_R=0.1/0.9 b) m_R=0.5/0.5 c) m_R=1.0/0

The figure indicates a maximum temperature of 1143 K when the effect of the local temperature variation on the O_2 permeation flux is considered compared with a maximum temperature of 1102 K when neglecting that effect.

For the case of pure CH_4 at inlet (m_R =1.0/0), Figure 68(c) shows small temperature variations along the reactor axis for both cases. The maximum temperature difference between the two cases of using the permeation equations (36) and (37) is about 16K.

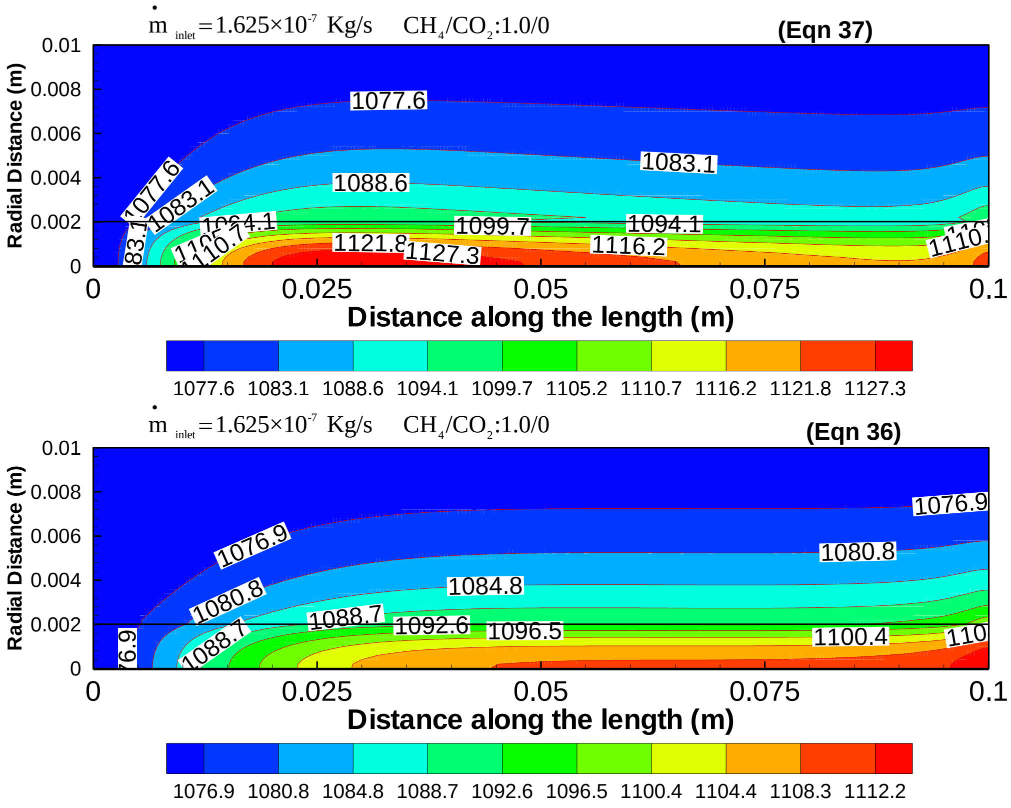

Figure 69 Temperature contours for mass flow rate of 1.625×10^{-7} Kg/s and m_R = 1.0/0 with equation 36 and equation 37

Figure 69 shows the temperature contours for the same flow rate (1.625×10^{-7} Kg/s) and for the mass ratio, m_R=1.0/0, considering the two permeation equations (36) and (37). It can be noted that with equation (37) the maximum temperature is achieved at approximately X/L =0.25 while the maximum temperature is achieved at approximately

X/L=0.5 when using equation (36). The delay in the combustion process when using equation (36) is mainly due to the low rate of O_2 permeation at the inlet region. Based on above analysis, it is clear that the effect of radiation as well as the effect of local temperature variation on the O_2 permeation flux should be considered. However, we wished to have some experimental results to verify the accuracy of the computational model. The absence of this verification prevented fine tuning of the model. A number of questions and uncertainties are still not answered/clarified including the following:

1. The exact chemical reaction taking place (not fully known) will in turn affect the emission and absorption coefficients.
2. The detailed chemistry will definitely differ from the assumed one step chemical reaction and this will affect the chemical composition of combustion products.
3. The effect of composition of combustion products on O_2 permeation through ITM is hard to assess because of lack of experimental results.
4. The O_2 permeation equation needs further improvement by considering the mechanism of O_2 ion exchange through the membrane based on the local parameters (temperature and partial pressures) and membrane characteristics. The obtained correlation [Eq. (37)] gives a maximum difference of 15% with the experimental results.

CHAPTER 6

CONCLUSION AND RECOMMENDATIONS FOR FUTURE WORK

The conclusion is divided into three sections. In the first two sections, the results in the previous chapter are summarized. In the last section, proposed directions for future research are presented.

6.1 Cold Combustion (O_2 separation-only)

A computational model is developed for predicting the performance of a cylindrical ion transport reactor designed for oxy-fuel combustion. The oxygen is supplied through the reactor walls which are made of dense, nonporous, mixed-conducting ceramic membrane that only allows oxygen permeation from the outside air into the combustion chamber. The details of the flow process and the concentration of different species are predicted by a numerical solution of the conservation equations of mass, momentum, energy and species in the axi-symmetric flow domain. The membrane is modelled as a selective layer in which the oxygen permeation depends on the prevailing temperatures as well as the oxygen partial pressure at both sides of the membrane. The model results were validated against previous experimental data and the comparison showed a good agreement. The results indicated that the oxygen to fuel mass ratio increases as the percentage of CO_2 increases in the inflow sweep gas for both co-current and counter-current regimes. In both regimes, the ratio of oxygen to methane increases for decreasing percentage of CH_4 at inlet of the sweep side. It is also found that the increase in the sweep ratio tends to reduce the size of the region outside the flammability limits. The results also indicated that the counter-flow regime exhibits better mixing of fuel and oxygen and provides more uniform oxygen flux along the reactor wall. The total O_2 permeation rate is found to be higher in the counter-current regime for all sweep gas compositions. The regions within the reactor that falls within the recommended flammability limits (O_2/CH_4 ratio between 3.4 and 4.4) are investigated considering three sweep ratios (15.67, 24.0, 49.0). The results indicated that the mixtures having sweep ratio of around 24 for the co-current flow and around 15.67 for the counter-current flow lie within the recommended mixture composition. In both cases, the nearly uniform mixture composition along the membrane leads to nearly homogeneous reaction rates that are likely to result in achieving constant temperature over the membrane surface.

6.2 Combustion in Oxygen Transport Reactor (OTR)

The results of combustion in OTR for different composition of CH_4/CO_2 mixtures and for different mass flow rates have provided many important insights and conclusions. First, the comparison between reactive and separation-only OTR units showed that combining reaction and separation increases significantly O_2 permeation rate to about 2.5 times under the assumptions given herein. Second, for mass flow rate of 1.625×10^{-07} Kg/s with CH_4/CO_2 mass ratio ranging from 0.5/0.5 to 1.0/0 gives almost uniform axial temperature of about 1250 K in most of the reactor length with high CH_4 conversion of 75% to 35% respectively. In all the simulations, the total O_2 permeation flux is almost the same except for 1.625×10^{-07} Kg/s with CH_4/CO_2 m_R less than 0.3/0.7. Since the thermal resistance of these membranes is low, the heat of reaction is mostly transferred to the air side with a portion used to heat the O_2 permeating flux. For higher mass flow rates, the OTR operates with rich mixture resulting in low CH_4 conversion. The combustion process in such cases can be improved by splitting the OTR into a series of units where the fuel is added at stages along the reactor network. This work requires significant experimental and modeling work and is outside the scope of this thesis.

6.3 Future work:

The use of ITM technology to capture CO_2 in power cycles shows potential to retrofit or to use as an auxiliary system to separate O_2 for oxy-combustion. The O_2 permeation equation used this work is based on experimental correlations. More work is needed to develop a more generalized equation which represents the membrane characteristics and operational conditions. Further, single-step chemistry is used in the present simulations for oxidation of methane into CO_2 and H_2O, but in practice there will be other species such as CO, H_2, etc. Accordingly, detailed chemistry must be employed to study the impact and stability of such species on ITM. Other major issues related to the effect of carbon deposition and soot formation on the membrane characteristics need detailed investigation.

A single ITM reactor results in low exit temperature and much loss of heat into the air side, a series of ITM reactors could be created such that the membrane surface area is split to a series of segments. This may lead to a higher temperature at the reactor exit that makes the combustion products more suitable in power cycles.

Nomenclature

L_c	characteristic membrane thickness [m]
D_s	self-diffusivity [m^2/s]
k_{io}	surface exchange coefficient [m/s]
t_i	ionic transference number [-]
t_e	electronic transference number [-]
μ_{O_2}	Oxygen vacancy potential [J/mol]
L	Membrane thickness [m]
F	Faraday’s constant [c/mol]

J_{O_2}	oxygen permeation flux [mol/m^2-s]
σ_i	ionic conductivity [S/m]
σ_e	electronic conductivity [S/m]
R	Gas constant [J/molK]
p	pressure [Pa]
$V_O^{\bullet\bullet}$	oxygen vacancy [-]
D_v	diffusion coefficient of oxygen vacancies [cm^2/s]
V_m	molar volume [m^3/mol]
E_a	activation energy [J/kg-mol]
$P_{O_2}^{'}$, P_1	partial pressure of oxygen at the feed side [atm]
$P_{O_2}^{''}$, P_2	partial pressure of oxygen at the permeate side [atm]
C_i	density of oxygen ions [mol/m^3]
T	temperature [K]
r_1	outer radius of the membrane tube [m]
r_2	inner radius of the membrane tube [m]

S	effective area of the membrane tube [m^2]
β_1	bulk-diffusion step constant [-]
$P_{O_2}^0$, P_0	1 atm oxygen pressure
U	velocity vector [$m\ s^{-1}$]
ρ	density [$Kg\ m^{-3}$]
μ	dynamic viscosity [$N\ s\ m^{-2}$]
S_i	source/sink term [Kg/m^3-s]
R_1	resistance to O_2 permeation at the inner membrane surface [$atm^{0.5}cm^2sec/mol$]
R_2	resistance to O_2 permeation in the bulk region [$atm^{0.5}cm^2sec/mol$]
R_3	resistance to O_2 permeation at the outer membrane surface [$atm^{0.5}cm^2sec/mol$]
$D_{i,m}$	diffusion coefficient of mixture of species i [m^2/s]
k_f	surface-exchange reaction forward-rate constant [$cm\ atm^{-0.5}s^{-1}$]
k_r	surface-exchange reaction reverse-rate constant [$mol\ cm^{-2}s^{-1}$]
K_1	geometric constant [-]

Y_i	mass fraction of species i [-]
$D_{i,j}$	binary mass diffusion coefficient of species i [m^2/s]
C_p	heat capacity [J/Kg-K]
A_{cell}	area of the cell [m^2]
MW_{O_2}	molecular weight of oxygen [Kg/Kmol]
V_{cell}	volume of cell [m^3]
X_i	mole fraction of species i [-]
K_2	constant depends on temperature [mol/m^2-s]
w	effective length of the tube [m]
$\Re$	Universal gas constant [J/molK]
M_i	molecular weight of species i [Kg/Kmol]
λ_i	thermal conductivity of species i [W/m/K]
$\varphi_{i,j}$	mixture rule constant for species i in species j [-]
k	reaction rate constant [Kg-mol/m^3-s]
A	pre-exponential factor [-]
$\dot{m}$	mass flow rate [Kg/s]

Suffix

op	operating
mix	mixture

References

[1] C. Keller, 2007, “Global Warming 2007. An Update to Global Warming: The Balance of Evidence and Its Policy Implications,” The Scientific World, Vol. 7: 381–399. doi:10.1100/tsw.2007.91.

[2] World Petroleum availability 1980-2000, a technical memorandum, NTIS order #PB81-145252.

[3] http://www.upstreamonline.com/live/article195770.ece (visited on 20th December 2010).

[4] N. Akinfiev, J. McGovern, E. Yantovski, “Zero Emissions Power Generation with CO_2 Reduction by Fayalite,” Int. J. of Thermodynamics, Vol. 8, No. 3: 155-157, 2005.

[5] Proceedings of Fourth Annual Conference on Carbon Sequestration, 2005, Alexandria, U.S.A., May 5-10.

[6] Proceedings of Fifth Annual Conference on Carbon Sequestration, 2006, Alexandria, U.S.A., May 8-11.

[7] IPCC. Intergovernmental Panel on Climate Change Special Report on Carbon Dioxide Capture and Storage. Cambridge university press, Cambridge, UK, 2005.

[8] IEA. International energy agency, Key World Statistics. Stedia Media, France, 2007a.

[9] E. Rubin, L. Meyer, H. Coninck, IPCC Special Report; “Carbon Dioxide Capture and Storage, Technical Summary”, 2005.

[10] L. Eide and D. Bailey, “Pre-combustion decarbonisation process” Oil and gas science and Technology – Rev. IFP, vol 60, 2005, no. 3, 475-484.

[11] D. Singh, E. Croiset, P. Douglas, M. Douglas, “Techno-economic study of CO_2 capture from an existing coal-fired power plant: MEA scrubbing vs. O_2/CO_2 recycle combustion”, Energy Conversion and Management 44, 2003, 3073-3091.

[12] D. Bailey, P. Feron, “Post-combustion Decarbonisation Process”, Oil & gas science and Technology – Rev. IFP, vol 60, 2005, n°3, 461-474.

[13] “Prospects for CO_2 capture and storage”, OECD/IEA, 2004, Paris, France.

[14] D. Arnold, D. Barrett, R. Isom, “CO_2 can be produced from flue gas”, Oil & Gas Journal, 1982, 80(47), 130–136.

[15] P.J. Gellings and H.J.M. Bouwmeester, “The CRC Handbook of Solid State Electrochemistry”, CRC Press, Boca Raton, (1997) 481-553.

[16] H. Kvamsdal, K. Jordal, O. Bolland, “A quantitative comparison of gas turbine cycles with CO_2 capture”, Energy 32 (2007) 10-24.

[17] B.Buhre, L. Elliott, C. Sheng, R. Gupta and T. Wall**.,** “Oxyfuel combustion technology for coal-fired power generation”, Progress in Energy and Combustion Science Vol. 31, Issue 4, (2005), 283-307

[18] K. Klostermann, M. Hermsdorf, K. Mieske, R. Eggers, D. Koepke,“Concept for a 600 MWe coal-fired power plant with CO_2 capture based on the oxyfuel process”, 38 Power Plant Power Conference, 24.-25.10.2006, Dresden.

[19] Y. Tan, E. Croiset, M. Douglas**,** K. Thambimuthu.,“Combustion characteristics of coal in a mixture of oxygen and recycled flue gas”, Fuel, Vol. 85 (2006) 507-512.

[20] J. Chen, Z. Liu, J. Huang., “Emission characteristics of coal combustion in different O2/N2, O_2/CO_2 and O_2/RFG Atmosphere”, Journal of hazardous materials, Vol. 142 (2007) 266-271..

[21] J. Chen and J. Huang, “Combustion efficiency and CO_2 emission from O_2/N_2, O_2/CO_2 and O_2/RFG coal combustion processes”, Environ. Eng. Sci., vol. 24, No. 3 (2007) 353-362.

[22] K. Andersson and F. Johnsson, “Flame and radiation characteristics of gas-fired O_2/CO_2 combustion”, Fuel 86 (2007) 656–668.

[23] www.vattenfall.com, (accessed on 29 December 2010).

[24] M. Anheden, J. Yan, G. De Smedt.,“Denitrogenation (or oxyfuel concepts)”, Oil and gas science technology –Rev. IFP, Vol. 60, No 3 (2005) 485-495.

[25**]** E. Kakaras, A. Koumanakos, A. Doukelis, D. Giannakopoulos**,** I. Vorrias**,** “Oxyfuel boiler design in a lignite-fired power plant”, Fuel, Vol. 86 (2007) 2144-2150.

[26] F. Chatel-Pelage, R. Varagani, P. Pranda, N. Perpin, H. Farzan, S. Vecci, Y. Lu, S. Chen, M. Rostam-Abadi, and A. Bos. “Applications of oxygen for NOx and CO_2 capture in coal-fired power plants”, Thermal Science, Vol. 10, No 3 (2006), 119-142.

[27] H. Liu, R. Zailani, B. Gibbs, “Comparisons of pulverized coal combustion in air and in mixtures of O_2/CO_2”, Fuel, 84 (7-8), 2005. 833-840.

[28] C. Hermsdorf , A. Kather, M. Klostermann, K. Mieske, “Oxyfuel process for Hard Coal with CO_2 Capture: First results”. Hamburg University of Technology.

[29] R. Anderson, S. Doyle, K. Pronske, “Demonstration and Commercialization of Zero-Emission Power Plants”, 29th International Technical Conference on Coal Utilization & Fuel Systems April 18-22, 2004, Clearwater, FL, USA.

[30] S. Sunqvist, H. Eklund, T. Griffin, “AZEP – an EC funded Project for Development of a CCGT Power Plant without CO_2 Emissions”, In Proceedings of CAME-GT 2nd Int'l Conference on Gas Turbine Technologies, Bled, Slovenia, 2004.

[31]S. Sundquist, K. Sjödin, K. Wilhelmsen, K. Asen, A. Tintinelli, S. McCahey, H. Ye, "AZEP gas turbine combined cycle power plants," InProceedings of GHGT-7, Uni Regina, Canada,2004.

[32] F. Beggal, S. Engels, M. Modigell, N. Nauels., "OXYCOAL-AC: Integration of high temperature membranes for air separation into oxyfuel power plants", 1st oxyfuel combustion conference, Cotbus, 2009.

[33] H. Stadler**,** F Beggel**,** M. Habermehl**,** B. Persigehl**,** R. Kneer**,** M. Modigell**,** P. Jeschke; "Oxyfuel coal combustion by efficient Integration of Oxygen Transport Membranes", International Journal of Greenhouse Gas Control (2010). (2011) 7-15.

[34] E. Yantovski, J. Gorski, B. Smyth, J. Elshof, "Zero Emission Fuel-Fired Power Plant with Ion transport Membrane," Energy, Vol. 29, No. 12-15: (2004) 2077- 2088.

[35] K. Foy, PhD Thesis, "Investigation into the possible use of an oxygen ion transport membrane combustion unit in an oxyfired power plant", Dublin institute of Technology, 2007.

[36] E. Tzimas, A. Mercier, C. Cormos, and S. Peteves, "Trade-off in emissions of acid gas pollutants and of carbon dioxide in fossil fuel power plants with carbon capture" Energy Policy 35 (2007) 3991–3998

[37] M. Bernal, J. Coronas, M. Menendez, and J. Santamarıa, "Separation of CO_2 /N_2 Mixtures Using MFI-Type Zeolite Membranes", AlchE Journal Vol. 50 (2004) 127.

[38] R. Thorogood, R. Srinivasan, T. Yee, M. Drake, “Composite mixed conductor membranes for producing oxygen”, US Patent 5,240,480 (1993)`

[39] S. Kim, Y. Yang, A. Jacobson, B Abeles; “Diffusion and surface exchange coefficients in mixed ionic electronic conductiong oxides from the pressure dependence of oxygen permeation”, Solid State Ionics, 106 (1998) 189-195.

[40] Y. Lin, W. Wang, J. Han, “Oxygen permeation through thin mixed-conducting solid state membranes”, AlchE J. 40(5) (1994)786.

[41] J. Elshof, H. Boumeester, H. Verweij, “Oxidative coupling of methane in a mixed-conducting perovskite membrane reactor, Appl. Catal, A130(1995) 195.

[42] Z. Shao, W. Wang, Y. Cong, H. Dong, “Investigation of ther permeation behaviour and stability of a $Ba_{0.5}Sr_{0.5}Co_{0.8}Fe_{0.2}O_{3-\delta}$ oxygen membrane”, Journal of membrane science, 172 (2000) 177.

[43] X. Qi, Y. Lin, S. Swartz, “Electric transport and oxygen permeation properties of lanthanum cobaltite membranes synthesized by different methods”, Ind. Eng. Chem. Res. 39 (2000) 646.

[44] S. Kim, Y. Yang, A. Jacobson, B. Abeles, “Oxygen surface exchange in mixed ionic electronic conductor membranes”, Solid state Ionics 121(1999) 31-36.

[45] S. Kim, Y. Yang, A. Jacobson, B. Abeles, “Diffusion and surface exchange coefficients in mixed ionic electronic conducting oxides from the pressure dependence of oxygen permeation”, Solid State Ionics 106(1998) 189-195.

[46] J. Han, Y. Zeng, Y. Lin, “Oxygen permeation through fluorite-type bismuth–yttrium–copper oxide membranes”, Journal Membrane Science.132 (1997) 235.

[47] Y. Nigara, J. Mizusaki, M. Ishigame, “Measurement of oxygen permeability inCeO2 doped CSZ”, Solid State Ionics 79 (1995) 208

[48] E. Capoen, M. Steil, G. Nowogrocki, M. Malys, C. Pirovano, A. L ofberg, E.Bordes-Richard, J. Boivin, G. Mairesse, R. Vannier, “Oxygen permeation in bismuth-based materials. Part I: Sintering and oxygen permeation fluxes”, Solid State Ionics 177 (2006) 483.

[49] S. Dou, C.R. Masson, P.D. Pacey, “Mechanism of oxygen permeation through lime stabilized zirconia”, Journal Electrochemical Society, 132 (8) (1985) 1843

[50] S. Liu, X. Tan, Z. Shao, J. Diniz, “$Ba_{0.5}Sr_{0.5}Co_{0.8}Fe_{0.2}O_{3-\delta}$ ceramic hollow fibe membranes for oxygen permeation”, AlChE J. 52 (10) (2006) 3452.

[51] X. Tan, K. Li, Modeling of air separation in a LSCF hollow-fiber membrane module, AIChE J. 48 (7) (2002) 1469.

[52] S. Xu, W. Thomson, “Oxygen permeation rates through ion-conducting perovskite membranes”, Chemical Engineering Science, 54 (1999) 3839.

[53] X. Tan, K. Li, “Oxygen production using dense ceramic hollow fiber membrane modules with different operating modes”, AlChE J. 53 (4) (2007) 838.

[54] X. Tan, Y. Liu, K. Li, “Mixed conducting ceramic hollow-fiber membranes for air separation”, AlChE J. 51 (7) (2005) 1991.

[55] X. Tan, S. Liu, K. Li, R. Hughes, “Theoretical analysis of ion permeation through mixed conducting membranes and its application to dehydrogenation reactions”, Solid State Ionics 138 (2000) 149.

[56]J. Guan, S. Dorris, U. Balachandran, M. Liu, “Transport properties of $BaCe_{0.95}Y_{0.05}O_{3-\alpha}$ mixed conductors for hydrogen separation”, Solid State Ionics 100 (1997) 45.

[57] X. Tan, K. Li, A. Thursfield, I. Metcalfe, “Oxyfuel combustion using a catalytic membrane reactor”, Catalysis today 131 (2008) 292-304.

[58] H. Wang, Y. Cong, W. Yang; “Oxygen permeation study in a tubular $Ba_{0.5}Sr_{0.5}Co_{0.8}Fe_{0.2}O_{3-\delta}$ oxygen permeation membrane”, Journal of Membrane Science 210 (2002) 259-271.

[59] M. Guillodo, J. Fouletier, L. Dessemond, P. Gallo; "Oxygen permeation through dense $Bi_2V_{0.9}Cu_{0.1}O_{5.35}$ ceramic membranes", Journal of The Electrochemical Society, 149(12) J93 J99 (2002).

[60] Z. Taheri, K. Nazari, N. SayedMatin, A. ASafekordi, B. Ghanbari, S. Zarrinpashne, R. Ahmadi; "Comparison of oxygen permeation through some perovskite membranes synthesized with EDTNAD", Reac Kinet Mech Cat(2010) 100:459-469.

[61] J. Xuan, M. Leung, D. Leung, M. Ni; "Integrating Chemical kinetics with CFD modeling for autothermal reforming of biogas", Journal of Hydrogen Energy,34 (2009) 9076-9086.

[62] X. Zhu, S. Sun, Y. Cong, W. Yang., "Operation of perovskite membrane under vacuum and elevated pressures for high purity oxygen production", Journal of membrane science 345 (2009) 47-52.

[63] J. Caro, K. J. Caspary, C. Hamel, B. Hoting, P. Kölsch, B. Langanke, K. Nassauer, T. Schiestel, A. Schmidt, R. Schomäcker, A. Seidel-Morgenstern, E. Tsotsas, I. Voigt, H. Wang, R. Warsitz, S. Werth, and A. Wolf, "Catalytic Membrane Reactors for Partial Oxidation Using Perovskite Hollow Fiber Membranes and for Partial Hydrogenation Using a Catalytic Membrane Contactor", Ind. Eng. Chem. Res., 46 (8), 2286 -2294, 2007.

[64] S. Lui, G. Gavalas, "Oxygen selective ceramic hollow fiber membranes", Journal of membrane science, 246(2005)103.

[65] H. Iwahara, T. Esaka, T Mangahara, “Mixed conduction and oxygen permeation in the substituted oxides for $CaTiO_3$”, Journal of Applied Electrochemistry, 18(1988)173.

[66] F. Akin, Y. Lin, “Selective oxidation of ethane to ethylene in a dense tubular membrane reactor”, Journal of Membrane Science, 209(2002)457.

[67] F. Akin, Y. Lin, “Oxidative coupling of methane in dense ceramic membrane reactor with high yields”, AlChE Journal, 47(2) (2001)436.

[68] Y. Teraoka, H. Zhang, S. Furukawa, N. Yamazoe, “Oxygen permeation through perovskite-type oxides”, Chemical letter, 11(1985) 1743.

[69] K. Li, X. Tan, Y. Liu, “Single-step fabrication of ceramic hollow fibers for oxygen permeation”, Journal of Membrane Science, 272 (2006)1.

[70] M. den Exter, J. Vente, D. Jansen, W.G. Haije, “Viability of mixed conducting membranes for oxygen production and oxyfuel processes in power production”, Energy Procedia 1(2009) 455-459.

[71] U. Balachandran, J. Dusek, R. Mieville, R. Poeppel, M. Kleefisch, S. Pei, T. Kobylinski , C. Udovich , A. Bose, “Dense ceramic membranes for partial oxidation ofmethane to syngas”, Applied Catalysis A: General 133 (1995) 19-29.

[72] W. Stephens, T. Mazanec, H. Anderson,” Influence of gas flow rate on oxygen flux measurements for dense oxygen conducting ceramic membranes”, Solid State Ionics 129 (2000) 271-284.

[73] W. Zhang, J. Smit, M. Annaland, J. Kuipers, “Feasibility study of a novel membrane reactor for syngas production Part 1: Experimental study of O2 permeation

through pervoskite membranes under reducing and non-reducing atmosperes", Journal of Membrane Science 291 (2007) 19-32.

[74] J. Smith, W. Zhang, M. Annaland, J. Kuipers, "Feasibility study of a novel membrane reactor for syngas production Part 2: Adiabatic reactor simulation", Journal of Membrane Science, 291 (2007) 33-45

[75] H. Liu, Z. Pang, X. Tan, Z. Shao, J. Sunarso, R. Ding , S. Liu, "Enhanced oxygen permeation through perovskite hollow fibre membranesby methane activation", Ceramics International 35 (2009) 1435–1439.

[76] M. Coroneo, G. Montante, A. Paglianti; "Numerical and Experimental Fluid Dynamic Analysis to improve the mass transfer performances of Pd-Ag Membrane Modules for Hydrogen Purification"; Ind. Eng. Chem Res. 2010, 49,9300-9309.

[77] M. Coroneo, G. Montante, M. GiacintiBaschetti, A. Paglianti; "CFD Modelling of inorganic membranse modules for gas mixture separation"; Chemical Engineering Science, 64(2009) 1085-1094.

[78] S. Goto, S. Assbumrungrat, T.Tagawa, P. Praserthdam; "The effect of direction of Hydrogen on the rate through a composite palladium membrane", Journal of Membrane Science, 175(2000) 19-24.

[79] M. Staudacher, M. Harasek, T Brinkmann, W. Hilgendroff, A. Friedl "CFD-Simulation of mass transfer effects in gas and vapour permeation modules", Desalination 146(2002) 237-241.

[80] Kang Li, “Ceramic Membranes for separation and reactions”, John Wiley &Sons ltd, 2007.

[81] User’s Guide, Fluent 6.3 Documentataion, Fluent Inc., Lebanon, NH 2006.

[82] McGee HA. Molecular engineering. New York: McGraw-Hills; 1991.

[83] N. Mancini and A. Mitsos, “Ion Transport Membrane Reactors for oxy-combustion- Part I: Intermediate Fidelity Modeling, Energy, 2011.

[84] N. Mancini and A. Mitsos, “Ion Transport Membrane Reactors for oxy-combustion- Part II: Analysis and comparison of Alternatives, Energy, 36 (4721-4739) 2011.

[85] S. Turns, Introduction to Combustion, McGraw Hill, 2000.

[86] Kenneth Kuon-yun Kuo, Principles of Combustion, 2nd Edition, John Wiley & Sons, 2005.

[87] J. Jarosinski, B. Veyssiere, Combustion Phenomenon, CRC Press, 2009.

[88] S. Patankar, “Numerical Heat Transfer and Fluid Flow”, Washington D.C.; Hemisphere Publishing Company, 1980.

[89] D. Norton and D. Vlachos “Combustion characteristics and flame stability at the micro-scale: a CFD study of premixed methane/air mixtures”, Chemical Engineering Science 58 (2003) 4871 – 4882.

[90] M. Arnold, H. Wang, A. Feldhoff, “Influence of CO_2 on the oxygen permeation performance and the microstructure of perovskite-type $(Ba_{0.5}Sr_{0.5})(Co_{0.8}Fe_{0.2})O_{3-\delta}$ membranes”, Journal of Membrane Science, 293 (2007) 44-52.

[91] H. Kruidhof, H. Bouwmeester, R. Van Dooen, A. Buggaraaf, “Influence of order-disorder transitions on oxygen permeability through selected non-stiochiometric perovskite-type oxide”, Solid State Ionics 63-65(1993)816.

[92] M. Hong, L. Chengye, L. Hui, J. Shengfu, “Simulation of catalytic combustion of methane in monolith honeycomb reactor”, Chineese Journal of Chemical Engineering, 14 (1) 56-64(2006).

[93] W. Buykx, “Specific heat, thermal diffusivity and thermal conductivity of Synroc, perovskite, Zirconolite and Barium Hollandite”, Journal of Nuclear Materials 107 (1982) 78-82.

[94] S. Yamanaka , T. Hamaguchi , T. Oyama , T. Matsuda , S.Kobayashi, K. Kurosaki, “H eat capacities and thermal conductivities of perovskite type $BaZrO_3$ and $BaCeO_3$”, Journal of Alloys and Compounds 359 (2003)1–4.

[95] A. Chernatynskiy, R. Grimes, M. Zurbuchen, D. Clarke and S. Phillpot, “Crossover in thermal transport properties of natural, perovskite structured superlattices”, Applied Physics Letters, 95, 161906 (2009).

[96] N. Kaisare, D. Vlachos, “Optimal reactor dimensions for homogeneous combustion in small channels”, Catalysis Today 120 (2007) 96–106.

Vita

Name: Azharuddin

Nationality: Indian

Present address: P.O. Box: 8620, KFUPM, Kingdom of Saudi Arabia.

Telephone: 00966552542328 (Present), 0091-9848931084 (Permanent)

Education: Received Bachelor of Engineering degree in Mechanical Engineering from Osmania University, Hyderabad, India in 2008

Experience: Worked as Field Operation and Panel Engineer in Reliance Industries Limited, India from 2008-2009.

Joined Mechanical Engineering Department of King Fahd University of Petroleum and Minerals, Dhahran as Research Assistant in October 2009.

E-mail: azharuddin0613@gmail.com, azharuddin_0613@yahoo.ca